UNIVERSITY OF LEEDS

Metadynamics Calculations of Magnetic Skyrmion Stabilities

Ioannis Charalampidis

University of Leeds

School of Physics and Astronomy

Submitted in accordance with the requirements for the degree of

Doctor of Philosophy

April, 2023

Intellectual Property Statement

The candidate confirms that the work submitted is his own and that appropriate credit has been given where reference has been made to the work of others.

This copy has been supplied on the understanding that it is copyright material and that no quotation from the thesis may be published without proper acknowledgement.

The right of Ioannis Charalampidis to be identified as Author of this work has been asserted by him in accordance with the Copyright, Designs and Patents Act 1988.

Acknowledgements

I would like to express my deepest gratitude to my PhD supervisor Dr Joseph Barker for his excellent supervision throughout my PhD research journey. Even from the first time I met him for my PhD interview and during every formal or informal discussion I had with him, he helped me become a better scientist and stimulated my academic interest in the field. His mentorship, guidance and encouragement helped me grow both as a scientist and as an individual. At the same time, his incredible expertise and practises in the field of magnetism have been invaluable and have clearly demonstrated to me what excellent science practices are. As I have expressed to him, the main reason I chose the University of Leeds for my PhD mostly had to do with him, which I consider one of my wisest decisions.

I also need to thank my colleagues for all the help, academic discussions and academic stimulation, especially Dr Thomas Nussle, Sean Stansill, and Robert Mackay, which not only increased my interest in the field and motivated me to keep good science practises but also made every single day more enjoyable during the good and not so good days of this PhD journey.

Finally, nothing of all this would be possible without the constant support and motivation from my parents and brother during my PhD journey and all my friends, who kept me on track with everything that defines me as a person.

Abstract

Interfacial magnetic skyrmions are topological spin textures that have been proposed for use as information carriers in spintronic devices. Hence, it is vital that their creation, annihilation, and motion can be accurately controlled [1]. Still, their thermal stability and interactions are not fully understood. Currently, athermal methods such as the geodesic nudged elastic band method (GNEBM) are used to quantify the skyrmion creation and annihilation energy barriers, including only the skyrmion's internal energy. Furthermore, GNEBM is a low-temperature formalism that samples only saddle points along the energy landscape without providing any information about the transition from a skyrmionic to a ferromagnetic (FM) state and vice versa. Similarly, the skyrmion lifetimes are often estimated using energy barrier calculations and an arbitrary attempt frequency [2, 3].

In contrast with GNEBM calculations, this thesis successfully demonstrated a novel use of metadynamics combined with atomic-scale magnetic simulations performed to reconstruct the free energy landscape (FEL) of macroscopic skyrmion observables. The reconstructed FELs are then used to quantify the skyrmions creation and annihilation energy barriers as a function of temperature, including both the effects of the internal energy and entropy, which is a major factor in skyrmion stability [4]. The reconstructed FEL shows every possible transition path from a skyrmionic to a ferromagnetic path. Additionally, it is demonstrated that the skyrmions' attempt frequency in finite temperature can be estimated with metadynamics and not assumed. Nonetheless, with the use of metadynamics, the effects of magnetisation reversal in thin films with DMI are explored, revealing the generation of a chiral domain that expands to reverse the magnetisation. Finally, the procedures to explore the effect of lattice defects and exploration of all possible topological spin textures in any thin film heterostructure in finite temperatures with metadynamics are reported. Ultimately, the results of this thesis demonstrate new procedures which can be used to design and realise future skyrmionic devices by identifying possible spin textures and assessing their thermal stability and lifetimes accurately while fully accounting for temperature effects.

CONTENTS

LIST OF FIGURES

List of Tables

Abbreviations

BCC	Body Centered Cubic	CMOS	Complementary Metal Oxide Semiconductor
CPU	Central Processing Unit	CVs	Collective Variables
DFT	Density Functional Theory	DMI	Dzyaloshinskii-Moriya Interaction
DRAM	Dynamic Random-Access Memory	DW	Domain Wall
FCC	Face Centered Cubic	FEL	Free-Energy Landscapes
FM	Ferromagnetic	GMR	Giant Magneto Resistance
GNEBM	Geodesic Nudged Elastic Band Method	HAMR	Heat Assisted Magnetic Recording
HCP	Hexagonal Close Packed	IDMI	Interfacial DMI
MAE	Magnetocrystalline Anisotropy Energy	MC	Monte Carlo
MMC	Metropolis Monte Carlo	MRAM	Magnetic Random Access Memory
PMA	Perpendicular Magnetic Anisotropy	QCD	Quantum Chromodynamics
STT	Spin-Transfer Torque	TMR	Tunneling Magneto-Resistance
UHV	Ultra High Vacuum		

CHAPTER 1

Introduction

1.1 Motivation

The rapid scientific and technological advances following the birth of quantum mechanics in the 1920s are largely affected by the constant increase in computational power and information storage capacities; since they allow the computation of more complex mathematical models and analysis of large datasets. As technological applications, scientific measurements and societies' growth rely on the constant increase of fast computations and large data storage capacities, many current technological limitations arise, which magnetic spin textures such as magnetic skyrmions show the potential to resolve, as discussed later in this section.

More importantly, conventional computational devices are energy inefficient, which is limiting considering the increasing threat of climate change. In 2018, data storage facilities consumed approximately 205 Terawatt hours (TWh) of energy, which is 25% more than in 2010. This accounts for the 1% of the global energy consumption [7]. Similarly, as an example, for this project, High-Performance Computer (HPC) clusters with Intel Xeon Gold 6138 were used, with an energy consumption of 125 Watts (for 20 CPU cores) [8]. In February 2023 alone, this project used 190 CPU cores running for 14 days consuming 39.9 kWh (excluding the energy required to cool down the CPUs, data storage and all the peripherals). Using the conversion factor of 0.23314 kg CO_2 per kWh as shown in the UK's energy Department 2022 report [9], only in February, the computations required for this project produced 9.3 kilograms of CO_2. As a comparison, a train journey from Leeds to London produces 11.98kg of CO_2 [9]. Much attention is devoted to producing Green energy to cover the increasing energy demands for computations and data storage [10]. However, it is crucial that more energy-efficient technologies are developed rather than producing more energy to cover the energy required for current computational devices.

To further introduce the main limitations of conventional computational devices and why they are becoming more energy inefficient, it is important to consider their main operational features. Modern computer architectures rely on microchip designs, where transistors perform computations. Transistors are made of doped semiconducting metal oxide materials to form a source and a drain separated by a gate. Thus devices utilising transistors are often referred to

as Conventional Metal Oxide Semiconducting (CMOS) devices. Transistors have two states, one with current flowing from the source to the drain and one which is not, translated to 0 and 1, respectively. When current is applied to the gate, the fermi surface of the device changes and current flows from the source to the drain; thus, a transistor can be considered a small capacitor whose charge and discharge speed dictate the computation speed. Traditionally the computational speeds are improved by reducing the physical dimensions of the transistors to increase their density within a microchip while reducing the transistors switching times by decreasing the capacitance of the gate.

In the 1960s, Gordon E. Moore predicted that the number of transistors in microchips would double every two years. This proposition indicated that the computational devices would exponentially increase their computational speeds. This postulate is called Moore's Law and has proven accurate from the 1960s to 2013 but has broken down since [11, 12]. This is due to the limitations of the continual miniaturisation of transistors and CMOS devices. As the physical dimensions are reduced, the distance between the source and the drain becomes smaller. This increases the leakage current from the source to the drain when current is not applied to the gate due to quantum tunnelling of electrons, which can lead to overheating and decreasing the devices reliability [13]. Other major limitations include short-channel effects, increased power consumptions and manufacturing yield issues [14]. At the same time, the manufacturing costs increase due to the multiple technical difficulties that arise due to the higher resolution requirements of optical lithography. More importantly, there are physical material limits due to the reduction of the size of the transistor. These limits arise from the semiconducting materials currently used in transistors (i.e. will stop having semiconducting properties) [15, 16]. Currently, 3nm chips are used commercially, and any further reduction in the transistor's physical dimensions becomes physically limiting. Modern computational needs like AI, image recognition, navigation and scientific calculations require higher computational speeds. Additionally, increasing demand for applications requiring beyond Von-Neumann technologies, such as neuromorphic, reservoir and probabilistic computing, require computational hardware with collocated processing and data storage, stochasticity and massive cross-parallel computation [17]. Thus, new emerging technologies and materials are required to overcome Moore's Law

to continue increasing the computational power and provide the hardware requirements to meet the demands of future technological applications.

At the same time, there is an exponential increase in demand for fast, stable and non-volatile data storage devices. Many businesses, services and sophisticated scientific algorithms require large data size storages. For example, the first image of the M87 supermassive black hole required collecting and analysing 4 petabytes of data [18]. Additionally, it is expected that by 2025, 20 zeta bytes per user/customer will be required [19]. Lately, many advances have been achieved in the data storage industry by improving the Heat Assisted Magnetic Recording (HAMR) hard drives, making the hard drives more reliable [20]. However, new technologies must continue meeting the increasing data storage capacities and computation speed demands.

1.1.1 Spintronic Devices

One avenue that promises to help overcome Moore's Law with next-generation technologies is the field of spintronics. Spintronics takes advantage of the spin and charge of electrons and/or holes in a material [21]. Spintronics can replace conventional CMOS technologies and introduce new devices to overcome the limitations of Moore's Law and the increasing demand for data storage by replacing conventional CMOS technologies or their hardware components. One of the main characteristics of spintronic devices is the control of spin polarisation at interfaces in magnetic materials and the propagation of information with spin transfer torques (STT). Another spintronic device design utilises the manipulation of nanoscale magnetic spin textures, which can be used as non-volatile information carriers. These spin textures are spin patterns in nanoscale magnetic materials formed due to the interplay of magnetic interactions, which are engineered by altering the magnetic anisotropies in low dimensions. Multiple disruptive spintronic components and principles have been established in conventional computational devices, which have increased their energy efficiency, storage capacities and computational speeds. Some of the most widely used include the Giant Magneto Resistance (GMR) sensors used to detect changes in the magnetic fields and convert them into electrical signals enabling the operation of hard drives. Tunnelling Magneto-Resistance (TMR) is used in Magnetic Random Access Memory (MRAM) based on quantum tunnelling [21]. It provides high-speed data

storage with low power consumption and the Spin-Transfer Torque (STT) MRAM, an advanced version of MRAM. [21].

These spintronic technologies have replaced parts of current CMOS technologies used for computations and data storage. This has decreased their energy consumption and improved their reliability and operational speeds. Still, they cannot continue meeting the rising demand for energy-efficient computational speeds and non-volatile data storage capacities. One of the most promising spintronic technologies to overcome all these issues is the design of devices utilising magnetic spin textures to design logic gates, non-volatile storage devices, and beyond von Neumann computational devices that do not rely on traditional computational architectures with transistors [22, 23]. Such concepts were experimentally demonstrated in works such as Allwood et al. in 2005, who used ferromagnetic nanowires with propagating magnetic domain walls (DW) to perform computational logic operations, such as AND, OR, and NOT gates [24]. DWs are the boundaries between two regions with different magnetisation directions formed to reduce the energy of ferromagnetic materials. These DWs can be isolated in nanowires and move within a nanowire with speeds up to $\approx 600\mathrm{m/s}$ with low applied currents or external stimuli [25]. Isolated DWs are non-volatile and can be used as information carriers. In 2008 Parkin et al. proposed the design of racetrack memories, which include suspended nanowires with DWs that can be propagated with low currents and stopped at specific regions for read/write operations [26]. The DW sizes can be many orders smaller than the conventional magnetic domains used in conventional hard drives, which can create ultra-dense memories. Computational devices utilising spin textures also offer the benefit of performing computations and storing data at the same physical device location. This is a crucial advantage over conventional CMOS devices and modern computers since the buses that slow down conventional computations are minimised. Additionally, DWs are non-volatile and less prone to data losses due to high energy particles or temperature fluctuation changing the state of the devices. However, as it was found, the propagation and pinning of DWs are stochastic in nature, limiting the usage, design and realisation of any deterministic computational devices utilising magnetic domain walls [27]. At the same time, the DW velocity is linearly increasing only for low-applied field strengths. There is a critical field strength in which the DW velocity shows retrograde mo-

tion if exceeded, called Walker breakdown, which further limits the usage of DWs [27, 28]. On the contrary, DWs are successfully being used in other applications, such as sensors and show potential to be used in many architectures of probabilistic and reservoir computing [23, 29].

A more recent development involves spin textures with the potential to be used in the next generation of spintronic devices, which are the magnetic skyrmions, first experimentally observed in 2009 [30]. Compared to DWs, skyrmions show particle-like characteristics that are easier to control, making them easier to manipulate within a device and can have sizes below 10 nm [31]. In short, magnetic skyrmions are topological defects within magnetic textures. They can exist in non-centrosymmetric bulk magnetic crystals with large SOC, such us MnSi and FeCoSi [32] or at the interfaces between layers of heavy metals and ferromagnetic layers in thin films with broken inversion symmetries where large DMI interactions are induced such as Ir/Co/Pt [33] and Pt/Co/Ta [34], multilayers. Their particle-like dynamics and properties make them ideal candidates for future spintronic information carriers. An important aspect of magnetic skyrmions is their thermal stability and lifetimes. Skyrmions often are metastable spin textures, which can be annihilated in high temperatures. In order to be used in devices, it is important to be thermally stable at elevated temperatures, which is one of this project's motivations. The thermal stability of skyrmions is primarily based on their unique topological nature, which has sparked an increased research interest in skyrmions. Thus, rapid advances in the field of skyrmionics are seen, with many groups recently demonstrating skyrmionic operating brain-inspired neuromorphic devices for pattern recognition applications [35].

1.1.2 Brief Skyrmion Literature Review

In 1962 skyrmions were hypothesised as topological solitons in non-linear field theory by the nuclear physicist Tony Skyrme [36]. Later in 1989, Bogdanov and Yablonski proposed that chiral skyrmions could exist in magnetic materials [37]. Five years later, Bogdanov and Hubbert theoretically demonstrated that thermodynamically stable chiral skyrmions could be stabilised in materials where the antisymmetric exchange DMI interaction is present [38]. However, the rapid advances in the field of skyrmionics started in 2009 when S.Muhlaber et al. suggested that the a-phase in the MnSi phase diagram is a closed-packed hexagonal lattice of

skyrmions [30]. MnSi is a non-centrosymmetric B20 crystal whose crystal structure induces DMI. This suggestion was based on their small-angle neutron scattering measurements, which can not resolve the internal magnetic spin structure; thus, they could not identify the skyrmion spin texture, but model calculations suggested that the hexagonal Bragg peaks observed in their neutron scattering experiments should be stable skyrmions. Later in the same year, A. Neubauer et al. supported the argument that the a-phase in MnSi is a skyrmion lattice with their Hall effect measurements that identify the skyrmionic spin texture [39]. At the beginning of 2010, skyrmion lattices were observed in semiconducting materials $\mathrm{Fe_{1-x}Co_xSi}$ using similar small angle neutron measurements [40]. Later in 2010, for the first time, isolated interfacial skyrmions were observed in real space measurements with TEM in thin films at 40K, stabilised by strong magnetic fields [41]. Compared with the bulk MnSi, where the crystal structure induces DMI, an interface between a ferromagnetic layer and a heavy metal layer induces DMI due to the strong spin-orbit coupling at the interface. In the following two-year period, skyrmions were found in many different multilayered thin films under applied magnetic fields at temperatures up to 40K. The small temperature range and the presence of a magnetic field required to stabilise skyrmion lattices were limiting the study and the technological applications of skyrmions. In 2012, it was found that the temperature range of the FeGe host system where skyrmions can nucleate can be tuned by altering the thin film thickness [42]. The following year, it was demonstrated that by alloying the composition of $\mathrm{Mn_{1-x}Fe_xSi}$, the temperature range and skyrmions size could be optimised, which pathed a new way to skyrmions research. At the same time, a study showed that by adding a layer of Pd in Fe/Ir(111) thin film heterostructure, a stronger DMI can be achieved due to strong spin-orbit coupling [43].

However, it was not until 2016 that room-temperature skyrmions were stabilised without an external magnetic field [44]. This sparked a lot of research regarding the creation, motion, thermal stability, interaction with defects and host systems for specific applications. Additionally, skyrmions were observed in many different material classes such us insulating $\mathrm{Cu_2OSeO_5}$, frustrated magnets, Heusler alloys, and much more fully discussed in a recent review [45]. Theoretical and computational studies supported all these experimental findings, which naturally led to the proposal of skyrmionic devices [1]. First, a racetrack memory with

skyrmions was proposed [43, 46]. Logic gates similar to the ones with DWs and logic gates incorporating both skyrmions and DWs [47, 48].MRAMs and MTJs have been proposed to use skyrmions to control the device resistivity by manipulating the number of skyrmions [49]. Similarly, many brain-inspired neuromorphic devices utilising skyrmions and probabilistic computers were proposed [22].

Recently many groups experimentally demonstrated successful operations with low-energy neuromorphic skyrmionic devices for pattern and image recognition where an input signal generates skyrmions that change the synaptic weights between layers in neuromorphic architectures by taking advantage of the non-linear skyrmion phenomena such as nucleation, propagation and annihilation [22, 35, 50]. In 2022, 94.7% accuracy in hand-written recognition was achieved using a neuromorphic skyrmionic device [50]. Furthermore, many skyrmionic devices rely on the interaction of skyrmions with other spin textures, which are hard to study their stabilities experimentally. Still, no unified analytic theory predicts the skyrmion dynamics, stabilities and interactions with defects or other spin textures. On the contrary, specific analytic equations can be used to describe specific skyrmion phenomena, such as the Thiéle equations, which have been extensively used to study skyrmion motion under external stimuli which are also experimentally verified [51]. Hence numerical models are used to guide and support experiments, propose new skyrmionic device architectures and test their stability. However, often these models do not fully account for temperature effects and the thermal stability of skyrmionic devices is not fully understood or proven. Many numerical formalisms use an algorithm named Geodesic Nugded Elastic Band Method (GENBM) that was first used to calculate the skyrmion metastable energy in 2015 [52]. This algorithm is used in many studies to estimate the skyrmion lifetimes [2, 3, 53, 54]. However, as Desplat et al. showed in 2018, the skyrmion stability also depends upon the change in configurational entropy and the metastable skyrmion energy [4].

A better understanding of the thermal stability and the temperature effects of the coexistence with other spin textures is required for the design and realisation of future skyrmionic devices [1, 22, 55].

1.1.3 Project Motivations and Achievement

This project's primary motivation was to develop a technique that can be used to explore the thermal stability of interfacial magnetic skyrmions in any magnetic thin film heterostructure. Moreover, we are interested in quantifying how the creation and annihilation energies scale with temperature and how they are affected by lattice defects or interaction with other spin textures. As a result of the original motivation, the major project's accomplishment was the development of a computational method that can be applied to a system in order to assess topological spin textures' thermal stability and their coexistence with an emphasis on magnetic skyrmions while mapping the transition paths between creation and annihilation of these spin textures. Additionally, our estimates of these energy barriers are in finite temperature, including the contribution of the entropic barriers. Compared to the GNEBM, here, metadynamics is used to reconstruct the free energy landscape (FEL) instead of sampling only the saddle points of energy landscapes, which only include the contributions from skyrmions' internal energy.

1.2 Thesis Overview

To introduce the main computational methods and results of this project, the theoretical background of magnetism required for the following discussions is introduced in this chapter's subsections. In chapter 2, the background theory of the techniques used is introduced and discussed. The main results of this thesis are presented in chapters 3, 4, 5, 6. As the results demonstrate, the development of a procedure to study the thermal stability of skyrmions is developed, which can now be used for a plethora of other investigations, which are the natural continuations of the research conducted in this project. Hence in chapter 7, the next steps are extensively discussed while demonstrating most of the calculations and procedures which should be used to achieve them. Finally, the main conclusions of this thesis are summarised in chapter 8

1.3 Magnetic Materials

The first historically recorded observation of magnetism without attributing it to mythological gods was by Thales of Miletus, an ancient Greek philosopher, in 600 BC. He observed the effect of ferromagnetism in Fe_3O_4 stones, widely known as lodestones, in the ancient Greek city of Magnesia, from which the modern name magnetism is derived [56, 57]. Similarly, in 1086 AD, the Chinese astronomer Shen Kua reported using magnetic materials as a compass for navigation [58]. Later many European scientists experimented with the observed magnetic properties in magnetic materials, which led to the development of Columbus' compass. However, it was not until 1600, when William Gilbert argued that the Earth itself is a magnet based on his scientific experiments, that the rapid advances in magnetism started [56, 58]. Eventually, with the birth of quantum mechanics in the 1920s, we connected the origin of magnetism to the electron's spin orbitals and motion, which sparked a lot of technological and theoretical advances with regard to magnetism, especially in condensed matter physics.

1.3.1 Origin of Atomic Dipole Moments

All elements are made of negatively charged electrons orbiting the positively charged nucleus. In quantum physics, each electron is described by a wave function, Ψ, that satisfies the Schrödinger equation. Electrons are most likely to be found anywhere within regions of high probability called orbitals surrounding the atomic nucleus. The orbitals' orientation, size and shape depend on the three quantum numbers that arise from the Schrodinger equation. In the hydrogen model, the energy of electrons depends on their distance from the nucleus, which is quantised and labelled by the integer principal quantum number n, often referred to as energy levels. Electrons with the same n form a shell. Within a shell, orbitals are divided into subshells with the same angular momentum quantum number l (s,p,d,f), which dictates the orbital shape. Finally, the number and orientation of orbitals within a subshell depend on the magnetic quantum number m_l.

The orbital angular momentum $\mathbf{L}$ of electrons around the nucleus gives rise to the orbital

magnetic dipole moment given by [59, 60]

$$\mu_{\mathrm{L}} = -g_{\mathrm{L}}\mu_{\mathrm{B}}\frac{L}{\hbar} \tag{1.1}$$

where g_{L} is the dimensionless proportionality g-factor constant which relates μ_{L} to the angular momentum quantum numbers.$\mu_{\mathrm{B}} = \frac{\mathrm{e}\hbar}{2m_{\mathrm{e}}c} = 9.27 \times 10^{-24}\mathrm{J/T}$ is the Bohr magneton where m_{e} is the electron's mass and $\hbar$ is the reduced Planck's constant. However, considering only μ_{L}, the magnitudes of bulk atomic magnetic dipole moments measured experimentally could not be explained, especially for 3d elements such as Fe and Co.

Finally, as it was shown, electrons have an additional intrinsic property called spin, described by electron spin quantum number m_{s} which take values $m_{\mathrm{s}} = +\frac{1}{2}$ often referred to as "spin-up" or $m_{\mathrm{s}} = -\frac{1}{2}$ often referred to as "spin-down", which is independent of the other three quantum numbers and is given by the following expression [61, 62].

$$\mu_s = -g_s\mu_{\mathrm{B}}\frac{S}{\hbar} \approx 2\frac{\mathrm{e}\hbar}{2m_{\mathrm{e}}c}\frac{\left(\frac{\hbar}{2}\right)}{\hbar} = \mu_{\mathrm{B}} \tag{1.2}$$

where $g_s \approx 2$ is the g-factor of the S spin angular momentum of electrons. In 1921 Alfred Lande derived the so-called Lande factor, which is a g factor g_{J} incorporating the contributions from g_s and g_{L} which is used to calculate the total magnetic dipole moment of an electron by considering both the spin and orbital angular momenta **J** with the following expression

$$\mu_{\mathrm{J}} = -g_J\mu_{\mathrm{B}}\frac{\mathbf{J}}{\hbar} \tag{1.3}$$

where J arises from the spin-orbit interaction. In 1926 Pauli showed that no two electrons within an orbital could have the same four quantum numbers. The n, l, m_l quantum numbers define the shell shape and the orbital orientation of which electrons occupy. Thus each orbital can only hold up to two electrons with opposite spins. This principle is referred to as the Pauli exclusion principle. Consequently, the magnetic moments of paired electrons within an orbital are cancelled out. Additionally, the atom's electron configurations follow the Aufbau principle, which states that orbitals with lower energies are filled first, as well as the three empirical Hund's rules, which minimise the electrostatic (coulomb) energy and the spin-orbit interaction energy incorporated in J of the atom [60, 61]. Hund's rules imply that electrons

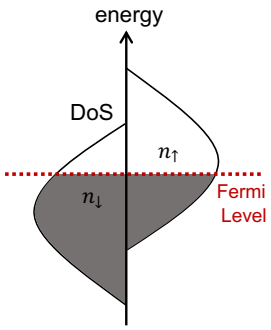

Figure 1.1: Illustration of the Stoner model of ferromagnetism, showing the density of states (DoS) bands split from which the spontaneous magnetisation is observed.

must first single-occupy all orbitals in a given subshell before double-filling them. However, the electrostatic field generated by the delocalised conduction electrons in metallic or semimetallic materials and the crystal fields reduces the orbital angular dipole moment, called orbital quenching [60]. Hence, the electron spins are the main contribution to the magnetic dipole moments measured experimentally in common magnetic materials such as 3d transition metals and ions, which can give rise to magnetic properties.

Magnetic ions are atoms or molecules with unpaired electrons in their outermost shell. Materials with filled orbitals are called diamagnetic and do not show any net magnetisation. Materials with partially filled orbitals often have thermally disordered magnetic ion orientations. These materials are referred to as paramagnetic and do not have long-range magnetic ion ordering [63]. In contrast, ferromagnetic materials lower their internal energy by adopting long-range magnetic ion ordering, which results in spontaneous magnetisation without any externally applied fields. This is due to the strong electrostatic electron-electron interactions and a large $n_\uparrow$, $n_\downarrow$ density of states near the Fermi level[60, 63]. In 1930 Edmund Stoner, by using a model where the conduction electrons in metallic and semimetallic materials are treated as an electron gas, showed that materials with a high density of states of electrons with $n_\uparrow$, $n_\downarrow$ near the Fermi Surface result in a spontaneous splitting of the $n\uparrow$ and $n\downarrow$ bands as shown in figure 1.1, which is called Stoner criterion [60].

One can assume that the magnetic moment of an electron equals one μ_B following equation

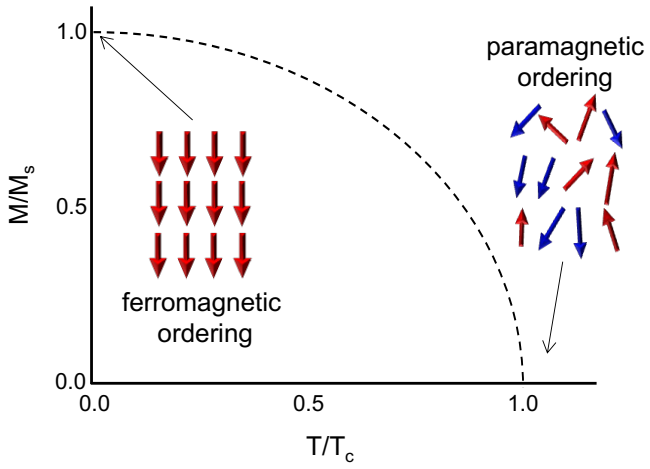

Figure 1.2: Phase transition from the ferromagnetic magnetic ordering to the paramagnetic. T_{C} denotes the Currie Temperature, and the arrows represent the spin moment vectors of individual magnetic ions.

1.2. Thus the spontaneous net magnetisation observed in materials which satisfy the Stoner criterion can be approximated as

$$M = \mu_{\mathrm{B}} \left(n_{\uparrow} - n_{\downarrow} \right). \tag{1.4}$$

Additionally, the magnetic ion alignment in ferromagnetic materials is subjected to thermal perturbations. As the temperature increases, the net magnetisation scales with Tk_{B}, opposing the energy responsible for the long-range alignment (exchange energy, introduced in section 1.4). Eventually, a critical temperature is reached where the thermal energy exceeds the exchange energy. The ferromagnetic material has thermally disordered magnetic moments. Figure 1.2 shows the corresponding phase transition. This critical temperature where the ferromagnetic to paramagnetic phase transition occurs is called Curie Temperature, T_{C}.

1.4 Magnetic Interactions

In magnetic materials that satisfy the Stoner criterion, the final magnetic configuration is determined by the minimisation of the energy terms given by a Hamiltonian. Depending on the

magnetic system of interest, different terms are included in the Hamiltonian to include all the effects of all the relevant interactions. In many magnetic thin films and the materials used in this project, five magnetic interaction energies are included, as shown below

$$E = E_{\mathrm{ex}} + E_{\mathrm{MAE}} + E_{\mathrm{z}} + E_{\mathrm{m}} + E_{\mathrm{D}} \tag{1.5}$$

where $E_{\mathrm{ex}}, E_{\mathrm{MAE}}, E_{\mathrm{z}}, E_{\mathrm{m}}, E_{\mathrm{D}}$ are the exchange, magnetocrystalline anisotropy, Zeeman, magnetostatic and DMI energies with units of energy. These interactions are introduced in the following section. From this point onward, spin is defined as a magnetic ion's total magnetic dipole moment direction noted as **S**, which is normalised with respect to μ_S.

1.4.1 Exchange Energy

Phenomenologically the exchange energy E_{ex} is minimised between two interacting spins aligned either parallel or antiparallel, depending on the sign of the exchange integral J. The exchange integral is a material-specific parameter. E_{ex} is a quantum interaction with no classical analogue. J is usually estimated using first principle electronic structure calculations or experimentally measured with techniques such as inelastic neutron scattering or resonant inelastic x-ray scattering (RIXS). For $J > 0$, the ferromagnetic alignment minimises energy between two spins giving rise to long-range magnetic order. For a ferromagnet, the exchange energy has the largest energy contribution compared to the other magnetic interactions. Its strength opposes the thermal perturbations; hence the stronger the E_{ex}, the higher the T_{C}. The interplay between the Coulomb interaction of an electron with its surroundings (other electrons and the atom nucleus) and the Pauli exclusion principle give rise to E_{ex}

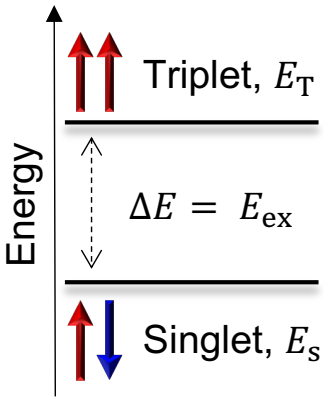

Figure 1.3: Energy difference between the singlet and triplet states

From quantum mechanics, it is known that there are four time-independent solutions for two interacting electron wavefunctions. Three solutions have spatial joint wavefunctions res-

ulting in a total spin $S = 1$. This is called triplet state,χ_{S}, which favours an antiparallel spin alignment ($\uparrow\downarrow$). Similarly, one state with anti-symmetric wavefunction where $S = 0$ called singlet state χ_{s}, with a parallel spin alignment ($\uparrow\uparrow$) [60]. The singlet and triplet states have different electrostatic interactions due to the spin orientations as illustrated in figure 1.3, and the exchange energy is the energy difference between these states. A more formal description of the Pauli exclusion principle than the one discussed in section 1.3.1 states that the overall wavefunction, Ψ with respect to exchange between electrons, must be antisymmetric [62]. The joint wavefunction between two electrons in separate atomic ions $\Psi = |\mathbf{r}\rangle|\psi\rangle$ includes the wavefunction's spatial and spin state parts. Following the Pauli exclusion principle

$$\left.\begin{array}{l} |\mathbf{r}\rangle \text{ symmetric} \sim |\psi\rangle \text{ antisymmetric} \\ |\mathbf{r}\rangle \text{ antisymmetric} \sim |\psi\rangle \text{ symmetric} \end{array}\right\} |\Psi\rangle = |\mathbf{r}\rangle|\psi\rangle \text{ antisymmetric} \tag{1.6}$$

The sign of J depends on the energy cost of the total wavefunction of the overlapping electron wavefunctions being in the singlet or triplet state. This can be further explained by considering two interacting electrons with states $\psi_a(\mathbf{r}_1)$ and $\psi_b(\mathbf{r}_2)$ with spatial coordinates $\mathbf{r}_1$ and $\mathbf{r}_2$. The interacting electrons are in a singlet or triplet state depending on the energy cost of each state E_{S}, E_{T} [60]. Thus the joint wavefunction for two electrons in the singlet Ψ_{s} and triplet states Ψ_{T} by considering the Pauli exclusion principle are the following [60]

$$\Psi_{\mathrm{s}} = \frac{1}{\sqrt{2}}\left[\psi_a(\mathbf{r}_1)\psi_b(\mathbf{r}_2) + \psi_a(\mathbf{r}_2)\psi_b(\mathbf{r}_1)\right]\chi_{\mathrm{s}} \tag{1.7}$$

and

$$\Psi_{\mathrm{T}} = \frac{1}{\sqrt{2}}\left[\psi_a(\mathbf{r}_1)\psi_b(\mathbf{r}_2) - \psi_a(\mathbf{r}_2)\psi_b(\mathbf{r}_1)\right]\chi_{\mathrm{T}} \tag{1.8}$$

and the energy difference between Ψ_{s} and Ψ_{T} is given by

$$E_{\mathrm{S}} - E_{\mathrm{T}} = 2\int \psi_a^*(\mathbf{r}_1)\psi_b^*(\mathbf{r}_2)\mathcal{H}\psi_a(\mathbf{r}_2)\psi_b(\mathbf{r}_1)d\mathbf{r}_1 d\mathbf{r}_2 \tag{1.9}$$

where $\mathcal{H}$ is the Hamiltonian of the system and by using the parameterisations for the singlet state of $\mathbf{S}_1 \cdot \mathbf{S}_2 = -\frac{3}{4}$ and $\mathbf{S}_1 \cdot \mathbf{S}_2 = \frac{1}{4}$ for the triplet state equation 1.9 can be written as an effective hamiltonian [60, 62]

$$\mathcal{H} = \frac{1}{4}\left(E_{\mathrm{S}} + 3E_{\mathrm{T}}\right) - \left(E_{\mathrm{S}} - E_{\mathrm{T}}\right)\mathbf{S}_1 \cdot \mathbf{S}_2 \tag{1.10}$$

By substituting equation 1.9 into the second term of equation 1.10 the exchange integral is defined as J often reffered as exchange costant

$$J = \frac{E_{\mathrm{S}} - E_{\mathrm{T}}}{2} = \int \psi_a^*(\mathbf{r}_1)\psi_b^*(\mathbf{r}_2)\mathcal{H}\psi_a(\mathbf{r}_2)\psi_b(\mathbf{r}_1)d\mathbf{r}_1 d\mathbf{r}_2 \tag{1.11}$$

Hence equation 1.10 is reduced too

$$\mathcal{H} = \frac{1}{4}\left(E_{\mathrm{S}} + 3E_{\mathrm{T}}\right) - 2J\mathbf{S}_1 \cdot \mathbf{S}_2 \tag{1.12}$$

Equation 1.12 is made of a constant and a spin-dependent part. The first term does not depend on the degrees of freedom of the system, in this case, spins. Thus, it does not affect equations of motion, and one can define an equivalent reduced to 1.12 as

$$\mathcal{H}^{\mathrm{ex}} = -2J\mathbf{S}_1 \cdot \mathbf{S}_2 \tag{1.13}$$

Then for $J < 0$, it is shown that $E_{\mathrm{S}} < E_{\mathrm{T}}$ which means it is energetically more favourable for spins to be in a singlet state (i.e. aligned) which results in ferromagnetic spin order. However, the example above includes only two interacting electrons. In this project, atomistic modelling is used, which includes hundreds of thousands of interacting, local spins. The exchange energy is then calculated using the Heisenberg exchange, defined as

$$\mathcal{H}^{\mathrm{ex}} = -\frac{1}{2}\sum_{\langle i,j \rangle} = J_{ij}\mathbf{S}_i \cdot \mathbf{S}_j \tag{1.14}$$

where $\langle ij \rangle$ denotes the nearest neighbouring atoms, and the $\frac{1}{2}$ is used to avoid double counting lattice points. In this thesis, only the nearest neighbours are considered in the Heisenberg exchange; since the thin films studied have direct exchange, which is often a short-range interaction, thus, negligible for the second nearest neighbouring atoms.

The type of exchange between two electrons whose wavefunctions overlap introduced here is often referred to as the direct exchange where J is uniform between neighbouring spins. However, in many cases, an indirect exchange is observed between electrons whose wavefunctions do not overlap, mediated through non-magnetic ions. Some common indirect exchange interactions are the superexchange in ionic solids such as MnO, the RKKY in specific metals and the double exchange in oxides [60, 61]. When the investigated materials possess any of

these types of exchange interactions, the next nearest neighbour interactions are considered to account for these interactions in the Heisenberg model.

1.4.2 Dyzaloshinskii Moriya Interaction (DMI)

DMI is an antisymmetric exchange interaction. It is induced when the centre between two spins i, j has broken inversion symmetry due to mediating heavy metal atom, often found in non-centrosymmetric systems. This induces a DMI vector, $\mathbf{D}_{ij}$ in which $\mathbf{S}_i$ and $\mathbf{S}_j$ are forced against the exchange order to be in right angles in a plane perpendicular to $\mathbf{D}_{ij}$ which strength is tuned by the Spin-Orbit (SO) coupling between the FM and heavy metal atom. This is illustrated in figure 1.4 where $\mathbf{D}_{ij}$ originates from the spin-orbit coupled $\mathbf{S}_i$ and $\mathbf{S}_j$ mediated by heavy metal atom. The Hamiltonian used for systems that exhibit DMI is

$$\mathcal{H}^{\mathrm{DMI}} = -\frac{1}{2}\sum_{\langle i,j\rangle} \mathbf{D}_{ij} \cdot (\mathbf{S}_i \times \mathbf{S}_j) \tag{1.15}$$

where $\langle i, j\rangle$ denotes the nearest neighbours. DMI can be induced in non-centrosymmetric bulk

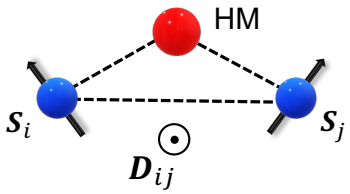

Figure 1.4: Illustration of the SOC of $\mathbf{S}_i$ and $\mathbf{S}_i$ shown as blue spheres with the heavy metal (HV) shown as a red sphere, located between $\mathbf{S}_i$ and $\mathbf{S}_i$ which breaks the inversion symmetry; resulting in the DMI vector $\mathbf{D}_{ij}$ direction.

materials such as MnSi. Additionally, DMI is induced in thin films with a ferromagnetic and a heavy metal layer with broken inversion symmetry at the interface. These two scenarios are illustrated in figure 1.5

DMI cants the spins $\mathbf{S}_i$ and $\mathbf{S}_j$ against the exchange energy; thus often referred to as a chiral interaction since it favours chiral spin alignment.

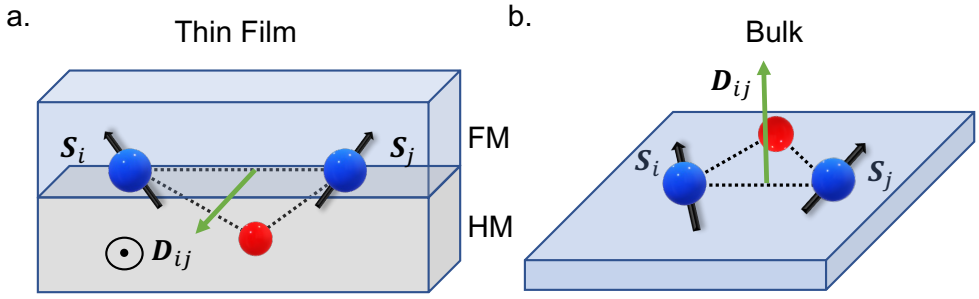

Figure 1.5: DMI vector $\mathbf{D}_{ij}$ directions induced (green arrow) a. at the interface of a thin film and b. in a bulk system. The blue and red spheres represent the ferromagnetic and heavy metal atoms, respectively. The black arrows on the ferromagnetic atoms show the spin directions at lattice sites i, j, $\mathbf{S}_i$ and $\mathbf{S}_j$. Illustration after [1]

.

1.4.3 Magnetocrystalline Anisotropy

Magnetocrystaline anisotropy refers to energetically preferred magnetisation and demagnetisation along specific crystalographic directions called ”easy axes” coupled with the system's symmetry. The magnetocrystalline anisotropy energy MAE, E_{MAE}, is induced from spin-orbit coupling (SOC) between the atomic nuclei and magnetic moments which follow the unit cell symmetry in crystalline materials. Thus rare-earth materials show larger magnetocrystaline anisotropies due to the larger crystal fields arising from their heavier nuclei (i.e. stronger SOC).

Hexagonal closed packed (HCP) and tetragonal crystal structures often have a uniaxial symmetry. Thus E_{MAE} can be described by an angle θ between the easy axis, which in the HCP cases is along the $\langle 0001 \rangle$ for HCP magnetic materials such as Cobalt with the following expression [60, 63]

$$E_{\mathrm{MAE}} = K_0 + K_1 \sin^2\theta + K_2 \sin^4\theta + ... \tag{1.16}$$

where K_0 and K_1 are the magnetocrystaline anisotropy constants in units of Joules. Similarly, face centre cubic (FCC), and body centre cubic (BCC) magnetic materials such as Fe - BCC and Ni - FCC have an easy axis along the $\langle 001 \rangle$ and $\langle 111 \rangle$ respectively. However, to describe

M along the cubic crystallographic directions, the directional cosines $\alpha_1, \alpha_2, \alpha_2$ are used as [60, 63]

$$E_{\mathrm{MAE}} = K_0 + K_1\left(\alpha_1^2\alpha_2^2 + \alpha_2^2\alpha_3^2 + \alpha_1^2\right) + K_2\left(\alpha_1^2\alpha_2^2\alpha_3^2\right) + ... \tag{1.17}$$

Like the easy axis, the intermediate and hard axes require a larger field to magnetise along. This section introduced the single-ion contribution to magnetocrystalline anisotropy, which is the most dominant in the lattices explored in this thesis. However, in non-cubic lattices and when the exchange interaction is not isotropic, one has to consider the two ion anisotropies by including additional terms in the Hamiltonian to account for anisotropic exchange and dipole-dipole interactions of the magnetic moments.

1.4.4 Zeeman Energy

In the presence of an external magnetic field **B** with units of A/m, the spins within a material experience a torque described by the Zeeman term

$$E_z = -\mu_0 \mathbf{M} \cdot \mathbf{B} \tag{1.18}$$

1.4.5 Magnetostatic Energy and Shape Anisotropy

The magnetic dipolar interaction is a long-range interaction between two magnetic dipoles. This interaction creates effective positive and negative charged poles within materials with long-range spin ordering, creating a magnetostatic field as shown in figure 1.6 a. The magnetostatic field is reduced by forming magnetic domains as illustrated in figure 1.6 b. and c. where a closed-flux domain structure is shown.

The magnetostatic energy is given by

$$E_{\mathrm{m}} = -\mu_0 \int_{\mathrm{V}} \mathbf{H}_{\mathrm{d}} \cdot \mathbf{M} dV \tag{1.19}$$

where $\mathbf{H}_{\mathrm{d}}$ is a demagnetisation field that opposes the magnetisation **M** to minimise the stray field, which is reduced by the creation of domains and minimised the most for a closed flux domain. Then it follows that E_{m} is minimised when **M** lies along the long axis of the element. The internal demagnetisation field due to effective poles created **M** is estimated by

$$\mathbf{H}_{\mathrm{d}} = N_{\mathrm{d}}\mathbf{M} \tag{1.20}$$

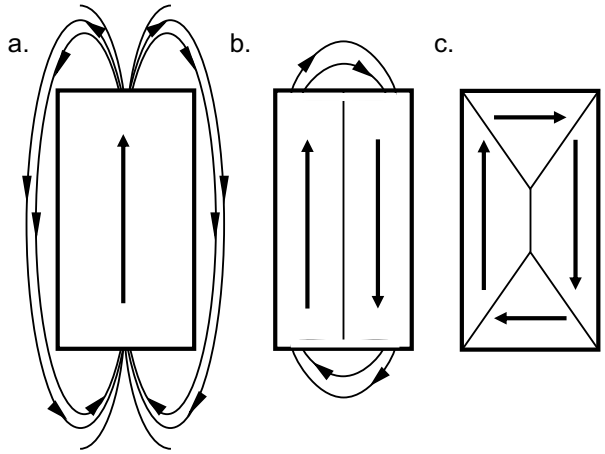

Figure 1.6: Illustration of the magnetostatic field reduction due to magnetic domain formation. a. shows a single domain structure magnet, b. a two domain magnet and c. a magnet with flux closure domain structure

where in the simplest case of a uniformly magnetised sample

$$N_{\mathrm{d}} = \begin{pmatrix} N_x & 0 & 0 \\ 0 & N_y & 0 \\ 0 & 0 & N_z \end{pmatrix} \tag{1.21}$$

N_d is called the demagnetisation factor, which trace equals 1 [60]. Thus different shapes of magnetic elements have different shape anisotropy where preferred de-magnetisation directions minimise the internal energy.

1.5 Magnetic Thin Films

In this thesis, skyrmions at interfaces in thin films are studied; thus, this section introduces the main features and differences between thin films compared to bulk materials. With the advances in chemical vapour deposition in the 1970s, thin film magnetism emerged [64]. Magnetic thin films are multilayered structures composed of atomically thin up to approximately 100 nanometers of layer thicknesses grown with techniques such as molecular beam epitaxy and pulsed laser deposition, showing incredible precision in depositing atoms on a substrate.

The low dimensionality of the layers and the interfaces between layers can alter the magnetic properties observed in bulk magnetic materials. In low-dimensional materials, the coordination number of atoms on the surface is lower than in bulk. This increases the population of magnetic spin DOS near the fermi surface, which promotes non-ferromagnetic materials to satisfy the Stoner criterion [60, 62]. More important for this project is the anisotropy change and broken inversion symmetry at the interfaces. Due to the symmetry change at the surface of the thin film (or interface), the anisotropy constant is replaced with an effective anisotropy constant K, which includes the effects of the low dimensionality as

$$K = \frac{2K_{\mathrm{s}}}{t} + K_{\mathrm{vol}} - \mu_0 \mathbf{M}^2 \tag{1.22}$$

where K_{s} is the surface anisotropy constant and t is the thickness of the layer, K_{vol} is the volume anisotropy and the third term $\mu_0 \mathbf{M}^2$ is the shape anisotropy. And the magnetic anisotropy in a thin film is estimated as [60]

$$E_{\mathrm{an}} = K \sin^2 \theta \tag{1.23}$$

The coordination number reduction and symmetry at the surface of the layer induce surface anisotropy. The surface anisotropy is reduced by spins aligned out-of-plane, opposing the shape anisotropy where the spins are aligned within the plane to reduce the magnetostatic field. As shown in 1.22, the effect of the surface anisotropy increases with decreasing layer thickness. There is a Perpendicular Magnetic Anisotropy (PMA) for thin enough layers. The volume anisotropy incorporates the effects of lattice stresses and strains, which can change the anisotropy. It is important to note that the dipolar interactions in thin film simulations are often included as an effective shape anisotropy in atomistic modelling; since its effect is small. However, computing the dipolar interactions of hundreds of thousands of spins is computationally expensive. Additionally, PMA can be induced or enhanced by placing a layer of heavy metal atoms above the ferromagnetic layer. In this case, the large spin-orbit coupling enhances the PMA. Thin films can also be grown in different crystalographic metastable phases, stabilised by the lattice strains. For example, Fe has a BCC crystal structure at room temperature in bulk. However, Fe is often grown in thin films with an FCC(111) crystal structure to enhance certain interactions, such as the DMI. More importantly, the interface between layers of different elements or

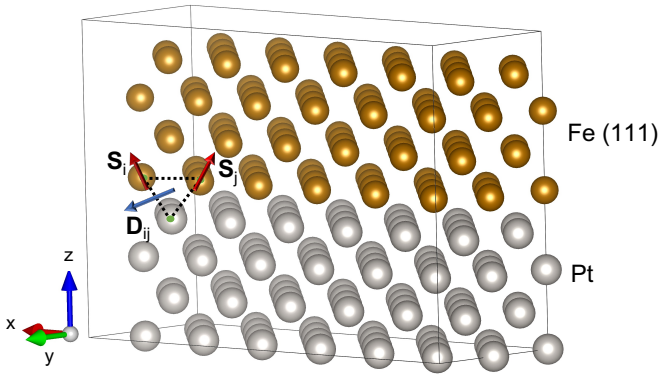

Figure 1.7: An example of a uniform interfacial DMI induced at the interface between a Fe and Pt thin-film

compounds in thin films has broken inversion symmetry. Thus, interfacial DMI can be induced by growing thin film stacks with a ferromagnetic and heavy metal layer. This is illustrated in figure 1.7

1.6 Magnetic Domain Walls

Magnetic Domains form to reduce the magnetostatic energy of a magnetic system, as shown in figure 1.6. The magnetic domain wall (DW) is a transition region between magnetic domains. The abrupt change of the adjacent spin directions between two neighbouring domains costs a lot of exchange energy [63]. Thus domain walls are formed to minimise this excess energy. Within a DW, the spin direction shifts in or out of the plane depending on the system's geometry. Bloch domains are favoured in bulk systems where the magnetisation rotates normal to the DW plane. In thin-film systems, Néel type DWs are energetically more favourable where the magnetisation rotates within the domain wall plane. The profiles of the two types of DWs are illustrated in figure 1.8.

In nanowires, it is possible to have isolated Néel DWs. When an external field is applied, the magnetic domain expands by moving the DW to minimise the Zeeman energy. Many spintronic devices currently use DWs in nanowires since they can be generated, moved and

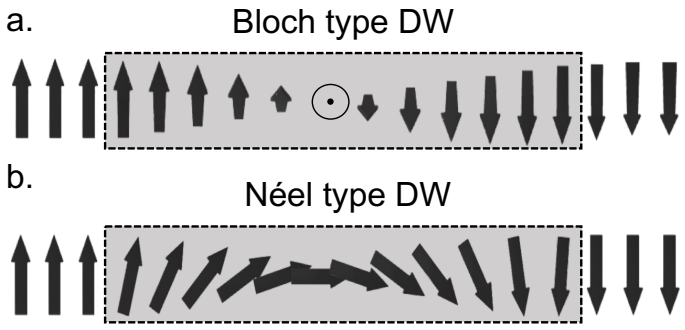

Figure 1.8: a. Bloch and b. Néel type domain wall profiles

are easy to detect since their magnetisation point in a different direction with respect to the nanowire's magnetisation. There are a lot of spintronic beyond von Neumann proposed device architectures with the use of DWs and storage devices such as racetrack memories. However, for computational needs, the manipulation of DW motion must be deterministic and easy to stop in specific regions within a device for operations like reading and writing. As demonstrated, DW motion is stochastic and thus cannot be used for deterministic computations or storage devices [27]. However, other concepts where circular nanowires are referred to as nanorings with DWs fabricated next to each other are proposed to be used as future image recognition or probabilistic computing applications by utilising the coupling of the DWs in neighbouring nanorings [29, 65].

1.7 Magnetic Skyrmions

Magnetic skyrmions are non-collinear swirling magnetic spin textures illustrated in figure 1.9. Their integer topological charge value, Q, characterises them, corresponding to the $\mathbf{M}$ rotation covering the whole unit sphere, often referred to as winding or skyrmion number. In 2D systems Q is defined as:

$$Q = \frac{1}{4\pi} \int \int \mathbf{M} \cdot \left(\frac{\partial \mathbf{M}}{\partial x} \times \frac{\partial \mathbf{M}}{\partial y} \right) dxdy \tag{1.24}$$

The skyrmion spin texture results in an integer $Q = \pm 1$, which differs from a ferromagnet, $Q = 0$. Hence skyrmions are often said to be topologically protected, which is often colloqui-

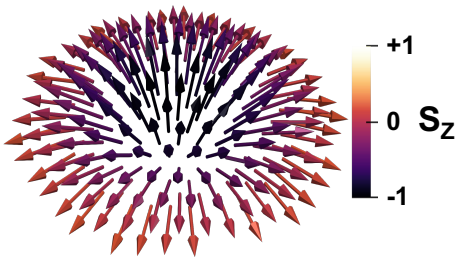

Figure 1.9: Néel skyrmion spin texture profile.

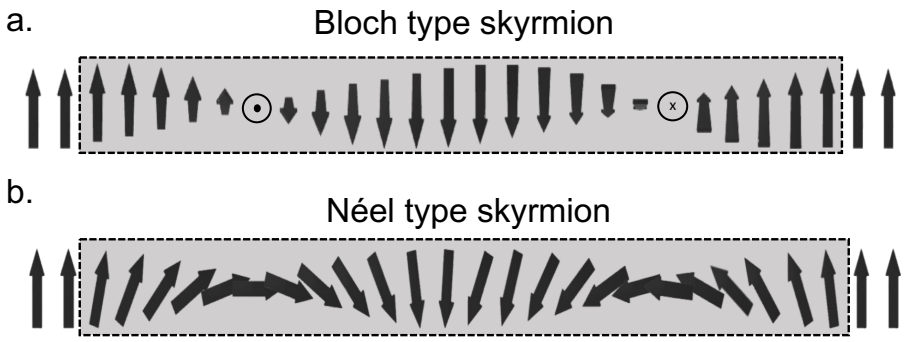

Figure 1.10: a. Bloch and b. Néel type skyrmion profiles

ally interpreted as magnetic skyrmion stability. Practically, skyrmions are stabilised through their topology but; in real systems, skyrmions can be destroyed through perturbations since the assumption of continuous field breaks from many factors, such as lattice finite sizes and defects. Thus magnetic skyrmions are stabilised due to their distinct topology instead of having topological protection. Skyrmions can exist in non-centrosymmetric magnetic bulk and thin-film systems with broken inversion symmetry with a strong DMI interaction. Two mainly used and studied types of skyrmion configuration profiles are illustrated in figure 1.10, which depends on the direction of $\mathbf{D}_{ij}$ vector. As illustrated in Bloch and Néel type skyrmions, the magnetisation rotates 360 degrees perpendiculars and in-plane along the skyrmion diameter, respectively. When DMI is present in bulk systems, the DMI energy is minimised when the

magnetic moments mediated by the HM are aligned perpendicular to the plane normal to $\mathbf{D}_{ij}$ and Bloch-type skyrmions are shown to be stabilised as a groundstate skyrmion lattice. In contrast, isolated Néel-type skyrmions can be formed in thin films as metastable spin excitations. Skyrmions can also be stabilised in other systems without DMI, such as helimagnets and frustrated spin textures. The magnetic skyrmion diameters depends in the interplay of the E_{ex}, E_{an} and E_{DMI}. A strong DMI favours big skyrmion radii, whereas, with increasing anisotropy, skyrmions shrink. However, in thin-film, the DMI and PMA are stronger; thus, sub $10\mathrm{nm}$ skyrmions have been stabilised without the need for an applied external field [66]. The exchange, anisotropy and DMI strengths scale with temperature and depend on the coordination number of the system. Thus due to thermal perturbations, skyrmions size changes due to the exchange, anisotropy and DMI energy variations. Similarly, lattice defects such as non-magnetic impurities and vacancies locally change the value of exchange, anisotropy and DMI [55, 67]. Additionally, skyrmions have internal dynamic modes referred to as breathing modes which are coupled oscillations under the influence of an external magnetic field with specific oscillation frequencies depending on the strength of the field [68]. Figure 1.11 shows the analytically calculated DMI vector directions for a FE(FCC(111)Pt multilayer. A Python script is developed for this calculation with a thin film lattice as an input parameter. The script identifies the lattice points of the FM and HM atoms at the interface within the lattice. Then the script loops through every single FM lattice point, identifies its nearest FM and HM neighbours and constructs the plane (red plane) in which the $\mathbf{D}_{ij}$ is calculated from. This script is intended to be used for visualisation and the explicit calculation of the $\mathbf{D}_{ij}$ in lattices with non-magnetic defects where the symmetry of the lattice is broken. The total DMI experienced for a selected magnetic ion (green) is the sum over all the neighbouring sets of triplets, including the 2 magnetic ions coupled with the Pt atom at the interface. This example demonstrates the big effect of non-magnetic lattice defects.

Similarly, E_{D}, E_{ex} and E_{MAE} locally change for magnetic impurities. The change of these energies for the magnetic impurities is studied using DFT calculations which do not include any temperature effects [69]. Likewise, for non-magnetic lattice defects, the methods used often do not fully account for thermal effects [2, 4, 54, 55]. This was one of the main drives of this

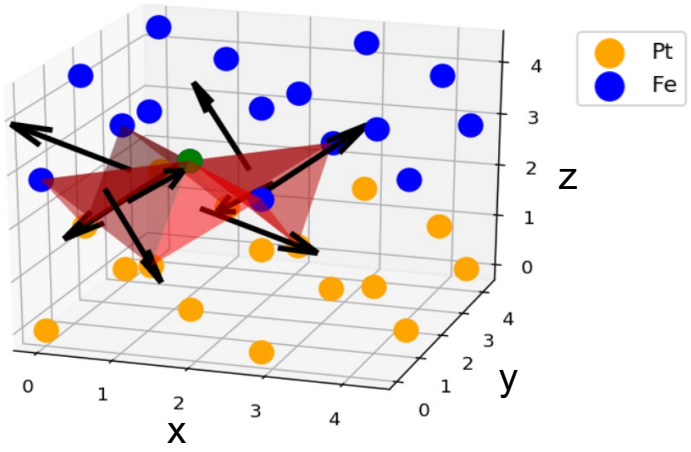

Figure 1.11: 3D PtFe(111) induced interfase DMI. The plane between the 2 Fe magnetic ions coupled with the Pt atom is the red area in 3D for the magnetic ion selected (green colour). The arrows represent the direction of the DMI vector $\mathbf{D}_{ij}$.

project, where a method that will allow the study of the effect of these defects was developed, which opens a new avenue that has not been explored yet.

Interfacial magnetic skyrmions have attracted much interest due to their particle-like behaviour and small sizes. Much research has focused on understanding their motion, suppressing the so-called skyrmion Hall effect, and understanding the effect of lattice defects in creating and annihilating skyrmions [1]. Unfortunately, experimentally observing skyrmions has proven to be a hard task. Still, no general analytic model for skyrmion dynamics exists, including the effects of temperatures and/or lattice defects. However, for any future proposed spintronic device, it is crucial to quantify the skyrmion creation and annihilation energies to examine the stability and reliability of any proposed device. Many proposed skyrmionic device architectures include the interaction of skyrmions with other spin textures such us skyrmioniums (skyrmions with an outer domain with opposite polarity relative to its core), magnetic bubbles and systems with the coexistence of skyrmions with other spin textures. The method demonstrated in this project also has the ability to examine the coexistence of skyrmions with any other spin texture in any skyrmion host systems while fully accounting for temperature effects. In the following section, an introduction to the multiscale modelling of magnetism is introduced prior to the dis-

cussion of the techniques used to examine and quantify the skyrmion energies and interactions described while highlighting the limitations and benefits of each method.

1.8 Multiscale Magnetic Modelling

Multiscale magnetic material modelling refers to the techniques and formalisms used to simulate different interactions and behaviour of magnetic systems occurring at different lengthscales and timescales. Moving from the smallest timescales to the largest, different parameters are calculated. These are then used as input parameters in larger-scale simulations, allowing large magnetic systems and devices to be simulated [70, 71]. This is due to the computational limitations of the current CPUs and GPUs, which require simplifying the calculations and use of approximations in order to simulate larger systems at a device level for longer timescales in a single simulation. Figure 1.12 summarises the main simulation formalisms with their approximated simulation scales.

In the first principle (often referred to as ab initio) calculations, it is assumed that the wavefunction of a system can be decomposed into single electron wavefunctions where the eigenstates of the non-relativistic time independent Shrödingers equation are aimed to be identified. One of the aims of the ab initio calculations relevant to this discussion is to study the electronic structure of materials and identify their ground state. However, the density functional theory approaches are most often employed since the ab initio calculations are becoming more complex with systems with more electrons (many body systems). DFT describes the electron wave functions in terms of local electronic charge densities and potentials used to identify a system's ground state. There are vastly different formulations of DFT used to solve different problems, and a thorough review is given at [72]. In magnetism, DFT is used to calculate magnetic material constants such as magnetic moment, exchange integrals, and anisotropy constants which depend on the electronic structure of the materials [70, 71]. The first principle calculation (including DFT) is a zero temperature formalism, and the complexity of the calculations increases the computational cost of these; thus, only a few hundred atoms can be simulated.

The material-specific constants calculated from the electronic mapping in DFT are then

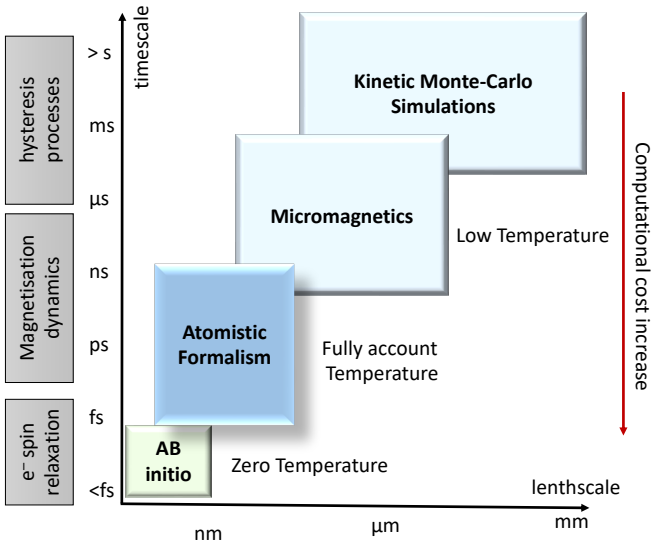

Figure 1.12: Multiscale magnetic material modelling techniques times and scales

used as input parameters in atomistic simulations, where the interaction of local magnetic moments is simulated. The strength of the interactions between the constants is calculated using the first principle (DFT) simulations, which are used in a Hamiltonian describing the energy of each lattice point. Any thin film and crystal structure can be simulated using the predefined lattice. Up to a few hundred of thousand atoms, allowing the calculation of the magnetisation dynamics up to a few nanoseconds and calculating thermodynamic equilibrium properties of a given system, such as the magnetisation at a temperature T, $M(T)$, $D(T)$, $J(T)$, by thermalising the lattice using sampling techniques such as the Metropolis Monte Carlo algorithm. This length scale fully accounts for temperature effects due to the large population of interacting spins $\mathbf{S}$ allowing statistical calculations in the canonical ensemble. Atomistic formalism often uses a classical thermostat with the Boltzmann statistics. However, semiclassical approaches have recently arisen using a semi-classical quantum thermostat with Bose-Einstein statistics [73]. With the quantum thermostat, there are less thermal artefacts often introduced by the classical approaches. In this project, atomistic simulations are combined with an enhanced sampling technique called metadynamics. This is introduced in the next section and detailed and discussed in section 2.

Micromagnetics often use the thermodynamic averages estimated by atomistic simulations to simulate the magnetisation dynamics and hysteresis processes of larger magnetic systems and devices up to a few micrometres. This well-established formalism is the most widely used to support and explain the origin of experimental results and design new spintronic devices. Micromagnetics is a finite difference formalism where the system is discretised into cells smaller than the exchange length, where the magnetisation is assumed to be uniformly aligned, thus having an effective constant magnetisation vector whose size is calculated from atomistic simulations for a given temperature [74, 75]. Micromagnetics is the most widely used formalism due to the introduction of well-established GUI software such us MuMax3 [76], OOMMF [77] and fidimag [78], which have shown incredible success validating experimental measurements. However, there is a lot of debate about the validity of many studies using these softwares, for simulations in temperatures close to the Curie temperature of the system. This is due to the main limitation of micromagnetics, which is the treatment of finite temperature effects. Micromagnetics discretise the system into cells that have constant magnetisation, thus, can not account for thermal effects and the coupling between spins resulting in the magnon-magnon interactions (waves within the spin precession). Hence, micromagnetic simulations often are inaccurate for temperatures where magnon-magnon interactions dictate the magnetisation dynamics. However, stochastic noise can be introduced to the micromagnetic simulations at low temperatures, interpreted as thermal noise [79]. This is of crucial importance for spin texture stability studies, where temperature effects have the ability to annihilate the spin structures. Additionally, skyrmion stability phase diagrams indicate the anisotropy and DMI strength fraction ranges that skyrmion may be stable. However, for finite temperatures, these stability windows might be inaccurate. Thus, often it is argued that micromagnetic simulations are misleading for these kinds of stability studies [80].

1.9 Skyrmion Metastable Energies and Thermal Stability Calculations

The thermal stability of skyrmions is crucial for the realisation of interfacial skyrmionic devices since it will dictate the reliability of these devices. It has been demonstrated, both experimental and theoretically, that the skyrmion stability depends on the skyrmion's internal energy ΔE and the change of the configurational entropy between a skyrmionic and a ferromagnetic state ΔS [4, 81, 82]. ΔE and ΔS create an energy barrier stabilising skyrmions against thermal fluctuations. However, thermal fluctuations can still result in annihilation affecting the operation of a device. Additionally, lattice defects and the finite size of the devices alter their metastable energy [2, 3, 55]. Even more important is to identify the lifetime of skyrmions to assess if a system can be used as non-volatile information storage. Multiple computational studies have demonstrated that skyrmions have three main ways of annihilation in confined geometries, such as nanowires [2, 3]. First, they can be annihilated as singularities, where a single spin within the skyrmion texture is reversed, resulting in skyrmion shrinkage or progressively annihilating around the singularity. Secondly, they can be annihilated by collapsing, where they shrink and slowly revert their spins around the skyrmion's outer circumference. Lastly, it is reported that the minimum energy path for skyrmion annihilation is from the system's boundaries [2, 3]. Hence the metastable skyrmion energy barrier must be quantified at finite temperatures, including the contributions of ΔE and ΔS.

However, all the computational methods use low or no-temperature techniques to calculate the skyrmion metastable energy with atomistic or micromagnetic simulations [2, 4, 54]. Additionally, the methods used to calculate the skyrmion creation and annihilation energy barriers only include the contribution of ΔE. Moreover, the skyrmion lifetimes are calculated using these estimations of the energy barriers and debatable assumptions using a Néel Arrhenius type equation,

$$\tau = \tau_0 \exp\left(\frac{-\Delta E}{k_\mathrm{b} T}\right) \tag{1.25}$$

where T is the Temperature in Kelvin, τ_0 is the attempt frequency and ΔE is the skyrmion metastable energy. In reported studies, ΔE is estimated from low or no temperature tech-

niques, and the τ_0 is assumed to be in the GHz range [2, 3, 22, 54, 55]. Likewise, the estimated skyrmion lifetimes are based on equation 1.25 using the energy barrier for 0K with the arbitrarily chosen τ_0, which can be used as a rough approximation. However, it has been experimentally demonstrated that the order of magnitude of τ_0 changes up to 30 orders in finite temperatures [82]. More importantly, these studies report only the minimum energy paths. As a recent theoretical study which includes citations of experimental results which also validate their theoretical findings, equation 1.25 assumes infinite time scales, where the most probable diffusion or a transition occurs through the minimum energy path [83]. For finite timescales, higher energy paths can be more probable [83]. This highlights the importance of identifying all possible transition paths.

In this thesis, we mainly demonstrate a computational technique to calculate the skyrmion metastable energy in finite temperatures, including the contributions from both the ΔE and ΔS while revealing and quantifying all the possible transition paths from the skyrmionic to the ferromagnetic state and vice versa. The method presented in this thesis can be applied to any lattice, with or without defects, and we also propose an accurate calculation of τ_0 in section 6. This method can be used for future studies for the design, material selection or realisation of skyrmionic devices. As is later discussed, this novel way can also be used for many other investigations regarding extracting metastable energies and identifying all possible spin textures and their transitions between different metastable states.

1.9.1 Skyrmion Energy Landscape Calculations

Currently, atomistic or micromagnetic simulations combined with the Geodesic Nugded Elastic Band Methods (GNEBM) are used to reconstruct FELs and extract only the minimum skyrmion metastable energy, a zero-temperature technique [52]. As this project demonstrates later in section 4, there are more paths to create and destroy a skyrmion, which are often the more realistic experimental paths, even if larger energies are required. As stated before, higher energy paths become more probable in finite timescales [83]. Additionally, micromagnetic studies can not accurately represent the skyrmion annihilation paths as a singularity. This is because micromagnetic cells correspond to a large physical number of individual spins with an effective total

magnetisation in each cell.

The GNEBM was first used to calculate the skyrmion metastable energy in 2015 [52]. GNEBM finds the minimum energy path between initial and final spin-textures in magnetic systems. In GNEBM, the initial and final states are manually input as a set of spins which are referred to as images $\mathbf{Y}_0$ and $\mathbf{Y}_\mathrm{N}$ each having its own energy $E(i)$, separated by bands of images as illustrated in figure 1.13. The algorithm works by finding the minimum energy path between $\mathbf{Y}_0$ and $\mathbf{Y}_\mathrm{N}$. The resulting energy landscape axis is the energy between different images E_i versus their distance y from the initial image as phase transition with unknown order parameters (i.e. arbitrary units). Thus the resulting energy landscape from GNEBM has abstract dimensions, which don't contain any information for the physical transition between the two states. This method samples only the saddle points of the energy landscape, not the whole energy landscape. Hence can not identify other metastable states, and often the final shape of the energy landscape is inferred instead of being calculated[2].

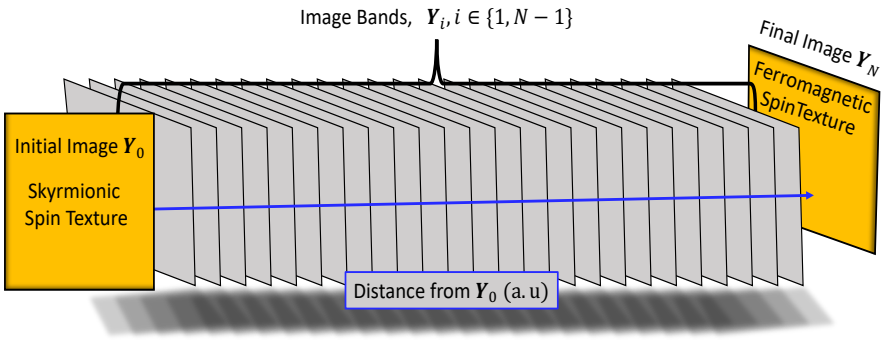

Figure 1.13: GNEBM illustration. The yellow boxes represent the initial and final spin texture images that must be predefined. These images are separated by the image bands represented by the grey boxes. The algorithm identifies the minimum energy to transition between the initial and final images through the image bands. Hence the reaction coordinate is the distance between the images, which is simplistically illustrated as the blue line

1.9.2 Skyrmion Free Energy Landscape with Metadynamics

The Free-Energy Landscapes (FEL) of specific skyrmion degrees of freedom must be reconstructed in finite temperatures to calculate the skyrmion metastable energies. The FEL are maps showing the free energy differences associated with the degrees of freedom used to reconstruct them. The FEL is then used to calculate the associated energy barriers between points of interest, including the contributions of ΔE and ΔS.

In contrast with the previous studies [2, 3, 22, 54, 55], this project combines atomistic simulations with an enhanced sampling technique called metadynamics which is a detailed discussion in section 2. Atomistic modelling is a sampling technique that can sample a local region along the FEL for a given finite temperature, discussed in section 2.2.2. Metadynamics was introduced in 2002 by Alessandro Laio and Michele Parrinello [84]; an enhanced sampling technique used to explore rare events. Metadynamics push the system over energy barriers along the FEL; sampling the whole FEL associated with the degrees of freedom selected; this thesis demonstrates that with this novel procedure developed, the FEL is reconstructed for specific skyrmion degrees of freedom. It is found that compound axes of the out-of-plane magnetisation and the topological charge describe the physical transition from the skyrmionic to ferromagnetic states. The reconstructed FEL allows the calculation of the skyrmion metastable energies and shows all the possible spin-textures that can be stabilised or coexist in any system. Additionally, this method allows us to investigate how the FEL changes as a function of temperature. Finally, with this method, it is demonstrated that we can recreate a thermalised skyrmionic lattice for a given temperature, which can allow the calculation of τ_0.

Metadynamics is a well-established technique used in many branches of science, such as chemistry and materials science [85, 86]. Traditionally it has been used to investigate how molecules bind to surfaces, but here it is used to explore the metastable energy of spins textures. This method is rarely used in condensed matter magnetism. However, recently it has been used to explore the temperature dependence of the magnetocrystalline anisotropy and spin-reorientation transitions of thin films and the creation of vortices [87, 88]. However, this study is the first that uses it in topological spin structures in condensed matter. Compared with the GNEBM, the initial and final spin configurations are not required. This gives the advantage

of using the method we show to investigate if any topological spin texture will be present in any system and open a new avenue for future studies. As it is demonstrated in section 4.3, metadynamics pushes the systems to explore all the possible spin textures possible within the configurational space defined by the CVs used, which, if a spin texture is metastable it will have a minimum region on the reconstructed FEL. Furthermore, the axes of the reconstructed FEL are not abstract, showing the full transition path between possible states. This method accounts for thermal effects and is able to study the stability of skyrmion, helping to investigate how the stability of any device can be improved, either by a material selection process or geometries where our method will show how the FEL is affected. On the downside, the calculations of the CVs can be very computationally expensive, making the metadynamics simulations limiting.

CHAPTER 2

Methodology

In this research project, magnetic atomistic simulations solved with the metropolis Monte Carlo algorithm are adapted to metadynamics to reconstruct the free-energy landscapes (FEL) of skyrmion host systems to study their thermal stability.

This chapter introduces and discusses the main principles of the Monte Carlo techniques, Metropolis Monte Carlo algorithm and metadynamics. Due to this project's nature, these methods' backgrounds are introduced here, and in later chapters, the development of new novel approaches and their validation is discussed. These methods developed allowed the successful outcome of this project and provided a new approach for thermal stability studies of spin textures.

2.1 Atomistic Modelling

As discussed in section 1.8, atomistic modelling is a formalism that naturally includes finite temperature effects in contrast with micromagnetics which is, in principle, an athermal formalism. This is because micromagnetics is a continuum formalism whose length scale can not account for thermal fluctuations of individual magnetic moments due to the discretisation of the system simulated. On the other hand, atomistic modelling considers a lattice consisting of individual localised classical magnetic moments at each lattice point. Thus allowing calculations of the canonical ensemble. Here, atomistic modelling is used to calculate the macroscopic thermodynamics of a magnetic system by solving the microscopic degrees of freedom. Prior to the simulation, the location of the magnetic moments within the lattice is pre-defined. Thus allowing the simulation of multilayer or single-layer thin film structures of specific crystallographic orientations and interfaces with or without lattice defects.

The total energy of the lattice is given by a Hamiltonian which includes all magnetic interactions present in the magnetic system of interest based on the physical basis of the system studied. This is because different systems and heterostructures have different interactions and couplings between atoms; thus, one needs to consider the physical basis of these interactions and include all the relevant terms in the Hamiltonian in the systems studied. This project considers mainly skyrmion host thin films with broken inversion symmetry at the interfaces. The

Hamiltonian, which considers the physical basis of these systems, is the following

$$\mathcal{H} = -\frac{1}{2}\sum_{\langle \mathrm{i,j}\rangle} J_{\mathrm{ij}}\mathbf{S}_{\mathrm{i}}\cdot\mathbf{S}_{\mathrm{j}} - \sum_{\mathrm{i}}\mu_{\mathrm{s}}\mathbf{B}\cdot\mathbf{S}_{\mathrm{i}} - K_{\mathrm{u}}\sum_{\mathrm{i}}(\hat{\mathbf{e}}\cdot\mathbf{S}_{\mathrm{i}})^2 - \frac{1}{2}\sum_{\langle \mathrm{i,j}\rangle}\mathbf{D}_{\mathrm{ij}}\cdot(\mathbf{S}_{\mathrm{i}}\times\mathbf{S}_{\mathrm{j}}) \tag{2.1}$$

where $\langle \mathrm{i,j}\rangle$ denotes the nearest neighbouring lattice points $\mathrm{i,j}$. J_{ij} and K_{u} are the scalar quantities describing the exchange and uniaxial anisotropy respectively in units of energy, $\mathbf{S}_{\mathrm{i}}$ and $\mathbf{S}_{\mathrm{j}}$ are spin vectors at sites $\mathrm{i,j}$.K_{u} often is used as an effective anisotropy, including all the anisotropy contributions as shown in equation 1.22. $\hat{\mathbf{e}}$ a unit vector along the uniaxial easy axis and $\mathbf{D}_{\mathrm{ij}}$ is the DMI vector direction which depends on the relative positions of $\mathrm{i,j}$ with a mediated non-magnetic heavy metal atom as shown in figure 1.4. μ_{s} is the atomic magnetic moment with units of JT^{-1} and $\mathbf{B}$ is the external applied field with units of Tesla.

The first term in equation 2.1 is the isotropic Heisenberg exchange which considers the nearest neighbouring spins and has the highest energy contribution. The factor of $\frac{1}{2}$ accounts for the double counting in the summation, and in the literature, they are often written with different conventions. The sign of J dictates the symmetry of neighbouring spins with positive J resulting in ferromagnetic alignment and a negative J in antiferromagnetic alignment. For the positive and negative J, the energy is minimised by the spins being aligned in parallel and antiparallel, respectively. The exchange interaction is not isotropic in many systems since it can have different strengths in different crystallographic directions. The second term is the Zeeman term, where $\mathbf{B}$ is the external magnetic field in units of Tesla. The Zeeman terms account for the interaction of a magnetic spin with the external field, and its energy is minimised when $\mathbf{S}_{\mathrm{i}}$ is aligned with $\mathbf{B}$. The third term accounts for the uniaxial magneto-crystalline anisotropy of the system, which is often referred to as single ion anisotropy since the local site symmetry determines its energetics, and it can be described only from a single atom in the Hamiltonian. The energy of this term is minimised when $\mathbf{S}_{\mathrm{i}}$ is aligned with the unit vector $\hat{\mathbf{e}}$ and depends on the sign of K_{u}.

The fourth term accounts for the DMI, which is present in non-centrosymmetric systems such as bulk crystals or the interfaces between a magnetic and a heavy metal atom. In the second case, the coupling between a mediating heavy metal atom between two magnetic atoms results in larger DMI values due to the large spin-orbit coupling. Additionally, in atomistic

modelling, the spin-orbit coupling of heavy-metal atoms above or below the magnetic atoms layers is included in the DMI term. In terms of a tensor the DMI is given from an exchange tensor

$$\mathbb{J}_{ij} = \begin{pmatrix} 0 & -D_{ij}^{z} & D_{ij}^{y} \\ D_{ij}^{z} & 0 & -D_{ij}^{x} \\ -D_{ij}^{y} & D_{ij}^{x} & 0 \end{pmatrix} \tag{2.2}$$

This exchange tensor is mathematically skew-symmetric. Thus, often the DMI is referred to as an antisymmetric exchange. Phenomenologically, DMI favours neighbouring spins aligned at right angles. In contrast, the exchange favours collinear spin alignment for $+J$. Thus in a ferromagnet, the DMI results in spins being canted.

Due to the energetic interplay between all the Hamiltonian terms, the resulting spin textures within the lattice result from the competing interactions of the Hamiltonian terms for a given temperature.

2.2 Monte Carlo Simulations

In the context of atomistic modelling in magnetism, Monte Carlo techniques are used to estimate mean thermodynamic values, understand thermal effects and equilibrate the initial lattice configurations at finite temperatures. Here I introduce the general concepts of Monte Carlo techniques before discussing how they are used in statistical physics and which algorithms are employed for the atomistic simulations in this project.

Monte Carlo techniques are used to estimate expectation values, $\mathbb{E}_p\left[f(\mathbf{x})\right]$ of a function $f(\mathbf{x})$ where $\mathbf{x}$ is a vector of random variables using a probability density function $p(\mathbf{x})$ as shown bellow for a single dimensional case

$$\int p(\mathbf{x}) f(\mathbf{x}) \mathrm{d}x = \mathbb{E}_p\left[f(\mathbf{x})\right] \tag{2.3}$$

Monte Carlo techniques are mainly employed in cases where the physical parameter space is multi-dimensional [89–91]. This is because solving analytically high multidimensional integrals is tedious, if not impossible. For example, in statistical physics, we integrate kinetic equations, which are equal to the degrees of freedom of the system studied. Hence for systems with many degrees of freedom, it is impractical to calculate them analytically. For example, in atomistic modelling, a single $\mathbf{S}_\mathrm{i}$ has two degrees of freedom, the azimuthal and polar angles when polar coordinates are used. Hence in a $100 \times 100 \times 100$ lattice, there are 2 million degrees of freedom; hence Monte Carlo algorithms are used.

Monte Carlo techniques work by utilising the pseudorandom number generators in computers to generate a subset of sampling values x_l, creating a subset of the $\{\mathbf{x}\}$ drawn from the $p(\mathbf{x})$, from which the $\mathbb{E}_p\left[f(\mathbf{x})\right]$ is estimated as arithmetic average. In simple sampling Monte Carlo techniques, the average formula used is [90, 92]

$$\mathbb{E}_p\left[f(\mathbf{x})\right] \approx \frac{1}{\mathrm{N}} \sum_{\mathrm{l}=1}^{\mathrm{N}} f(x_\mathrm{l}) \qquad x_\mathrm{l} \sim p(\mathbf{x}) \tag{2.4}$$

where N is the number of sampling points, x_l are the randomly extracted sampling points from the $p(\mathbf{x})$. Additionally, it has been demonstrated that the summation in equation (2.4) has its own normal distribution function; thus, using the central limit theorem, one can estimate the

mean and variance of the $\mathbb{E}_p[f(x)]$ [89, 93, 94]. However, using an arbitrary $p(\mathbf{x})$ to extract the x_1, we may sample regions from the phase space which are less relevant to $f(\mathbf{x})$ (less "important"). By sampling these regions more frequently, the variance is increased, reducing the accuracy of $\mathbb{E}_p[f(\mathbf{x})]$. This is illustrated in figure 2.1 a., where there is a small overlap between $f(\mathbf{x})$ and $p(\mathbf{x})$; thus, having more dense sampling points in less relevant regions, represented by the black lines along the x axis.

The more "important" sampling region is the area under the $f(\mathbf{x})$, which is sampled more often in regions where the $p(\mathbf{x})$ overlaps with $f(\mathbf{x})$. This "important" area can be sampled more frequently by using another probability distribution function, $q(\mathbf{x})$, to draw the sampling points, which offsets the sampling towards regions of higher relevance to $f(\mathbf{x})$. This procedure is called importance sampling and can reduce the variance of $\mathbb{E}_p[f(\mathbf{x})]$ and is demonstrated in figure 2.1 b. Additionally, as discussed in 2.2.1, we use importance sampling Monte Carlo to sample regions relevant to a given temperature along the phase space without apriori knowledge of their location.

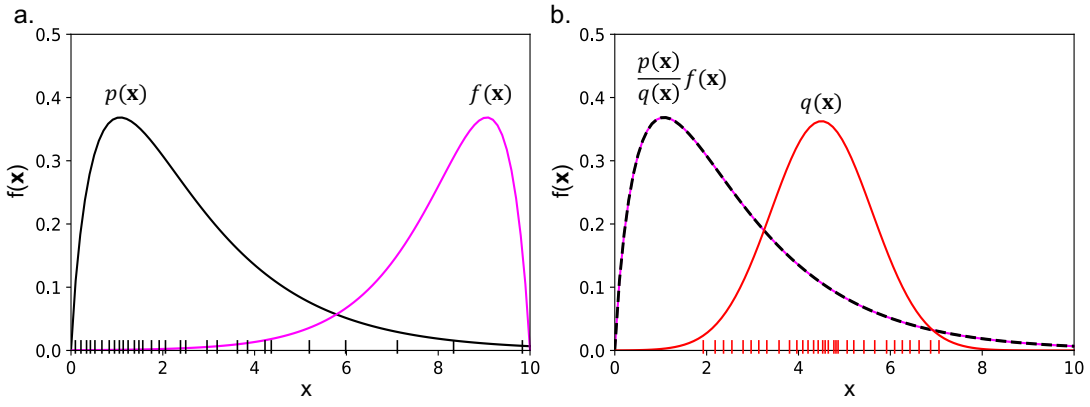

Figure 2.1: Importance sampling procedure. a, Shows the small overlap between the $f(\mathbf{x})$ and $p(\mathbf{x})$, resulting in high variance of the estimated value of $f(\mathbf{x})$ in simple sampling Monte Carlo. b, illustrates how another function $q(\mathbf{x})$ can be used in importance sampling Monte Carlo which reduces the variance of the estimated value of $f(\mathbf{x})$. Along the x-axis, the drawn sampling values x_1 from $p(\mathbf{x})$ and $q(\mathbf{x})$ are shown in a. and b. respectively.

To incorporate the importantance sampling, we need to select the probability distribution density to be $q(\mathbf{x}) > 0$ wherever $p(\mathbf{x})f(\mathbf{x}) \neq 0$ along the subset of drawn sampling points $\{x\}$. Importance sampling is realised in Monte Carlo techniques by modifying equations (2.3) and (2.4) to [93, 94]

$$\mathbb{E}_p\left[f(\mathbf{x})\right] = \mathbb{E}_q\left[\frac{p(\mathbf{x})}{q(\mathbf{x})}f(\mathbf{x})\right] = \int q(\mathbf{x})\left[\frac{p(\mathbf{x})}{q(\mathbf{x})}f(\mathbf{x})\right]\mathrm{d}x \approx \frac{1}{\mathrm{N}}\sum_{\mathrm{l}=1}^{\mathrm{N}} f(x_{\mathrm{l}})\frac{p(x_{\mathrm{l}})}{q(x_{\mathrm{l}})} \qquad x_{\mathrm{l}} \sim q(\mathbf{x}) \tag{2.5}$$

where points x_{l} are drawn from the $q(\mathbf{x})$ in contrast with equation 2.4 where x_{l} are drawn from $p(\mathbf{x})$.Then the average estimate of the expectation value $\mathbb{E}_p\left[f(\mathbf{x})\right] = \mathbb{E}_q\left[\frac{p(\mathbf{x})}{q(\mathbf{x})}f(\mathbf{x})\right]$ where $\mathbb{E}_q$ is the expectation value with the $q(\mathbf{x})$ which can also be estimated as an average as shown in equation 2.5.

Ultimately, the proper choice of $q(\mathbf{x})$ will reduce the variance [89, 93, 94]. Unfortunately, identifying the correct choice of $q(\mathbf{x})$ is not trivial. Moreover, both the simple and the importance sampling Monte Carlo techniques are valid under the assumption that the algorithm used is ergodic, meaning that all points within the phase space will be sampled for an infinite number of generated drawn points [93, 94].

2.2.1 Estimating Thermal Averages with Monte Carlo

In statistical physics, thermal averages of an observable $A(\mathbf{x})$ in the canonical ensemble are estimated as [90]

$$\langle A(\mathbf{x})\rangle_T = \frac{1}{\mathrm{Z}}\int \mathrm{d}\vec{x}\exp\left[-\beta\mathcal{H}(\vec{x})\right]A(\vec{x}) \tag{2.6}$$

Where $\langle ...\rangle$ denotes the expectation value of $A(\mathbf{x})$, which can be any macroscopic observable, $\mathcal{H}(\mathbf{x})$ is a Hamiltonian which describes the energy of any configuration of $\vec{x} = \{x\}$ and $\beta = 1/k_B T$ is the Boltzmann's factor where $k_B = 1.3806503 \times 10^{-23}$ J/K is the Boltzmann's constant and T is the temperature in Kelvins, and Z is the partition function defined as [89, 90]

$$\mathrm{Z} = \int \mathrm{d}\vec{x}\exp\left[-\beta\mathcal{H}(\vec{x})\right] \tag{2.7}$$

In equations 2.6 and 2.7, the normalised Boltzmann factor is the probability density function $p(\mathbf{x})$, which can be written as [90]

$$p\left(\mathbf{x}\right) = \frac{1}{\mathrm{Z}}\exp\left[-\mathcal{H}(\vec{x})\beta\right] \tag{2.8}$$

$p(\mathbf{x})$ incorporates the temperature by statistically weighting the configurations of the given phase space relative to the system's thermal equilibrium, often referred to as Boltzmann sampling. However, integrating all the possible configurations, as shown in 2.6, in a system with high dimensional phase space is analytically a tedious and computationally demanding task, which is mostly not possible to solve analytically. Hence the thermodynamic averages are estimated using the Monte Carlo techniques, which can calculate ensemble mean values by approximating equation 2.6 by summations. Adapting equation 2.6 to equation 2.5 we can approximate $A(\mathbf{x})$ as [90]

$$\left\langle A(\vec{x})\right\rangle_{\mathrm{T}} = \frac{\sum\limits_{\mathrm{l}=1}^{\mathrm{N}} \exp\left[-\mathcal{H}(\vec{x})\beta\right] A(\vec{x})/q(\vec{x})}{\sum\limits_{\mathrm{l}=1}^{\mathrm{N}} \exp\left[-\mathcal{H}(\vec{x})\beta\right]/q(\vec{x})} \tag{2.9}$$

However, we need to sample the phase space region relevant to a given temperature. Hence, the importance sampling procedure needs to be realised, where $q(\vec{x})$ needs to be selected to allow sampling of the "important" regions for a given temperature. In 1953 Metropolis et al. showed that by not drawing independent x_{l} but selecting x_{l} using a Markov Process with the appropriate transition probability $\mathrm{W}(x_{\mathrm{l}} \rightarrow x_{\mathrm{l}+1})$, $q(\vec{x})$ will lead an equilibrium distribution [95]

$$q_{eq}(x_l) = \frac{1}{\mathrm{Z}}\exp\left(-\mathcal{H}(x_{\mathrm{l}})\beta\right) \tag{2.10}$$

Here a Markov Process or Markov Chain is the process where the selection of $x_{\mathrm{l}+1}$ is not random. Rather, it only depends on the current configuration's transition probability, W, x_{l}.

The equilibrium distribution (2.10) thus can sample the phase space relevant to the temperature. Additionally using (2.10), the observable $A(\mathbf{x})$ (2.9) is reduced to an arithmetic average

$$A(\mathbf{x}) = \frac{1}{\mathrm{N}}\sum_{\mathrm{l}=1}^{\mathrm{N}} A(\mathbf{x}_{\mathrm{l}}) \tag{2.11}$$

More importantly, they demonstrated that the only condition required to realise importance sampling, which results in the equilibrium distribution (2.10), is to impose the principle of detailed balance (2.12), which states that the transition probability between two consecutive configurations must be symmetric [60, 89]

$$q_{\mathrm{eq}}(\mathbf{x}_{\mathrm{l}})\mathrm{W}(\mathbf{x}_{\mathrm{l}} \rightarrow \mathbf{x}_{\mathrm{l}+1}) = q_{\mathrm{eq}}(\mathbf{x}_{\mathrm{l}}+1)\mathrm{W}(\mathbf{x}_{\mathrm{l}+1} \rightarrow \mathbf{x}_{\mathrm{l}}) \tag{2.12}$$

Additionally, equation 2.12 implies that the W ratio only depends on the energy difference

$$\frac{\mathrm{W}(\mathbf{x}_{\mathrm{l}} \rightarrow \mathbf{x}_{\mathrm{l}+1})}{\mathrm{W}(\mathbf{x}_{\mathrm{l}+1} \rightarrow \mathbf{x}_{\mathrm{l}})} = \exp\left(-\Delta\mathcal{H}\beta\right) \tag{2.13}$$

where $\Delta\mathcal{H} = \mathcal{H}(\mathbf{x}_{\mathrm{l}}) - \mathcal{H}(\mathbf{x}_{\mathrm{l}+1})$ is the energy difference

There are multiple proven transition probabilities, W, used, which satisfy (2.12), which are used for different purposes and models. Here we use the following transition probability [90]

$$\mathrm{W}(\mathbf{x}_{\mathrm{l}} \rightarrow \mathbf{x}_{\mathrm{l}+1}) = \begin{cases} \frac{1}{\tau_{\mathrm{s}}}\exp(-\Delta\mathcal{H}\beta), & \text{if } \Delta\mathcal{H} > 0, \\ \frac{1}{\tau_{\mathrm{s}}}, & \text{otherwise.} \end{cases} \tag{2.14}$$

Where τ_{s} is an arbitrary factor that can be interpreted as "Monte Carlo Time" or "Monte Carlo Step", as it will be shown in section 2.2.2. Equation 2.14 shows that a transition move will be accepted if the energy of the new configuration $x_{\mathrm{l}+1}$ is lower than the current x_{l}. For a magnetic system, this energy is given by the Hamiltonian with units of Joules. If $\Delta\mathcal{H} < 0$, the acceptance probability will be proportional to $\exp(-\Delta\mathcal{H}/k_{\mathrm{B}}\mathrm{T})$. This transition probability is referred to as the Metropolis function, which is formally written as [89–91]

$$\mathrm{W}\left(\mathbf{x}_{\mathrm{l}+1}|\mathbf{x}_{\mathrm{l}}\right) = \min\left[1, \exp\left(\frac{-\Delta\mathcal{H}}{k_{\mathrm{B}}\mathrm{T}}\right)\right] \tag{2.15}$$

The metropolis function is the basis of the Metropolis Monte Algorithm, which is introduced in section 2.2.2 and will be later used to show how metadynamics is adapted to this algorithm.

2.2.2 Metropolis Monte Carlo Algorithm

The previous subsection discussed the main principles of Monte Carlo and how they are used to sample regions of a phase space relevant to a given temperature. The atomistic modelling

algorithms incorporating the principles of importance sampling are used to equilibrate predefined lattices, which allows the calculation of thermodynamic equilibrium properties such as magnetisation and heat capacity for a finite temperature. The lattice is often initialised with a configuration that is not thermalised. By using the importance sampling Monte Carlo, the excess energy is removed from the lattice with small increments by proposing random individual trial spin directions $\mathbf{S}_{\mathrm{trial}}$ which are then accepted or rejected using the acceptance probability which results in the Boltzmann distribution; which is often called the dynamic interpretation of Monte Carlo. As discussed, this is achieved by using any transition probability W, which satisfies the principle of detailed balance shown in equation 2.13. Doing so estimates the average observables of interest after incrementing a few Monte Carlo steps (MCS). A MCS is defined as the consecutive trial spins proposed equal to the number of lattice points.

The Metropolis Monte Carlo (MMC) algorithm is an importance sampling Monte Carlo technique that uses the Metropolis function W introduced in equation 2.15 to satisfy the principle of detailed balance. The algorithm proposes a random trial microstate configuration which is then accepted or rejected based on thermodynamic considerations that minimise the system's energy for the given temperature. In magnetism, the microstates are the spin vector directions $\mathbf{S}$. In other words, MMC proposes random states on a system which are accepted or rejected based on the acceptance criteria set by equation 2.15, which will force the system to be in regions of high probabilities for the given temperature along the space of the microstates. Thus sampling only the regions relevant to the given temperature. This allows the evaluation of any thermodynamic equilibrium properties of a magnetic system at finite temperatures.

In practice, the MMC is implemented with the following procedure, as also shown in figure 2.2: First, a predefined lattice space is initiated. Each lattice point represents a local magnetic dipole moment as vector $\mathbf{S}$, which can have any direction on the unit sphere. Then:

1. A random classical spin at point i from the lattice, $\mathbf{S}_{\mathrm{i}}$, is selected with energy, E_1, calculated from the Hamiltonian of the system.

2. A random magnetic moment direction is proposed for the spin in site i, $\mathbf{S}_{\mathrm{trial}}$, with energy E_2

3. If the energy difference between E_1 and E_2, $\Delta\mathrm{E} \leq 0$ or $\exp\left[-\Delta\mathrm{E}/\,k_{\mathrm{B}}T\right] > \chi$ where χ is a random number inside the interval $[0, 1]$ then, $\mathbf{S}_{\mathrm{trial}}$ is accepted

4. otherwise, $\mathbf{S}_{\mathrm{i}}$ is kept

5. Steps 1-3 are repeated n-times where n = lattice points (Monte Carlo Step)

6. After sufficient Monte Carlo Steps (MCS), the lattice is thermalised, and the simulation is stopped. The number of MCS required to thermalise the lattice depends on the size of the lattice. Once the lattice is thermalised, the value of the estimated thermodynamic averages fluctuates around a value; which size of fluctuations depends on the lattice size and temperature.

At the end of the simulation, the data acquired are analysed. The thermodynamic averages of interest, such as the magnetisation, heat capacity and susceptibility, can then be calculated from the final thermalised spin-lattice.

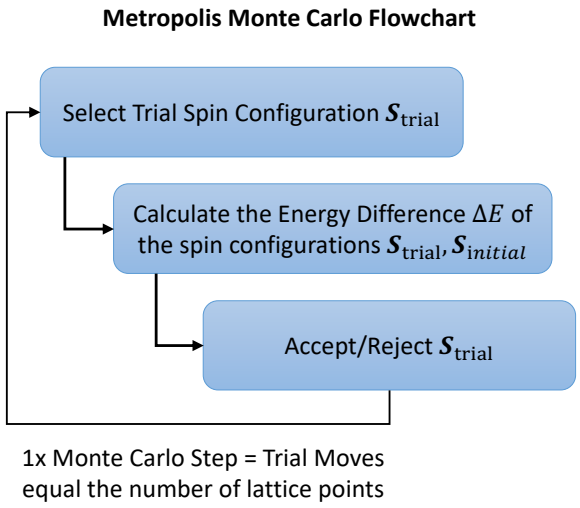

Figure 2.2: Metropolis Monte Carlo flowchart on a predefined atomic lattice where each lattice point is a local magnetic dipole moment **S**.

2.3 Metadynamics

As explained, the Metropolis Monte Carlo algorithm is an importance sampling technique that samples only a region of space relevant to the simulation's temperature. This project aims to reconstruct free energy landscapes (FEL) associated with single or multiple differentiable functions of the spin degrees of freedom, referred to as collective variables (CVs) or atomic coordinates and degrees of freedom. This is achieved by pushing these degrees of freedom out of their thermodynamic equilibrium to explore their whole landscape, thus sampling the free energy landscape associated with them. Examples of differentiable functions of the atomic coordinates in magnetism are the magnetisation and helicity of the spins. By selecting appropriate CVs that describe the transitions of interest, the skyrmion metastable energy can be estimated and studied at finite temperatures, which is a crucial parameter of the stability of the skyrmions; thus, an understanding of the thermal effects on skyrmion stability which is crucial for our understanding of skyrmions and the design of future skyrmionic devices as it was discussed in section 1.9. Multiple techniques are currently being explored to estimate the skyrmion metastable energies in atomistic and micromagnetism formalisms [2, 3, 54]. Namely, the geodesic nudged elastic band method (GNEBM) and variations of it can be applied in micromagnetic and atomistic simulation. However, GNEBM, either on micromagnetic or atomistic formalism, can not account for thermal effects, use abstract coordinates and cannot combine different CVs, as discussed in the introduction.

This project has successfully used metadynamics with the MMC algorithm to extract the skyrmion metastable energy in finite temperatures. In short, metadynamics is an enhanced sampling technique that accelerates the exploration of the atomic coordinates selected. However, metadynamics is not widely used in magnetism, and before this project, it had never been used to study topological spin textures in magnetism. Nevertheless, metadynamics has recently been reported in magnetism to study the nucleation of vortices in micromagnetism and the temperature dependence of the magnetocrystaline anisotropy and spin reorientations in thin films within the atomistic modelling formalism [87, 88]. A major difference with this project is that these metadynamic studies used trivial CVs since the shape and energy barrier energies of their

associated FELs were expected and were non-topological, which, as is discussed in the results section, hides a lot of difficulties that needed to be overcome.

There are a plethora of ways in which metadynamics accelerate the exploration of the CVs selected, each having benefits and drawbacks for studying specific systems. However, the basic ideas of metadynamics remain the same; creating a potential landscape that fills the energy minima of any functions of the atomic coordinates, which is used to bias them out of their thermodynamic equilibrium to explore their landscape. In this project, we used plain and tempered metadynamics. Hence these metadynamic variations will be discussed in this chapter. One of the difficulties of metadynamics is the calculation of the CVs. Since many CVs are used in this project, the method of calculating each of them will be introduced when they are used in the following chapters.

2.3.1 Metadynamics Collective Variables

In metadynamics terminology, the differentiable functions

$$Y_{\mathrm{a}} = (y_1(x), ..., y_{\mathrm{a}}(x)) \tag{2.16}$$

of the set of microscopic coordinates $\{x\}$ which describe the system of interest are referred to as Collective Variables (CVs) where a is the number of the selected CVs. If more than a single CV is used, the explored energy landscape space will be multidimensional. The CVs can be seen as generalised coordinates where their space is defined by the configurational space $y(x)$ and the value of a CV as y. In a magnetic system, the set of microscopic coordinates describing the system are

$$x = \{\mathbf{S}_1, \mathbf{S}_2, ..., \mathbf{S}_{\mathrm{n}}\} \tag{2.17}$$

where $\mathbf{S}_{\mathrm{n}}$ are the localised magnetic moments.

Metadynamics is used to reconstruct the free-energy landscapes associated with the set of CVs selected. This allows us to explore and quantify the transition pathways and energy barriers between states revealed by sampling the CVs configurational space. However, the choice of the CV needs to be carefully considered since the accuracy and reliability of metadynamics

depend on the choice of the CV. Much previous work has been conducted to identify suitable CVs for specific applications. In 2008, Laio and Gervasio summarised three properties that constitute a set of suitable CVs. These are the following properties that CV need to satisfy [96]:

1. Clearly distinguish the initial, final and all intermediate states
2. Describes the events relevant to the process of interest
3. Their number should be small

The first property ensures that the CVs selected are continuous variables. This ensures that all the transition features between the initial and the final states can be sampled smoothly without hiding any information.

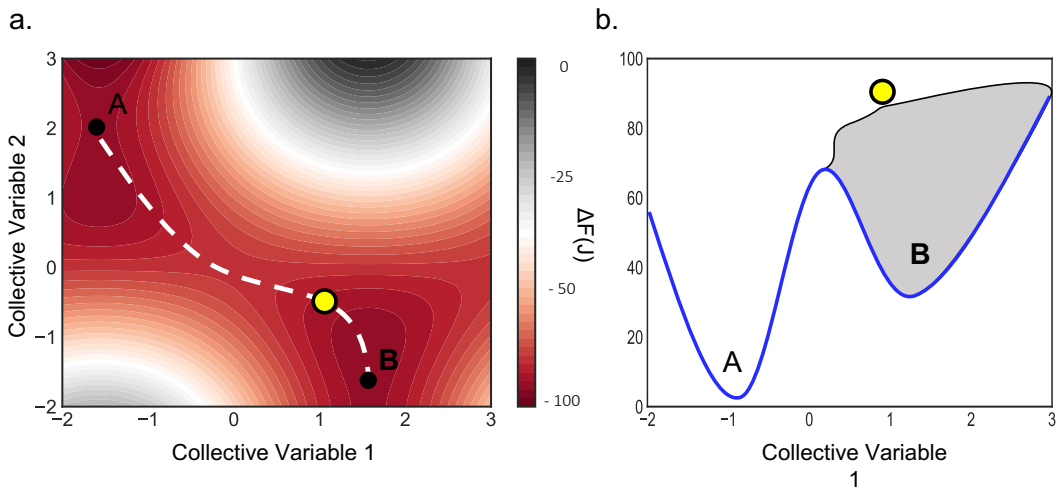

Figure 2.3: Free Energy Landscapes reconstructed by metadynamics for a transition from state B to A, whose process is described by two CVs. The minimum energy path is shown in a. by the white dotted lines, and the yellow circle indicates the value of the CVs. In b., the system has the same FEL as in a. and is reconstructed using a single CV, illustrating the overfilled potential shown as the grey area.

The second property is important to be satisfied to avoid overfilling the potential landscape from which the FEL is reconstructed as discussed in section 2.3.2, metadynamics builds a potential landscape to fill the CVs energy minima and push each CV out of its thermodynamic equilibrium, which is then used to reconstruct the associated free energy landscape. The transition between states occurs when each minimum is filled. If one or more CVs required to describe the transition process between states are not included, the resulting potential will be overfilled; the potential build will include the energy of the minimum of the neglected CV. Hence estimating the FEL inaccurately. Figure 2.3 illustrates this, where A and B are two minima. Metadynamics is used to estimate the energy required to transition from state B to A. The yellow circle indicates the value of the CVs y at a given time during the metadynamics simulation. Figure 2.3 a. shows that two CVs describe the transition process from B to A. Using only a single CV results in overfilled potential shown as the grey area in figure 2.3 b, which then results in inaccurate reconstruction of the FEL shown by the blue line.

On the other hand, the number of CVs describing a process should be as small as possible to understand the relevant pathways. As more CVs are used to describe a transition process, higher dimensional FELs are reconstructed, which are hard to analyse. Additionally, the higher the dimensional space of the CVs, the more computationally expensive the metadynamics simulations become since the phase space becomes one order larger with every additional CV added.

2.3.2 Metadynamics Integration to Metropolis Monte Carlo

In metadynamics, a history-dependant bias potential, V_{bias}, is build during the simulation to bias the CVs to escape their local minima to explore their whole configurational spaces. V_{bias} is build by depositing and accumulating Gaussians centred around the CV values calculated from the system's configuration during the simulation [96]. Other functions, such as triangular functions, can be used to fill the local minima [97]. However, Gaussians fill the minima more uniformly, minimising the possibility of creating large local minima between two consecutive depositions.

Following the metropolis algorithm described in section 2.2.2, metadynamics can be im-

plemented by altering the acceptance probability of every Monte Carlo trial move by including the bias potential difference, ΔV_{bias}, into the acceptance criteria [86, 96, 98]. During the metadynamics simulation, V_{bias} is stored and updated in a histogram spanning along the CVs configurational space $\mathrm{N}(y(x), t)$, where t is the time of the simulation or MCS and $y(x)$ is the CV value resulted from the system's configuration from $\{x\}$. For a trial move $\mathbf{S}_{\text{trial}}$, the system's configuration from which the value of the CV is calculated will be different from the system configuration with $\mathbf{S}_{\text{i}}$, resulting in different CV values. This, in turn, points to different values of potential stored in $\mathrm{N}(y(x), t)$. In this thesis, the value of the potential at an arbitrary point V(CVs) is found using linear or bilinear interpolation, depending on the number of CVs used. This is because, technically, in the code developed $\mathrm{N}(y(x), t)$ is a discretised n-dimensional array with equal-sized bins; thus, linear or bilinear interpolation is used to find the potential values along the $\mathrm{N}(y(x), t)$. Thus ΔV_{bias} for $\mathbf{S}_{\text{trial}}$ and $\mathbf{S}_{\text{i}}$ is calculated from $\mathrm{N}(y(x), t)$ build during the simulation. To summarise, the acceptance probability for the trial spin direction, $\mathbf{S}_{\text{trial}}$ in metadynamics depends on both ΔE and ΔV_{bias} of $\mathbf{S}_{\text{trial}}$ and $\mathbf{S}_{\text{i}}$

$$P(x_{\text{initial}} \rightarrow x_{\text{trial}}, t) \equiv \min[1, \exp(-\beta(\Delta E + \Delta V_{\text{bias}}))] \tag{2.18}$$

Hence V_{bias} introduces an energy penalty to discourage the system from sampling the same regions along the configurational space of the CVs selected. Similarly, V_{bias} also bias the system to adapt a set of configurations $\{x\}$ which result in CVs values where the potential in $\mathrm{N}(y(x), t)$ is lower. Effectively this pushes the system out of the thermodynamics equilibrium from the MMC algorithm, which allows the sampling of the CVs configurational space. The flowchart of the implementation of metadynamics in the MMC algorithm is also illustrated in figure 2.4.

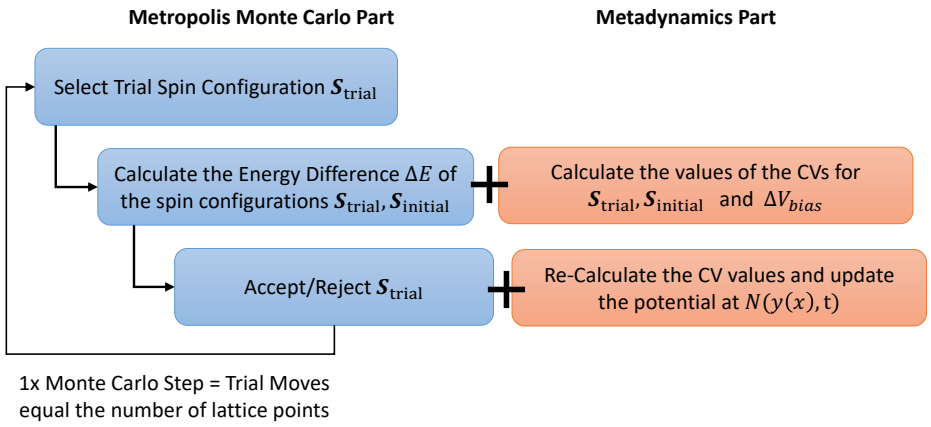

Figure 2.4: Flowchart with the implementation of the metadynamics in the MMC algorithm. For every trial move, the difference of the bias is included in the acceptance/rejecting criteria of the $\mathbf{S}_{\mathrm{trial}}$, and the potential is updated in each trial move step.

2.3.3 Direct / Plain Metadynamics

In direct or plain metadynamics, the FEL of the set of CVs used is estimated by depositing Gaussian in $N(y(x), t)$ during the simulation according to [84, 96]

$$V_{\mathrm{bias}}(y(x), t) = w \sum_{\substack{t'=\tau, 2\tau, \ldots \\ t'<t}} \exp\left(-\sum_{\mathrm{a}=1}^{\mathrm{N_{cv}}} \frac{\left(s_{\mathrm{a}}(x,t) - s(x,t')\right)^2}{2\sigma_{\mathrm{a}}^2} \right) \tag{2.19}$$

where w, σ and τ are the Gaussian height, width in units of energy and the time interval at which Gaussians are deposited, which are pre-defined and centred at the CVs values at a time, t. The summation from a through the number of the CVs selected N_{cv}.

As introduced in section 2.3.2, the potential introduced will result in the progressive exploration of the CVs configurational space, $y(x)$ [85]. This is because the potential introduced to previously visited states along the $y(x)$ will make it thermodynamically un-favoured to revisit the same state. In metadynamics, the shape of the FEL $F(y)$ is not required to be known before the simulation. Usually, the systems of interest in this project have unknown FELs. Also, which spin textures can be stable in a system is often unknown, and metadynamics can find all the possible textures. Hence, here it is emphasised that this is one of the primary motivations

that metadynamics was used instead of widely used techniques such as the GNEBM, where the initial and final configurations and the FEL need to be known before the simulation.

At the start of the MMC metadynamics simulation, the system is in thermodynamic equilibrium for a given temperature, which minimises its internal energy as described in section 2.2.1. Effectively this is due to an energy minimum within $F(y)$ in which the physical system is trapped. The $V_{\text{bias}}(y(x), t)$ progressively fills the energy minimum in which the CVs are localised at $t = 0$. Once the first energy minimum is filled, the CVs will move in different regions along its space, with lower potential. If there are more energy basins along the FEL, $F(y)$, the CV will move in every energy basin until the potential build fill all of them. During this process, the $F(y)$ is modified to $F'(y)$, which is the energy landscape felt by the system due to the potential build. Thus, the FEL experienced by the physical system is $F'(y)$. Eventually, the potential built by equation 2.19 and stored in $N(y(x), t)$ will flatten the $F'(y)$. When the FEL is flattened, the CVs will freely fluctuate along their configurational spaces. This means that in the long time limit, the FEL is roughly the negative of the potential built plus an arbitrary constant, C, previously shown [84–86, 98, 99]

$$V(y(x), t \to \infty) = -F(y) + C \tag{2.20}$$

However, when more complex CVs are used, the underlined $F(y)$ and the associated energy barriers can not be estimated before the simulation. This creates a major issue with direct metadynamics; the Gaussians will be deposited along the configurational space of the CV with a constant w and σ overfilling the potential landscape. When the energy deposited constantly increases unlimited, it can force the physical system into low probability state configuration or regions along its space. In the example shown in figure 3.1, if the V_{bias} energy exceeds exchange energy in all points along the configurational space of the CV, the system will behave as a paramagnet, which is a highly improbable state. It is a very low probability state since the system's temperature in the example is not higher than the Curie temperature. Additionally, the estimated FEL will fluctuate by a factor proportional to w since Gaussians with constant w are deposited throughout the simulations.

2.3.4 Well-Tempered Metadynamics

By solely employing plain metadynamics, there is a concern that the bias potential energy will exceed the metastable energy of the topological spin textures, thus destroying them before the CVs configurational space is sampled in studies where we want the skyrmion to move around the sample. Additionally, with plain metadynamics, the error increases by a factor of ω after the FEL is filled, which is usually hard to identify. An argument for the first concern described is that the rate of the energy deposited, which is defined as

$$\varepsilon = \frac{V_{\text{bias}}}{\tau} \tag{2.21}$$

with units of energy per MCS (time), can be used to ensure that the spin texture will move to regions with lower potential before it is destroyed. However, plain metadynamics can be used to identify the magnitude of the energy barriers along the $F(y)$ associated with the CVs; but eventually will exceed this energy barrier resulting in the limitations described here and in section 2.3.3. Therefore, we employ the well-tempered metadynamics algorithm proposed by Barducci, Alessandro et al. in 2008, which scales the initial Gaussian height w_0 during metadynamics for regions previously visited along the configurational space of the CVs according to [100]

$$w = w_0 \cdot \exp\left(\frac{N\left(y\left(x\right),t\right)}{\Delta T \cdot k_{\text{B}}}\right) \tag{2.22}$$

where w is the Gaussian deposited during the simulation, and ΔT is called the bias temperature, with the temperature dimensions, which is used to control the rate of the Gaussian height scaling. Substituting equation 2.22 to 2.19, V_{bias} becomes [99, 100]

$$V_{bias}(y(x),t) = w_0 \cdot \exp\left(\frac{N(y(x),t)}{\Delta T k_{\text{B}}}\right) \sum_{\substack{t'=\tau,2\tau,\ldots \\ t'<t}} \exp\left(-\sum_{\alpha=1}^{N_{cv}} \frac{\left(y_a(x,t) - y(x,t')\right)^2}{2\sigma_a^2}\right) \tag{2.23}$$

Thus in well-tempered metadynamics, the Gaussians deposited along the histogram $N(s(x),t)$ will scale down by $\frac{1}{N(s(x),t)}$ and not like $\frac{1}{t}$ as in many other enhanced sampling techniques. This is important because it scales the potential only for previously visited sites along the

configurational space of the CVs, allowing to fill any potential basins into which the CV move. Well-tempered metadynamics can be seen as sampling the CVs at higher temperatures $T+\Delta T$. Hence in the long time limit, the free energy is recovered by considering ΔT

$$F(y) = -\frac{\Delta T + T}{\Delta T} \cdot V(y(x), t) \tag{2.24}$$

In the long time limit $V_{bias}(y)$ built converges to $\frac{-\Delta T}{T+\Delta T}F(s)$. Additionally, the fluctuation in the estimate of the $F(y)$ is progressively damped since the Gaussian height is reduced. Eventually, $F'(y)$ converges to $F(y)$ because w height becomes negligible [85, 100].

The choice of ΔT is crucial since the larger the bias temperature, the faster the potential basins are filled. The simulation becomes computationally more efficient; fewer MCS are required to fill all the energy minima in $F(y)$. However, the slower the fluctuations of the estimated $F(y)$ are damped. Furthermore, ΔT can introduce maximum energy deposited along the configurational space of the CVs, ensuring that the system will not be biased to go into any unphysical configuration. In practice, plain metadynamics can approximate the energy barriers' magnitudes, thus selecting the ΔT accordingly. A better comprehension of the effect of ΔT is achieved by examining two extreme values of ΔT [85, 99]:

- For $\Delta T \to \infty$: Direct metadynamics is recovered since the exponential in equation 2.22 will be close to 1. Hence the Gaussians deposited will have constant height.
- Similarly for $\Delta T \to 0$, simple MMC metropolis is recovered. This is because every time a Gaussian will be deposited in $N(y(x), t)$, the scaling will minimise the Gaussian into 0; thus, effectively, there will be no external bias to push the CVs out of equilibrium and $F(s) = T \cdot k_B \ln(s(x))$.

CHAPTER 3

Metadynamics Analysis of Magnetic Anisotropy

Metadynamics can be more apparent by considering a simple case study relevant to a spin-lattice, as shown in figure 3.1. The physical system considered is a ferromagnetic system with out-of-plane magnetisation m_z, described with a Hamiltonian, including the Heisenberg exchange and magnetocrystaline anisotropy terms. Using metadynamics, the scaling of the effective anisotropy with temperature can be estimated using m_z as the CV. This is because the energy barrier for the magnetic spin crossing is set by K_{ani} for a given temperature. The CVs configurational space, $y(x)$, is in the range of $[-1, 1]$.

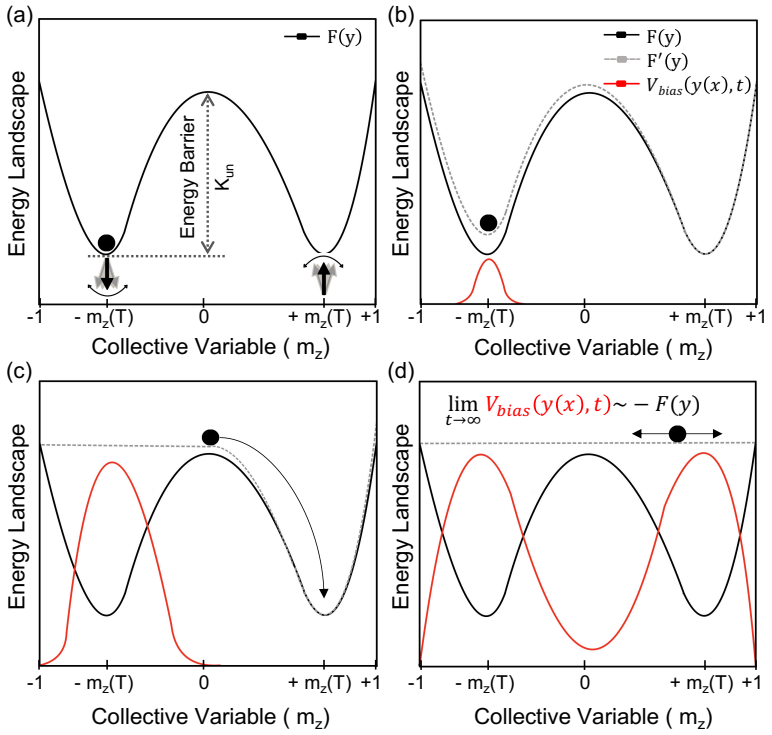

Figure 3.1: Metadynamics procedure considering a ferromagnetic thin film a.System at the equilibrium at $-m_z(T)$ with the underlying FEL $F(y)$ (black line). b, Gaussian deposited which modify the underlying FEL $F(y) \rightarrow F'(y)$ shown as the dashed grey line. c. The first energy basin filled results in the CV moving to the second energy minimum region. d. the CV fluctuates freely once all the energy minima are filled by the potential build, which in the long time limit represents the FEL as shown in the equation.

In figure 3.1a, the underlying FEL $F(y)$ that metadynamics is aimed to reconstruct is illus-

trated with the solid black line. For a given temperature, the magnetic system is at thermodynamic equilibrium magnetisation at $\pm m_z(T)$, and the CV (m_z) will fluctuate within the energy well due to the finite temperature. In the long-time limit, there is a small finite probability that an event will occur where the magnetisation will switch due to temperature fluctuations. The Néel Arrhenius equation gives the mean transition time τ_{N} of that event with the following expression

$$\tau_{\mathrm{N}} = f_0 \exp\left(\frac{\Delta E}{k_{\mathrm{B}} T}\right) \tag{3.1}$$

where f_0 is the attempt frequency and ΔE is the energy barrier in units of energy. However, the mean transition time can be thousands of years. These events are called rare events; the probability of sampling them is negligible. However, metadynamics accelerates the exploration of these events by biasing the CV. As shown in figure 3.1 b, metadynamics deposits a Gaussian centred at the CV value using equation 2.19. This modifies $F(y)$ to $F'(y)$, which makes it more favourable for the CV to explore other regions along y where the potential is lower. Eventually, the potential build will fill the first energy minima, and the CV will move into the second energy minimum, 3.1 c. Once all the energy basins are filled, the CV will fluctuate freely along its configurational space since the $F'(y)$ is flattened. From figure 3.1 d, it can be seen that, indeed, in the long time limit, the potential build is the inverse of the underlying FEL. However, when more complex CVs are used, the underlined $F(y)$ and the associated energy barriers can not be estimated before the simulation.

As described here and in the methodology section, metadynamics biases the CVs to explore the whole configurational space, which biases the physical system to explore its space. Thus, metadynamics will try to sample the boundaries of the physical space at $m(z) = \pm 1$. For low temperatures where $m_z(T)$ is close to the boundaries of the configurational space, systematic errors are introduced. These systematic errors at the boundaries affect the accuracy of the estimated energy barriers and shape of the reconstructed FEL. These systematic errors are avoided using the mirrored boundary conditions discussed in 3.2. Furthermore, the study of the magnetic anisotropy scaling with temperature is also used as a model validation for the code developed against conceptual algorithm errors and bugs by validating the Callen-Callen theory, which shows how the magnetocrystaline anisotropy energy scales with temperature.

Here, metadynamics was applied on a bulk ferromagnetic system with the CV set as the out-of-plane magnetisation, m_z. Thus the anisotropy scaling with temperature can be estimated to validate the Callen-Callen theory.

In this chapter, the plain, tempered metadynamics and mirrored boundaries applied will be discussed before presenting the final results of the anisotropy scaling.

3.1 Plain/Direct Metadynamics Test

A simple cubic $20 \times 20 \times 20$ ferromagnetic bulk system at a finite temperature of $\mathrm{T} = 20\mathrm{K}$ was considered for testing the plain metadynamics code developed, and the ability of metadynamics to reconstruct the expected FEL as illustrated on figure 3.1. This system's thermodynamic equilibrium normalised magnetisation is $m_{\mathrm{z}}(\mathrm{T}) = 0.70$. The CV selected was the out-of-plane magnetisation m_{z} with a physical space $m(z) \in [-1, 1]$. As described, we know that the expected free energy landscape will have two minima at $\pm m_{\mathrm{z}}(\mathrm{T})$; thus, by monitoring the m_{z} evolution during the metadynamics simulation, the algorithm developed is tested. It is expected the metadynamics will fill the two minima, and once all minima are filled, the CV will freely fluctuate along its configurational space. The test results are presented in figure 3.2.

The simulation was initiated with uniform magnetic spins along the positive z-direction, figure 3.2 A.i. At A.ii, the system reached its thermodynamic equilibrium $m_{\mathrm{z}}(\mathrm{T}) = 0.70$ for the given temperature.

Region A is thus the first energy basin that CV is located. When the potential built is comparable with the energy basin, the CV diffuses into the second energy minimum region at $y(x) = -m_{\mathrm{z}}(\mathrm{T})$. However, once the potential build fills the second energy minimum at $-m_{\mathrm{z}}(\mathrm{T})$, the CV fluctuates in $y(x)$ freely, as shown in figure 3.2 C.

In region B, the CV fluctuations are more significant compared to region A. Region A seems to be more smooth since we initiate the simulation with uniform magnetic spin configurations without relaxing our system. Hence, until the magnetisation reaches the $m_{\mathrm{z}}(\mathrm{T})$, the Gaussians deposited at the first 300 Monte Carlo steps have filled a part of the energy minimum at $+m_{\mathrm{z}}(\mathrm{T})$. Thus, when the CV reaches the bottom of the energy well, the potential

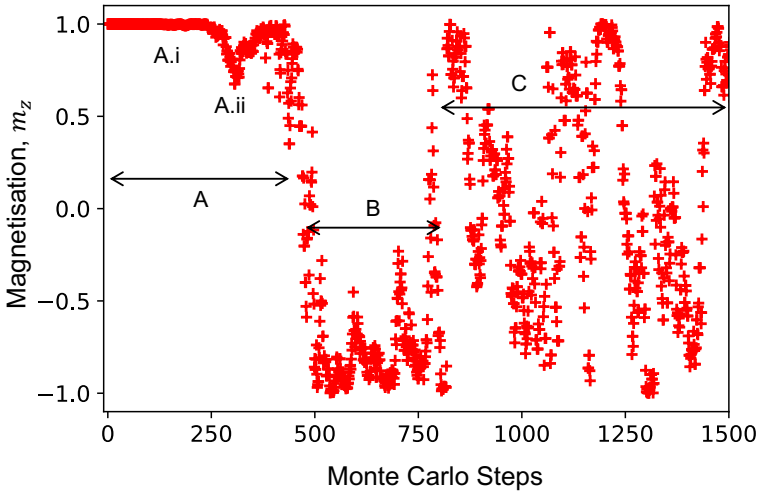

Figure 3.2: Collective Variable evolution along its configurational space $y(x)$. Region A.i shows the initial state of the simulation. A.ii, the system is relaxed in its thermodynamic equilibrium. The CV reaches region B when the potential built at region A exceeds the energy barrier set by the magnetocrystalline anisotropy, which results in the magnetic spin switch. Region C shows the CV fluctuating freely along $y(x)$.

added centred around the CV fills only the other half. It is worth noting that in the later sections, the lattice is first thermalised, and metadynamics is afterwards applied, which increases the accuracy of the estimated free energy landscape.

A range of Gaussian amplitudes were considered, which affect the speed and accuracy of the final FEL. For this test, we only test the evolution of the CV. This is because, as expected, plain metadynamics will overfill the potential landscape once all minima are filled since it will continue depositing Gaussians until the simulation is stopped. This is shown in figure 3.3, where the shape of the resulting FEL is asymmetric and the energy barrier is two orders larger due to overfilled potential landscape. However, it is also essential to test the plain metadynamics since it is the base of our code and is later used to select the appropriate tempered metadynamics parameters. Thus, a relatively large Gaussian amplitude of $w = 1 \times 10^{-24}$ J compared to the magnetocrystalline anisotropy of the system $K_{\mathrm{u}} = 5 \times 10^{-23}$ J with a depos-

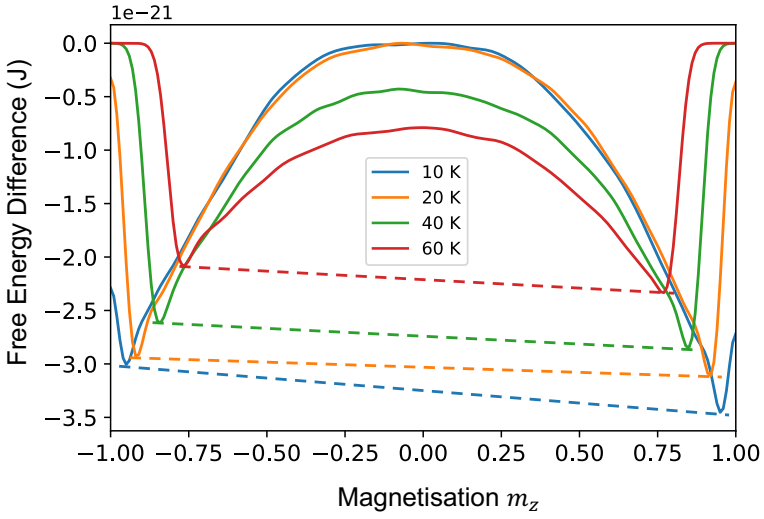

Figure 3.3: Plain metadynamics reconstructed FEL for a range of temperatures. Due to the overfilled potential, the depth of the energy minima are significantly different, the shape of the FEL is unsymmetric, and the expected energy barrier order is off by two orders.

ition stride of $\omega = 2MCS$. These values selected since the evolution of the CV were tested regardless of the accuracy of the resulting FEL but purely considering the simulation speed.

To conclude, the study of the CV evolution ensured that the implementation of direct metadynamics was error-free since the simulation could explore and sample all the physical regions of the CV space as expected, and the final shape of the FEL was as expected.

3.2 Mirrored Boundary Conditions

Metadynamics biases the CVs to explore their configurational space $y(x)$. Systematic errors are introduced near the boundaries for temperatures where the thermodynamic equilibrium magnetisation difference from the boundary values is smaller than the Gaussian width, $|m_{\mathrm{z}}(\mathrm{T})| \gtrapprox 1 - \sigma$. For higher temperatures where the $|m_{\mathrm{z}}(\mathrm{T})|$ is lower, it is unprobable for the system to reach areas close to the boundaries since it has to work against the entropy introduced by the temperature. The systematic errors are due to the finite size of the Gaussians, which can result in the CV getting trapped near the boundaries. Thus metadynamics can not converge to the $F(s)$ since the system is oversampled in regions near the boundaries, which affects the accuracy of metadynamics. This limitation was overcome by employing mirrored boundaries similar to the publication of Crespo et al. in 2010 [101]. Effectively the mirrored boundaries build a repulsive potential in the boundaries allowing the CV to explore the physical space $y(x)$ without getting trapped in the boundaries, which can be considered unphysical in regions where $|m_{\mathrm{z}}| > |m_{\mathrm{z}}(\mathrm{T})|$ for finite temperatures.

The mirrored boundaries are implemented as an extended discrete landscape in m_{z}, covering the range of -2.0 to 2.0 as illustrated in figure 3.4. Only the range -1.0 to 1.0 is physically meaningful. When a Gaussian is deposited centred around the value of the CV within the physical space, a second Gaussian is mirrored across the boundary with a centre of $2L_0 - y$ for negative CV values and $2L_1 - y$ where L_0 and L_1 are the maximum and minimum region of the CV configurational space. This avoids the potential and the spin system getting stuck near the edges. This is because there is a potential build at $|m_{\mathrm{z}}(\mathrm{T})|$ from the overlapped Gaussians near the boundary, as shown by the solid blue lines in figure 3.4. This flattens out the free energy landscape in these regions and prevents the CV values and spin system from getting trapped in that region. If no mirrored boundaries are applied, the potential build near the edges will be overfilled, as shown by the dashed red lines within the physical space region in figure 3.4.

In figure 3.4, the effect of the mirrored boundaries is shown, which helps to flatten the region where $|m_z| > |m_{\mathrm{z}}(\mathrm{T})|$ by sampling the region with the overlapping Gaussians used build the potential.

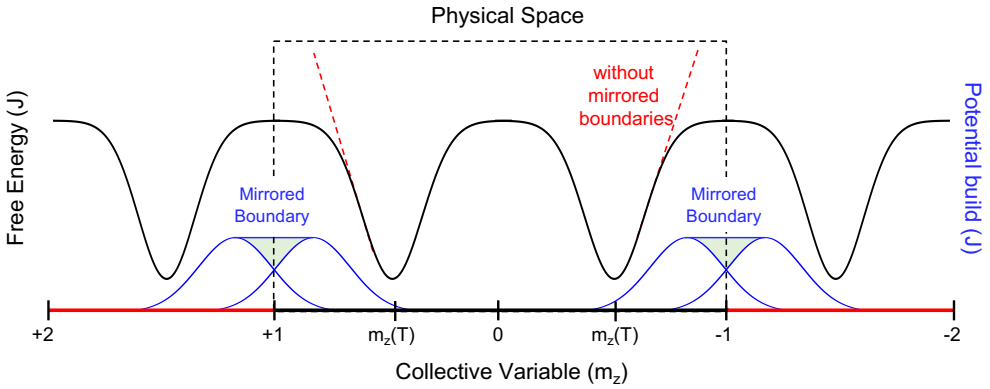

Figure 3.4: Illustration of the effect of the mirror boundaries. The black plot represents the FEL, and the blue line is the potential built near the boundary. The expected FEL near the boundary without the mirrored boundaries is shown as red dashed lines within the physical space denoted with the black dashed lines.

3.3 Well-Tempered Metadynamics Test

Having validated the plain metadynamics algorithm, the Gaussian amplitude tempering was tested. A simple cubic 20x20x20 thin film was considered for testing the well-tempered metadynamics functions. The initial Gaussian height set $w_0 = 1 \times 10^{-25}$ J which is two orders smaller than the $K_u = 1 \times 10^{-23}$ J. The small initial Gaussian height ensures that the potential landscape will not get overfilled. Additionally, a smaller initial w_0 ensures that the initial fluctuations of the estimated energy barrier will fluctuate less around the energy barrier value. However, a small initial Gaussian amplitude significantly increases the time required to fill the energy minima.

Figure 3.5 shows the Gaussian scaling. Regions A and B show that the CV fluctuations inside the minima are approximate $\approx 0.3w_0 - 0.5w_0$, which is a result of the width of the well; thus, the Gaussian width is selected as an order smaller than this fluctuation $\sigma = 0.03$. A range of bias temperatures, ΔT, were used as shown on 3.1. The values of the ΔT were in the order of one larger of the minimum regions and similar to the exchange of the system since the potential needs to exceed to exchange to flip the spins. Additionally, it is shown

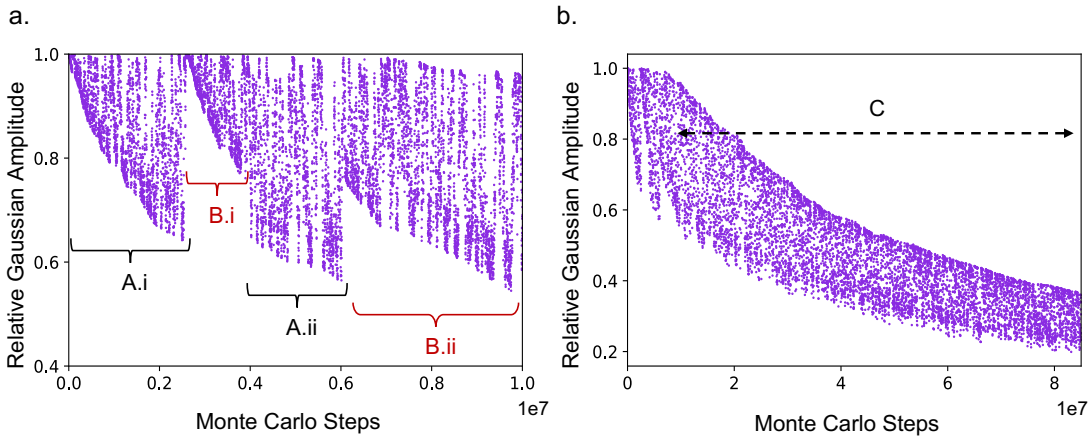

Figure 3.5: Gaussian amplitude evolution during the tempered metadynamics simulation. The initial Gaussian height was set $w_0 = 1 \times 10^{24}$ J. Regions A and B show the regions where the CV was fluctuating inside the two energy minima. C represents the points in the simulation where the CV was freely fluctuating in the configurational space, $y(x)$.

that a ΔT with similar energy of the exchange of the system will minimise the stationary fluctuations of the estimated $F(y)$ with fewer Monte Carlo steps. Finally, mirrored boundaries are applied to eliminate the boundary errors described in section 3.2. Having selected the tempered metadynamics parameters, we test the Gaussian amplitude scaling as shown in figure 3.5.

The scaling trend of w_0 can be seen along the dense area in figure 3.5b. This is because the scaling of w_0 occurs individually at every point along the histogram. The predefined histogram has 2000 points since the CV $y(x) \in [-1, 1]$, and the step size of the predefined histogram $\mathrm{N}(y(x), t)$ is set as 0.001.

Regions A, B and C of 3.5 represent the same regions as in figure 3.2. Figure 3.5 a. shows the first million MCS, which illustrates an important fact. The CV has a finite probability of crossing the energy barrier due to the onset fluctuations of the magnetisation due to the finite temperature effects before the energy minimum is fully filled with potential. This phenomenon is clearly shown in figure 3.5 A.i, where the first energy basin is partially filled before the

CV crosses the energy barrier, B.i. Thus the Gaussian height is recovered to the initial height w_0. After the second energy basin is partially filled, the CV transitions back to the first one, A.ii, before it crosses again to the second, B.ii. Once the $V(Y(x))$ has filled both energy minima partially filled, the CV crosses multiple times and samples the region between the two minima and fully fills both minima. Eventually, w is reduced along the histogram, and its effect becomes negligible, which ensures the potential landscape $V(Y(x))$ is not overfilled. If the metadynamic parameters have been selected correctly, the energy barrier estimation will converge to the solution with small onset fluctuations. It is also important the energy barrier is crossed many times to sample the FEL more accurately.

Following the Gaussian scaling tests, the convergence of the energy barrier with magnetic anisotropy constant K_{u} was examined. Figure 3.6 shows the results the same $20 \times 20 \times 20$ simple cubic ferromagnetic thin film with $K_{\mathrm{u}} = 1.4 \times 10^{-23}$J, $J_{\mathrm{ij}} = 2.2 \times 10^{-21}$J at 10K, with various bias temperatures ΔT. As shown in 3.6, three ΔT temperatures were examined and compared to the exchange energy of the system for the reasons explained. Following equation 2.24, we expect to converge to a reduced K_{u} based on the simulation temperature and the ΔT value used; since in well-tempered metadynamics, the system is sampled at a higher effective temperature due to the introduction of the bias temperature. The bias temperatures and their expected convergence points calculated are presented in table 3.1.

Numerical Details for ΔT	
ΔT (K)	Calculated Convergence Point (J)
$100 < E_{ex}/k_B$	1.26×10^{-23}
$164 = E_{ex}/k_B$	1.31×10^{-23}
$350 >> E_{ex}/k_B$	1.35×10^{-23}
$K_u = 1.4 \times 10^{-23}$J , $E_{ex} = 3.55 \times 10^{-21}$J , $T = 10$K	
1 Kelvin $\times\, k_B \cong 1.38 \times 10^{-23}$ J	

Table 3.1: Tempered metadynamics simulation parameters used to study the convergence of the calculated energy barriers with magnetic anisotropy, K_u for a range of bias temperatures ΔT (plotted in figure 3.6). The calculated convergence points are the scaled K_u using the bias factor for each ΔT as explained in section 2.3.4.

As seen in figure 3.6, the functions developed can accurately estimate the energy barriers associated with the selected CV. In addition, the effect of the ΔT upon the speed and accuracy of the simulation can be seen. For a $\Delta T < E_{ex}$, the estimation of the energy barrier converges to the scaled K_u value shown as the red dashed line on figure 3.6 with the most minor onset fluctuation at approximately 8×10^9 MC steps. By tunning the ΔT, the metadynamics solution will converge to the scaled K_u value. For higher values of ΔT, the energy barrier will converge faster but with larger fluctuations which will eventually be minimised. Similarly, for smaller values of ΔT metadynamics will converge to the scaled K_u slower (i.e. more MC steps), but the fluctuations will be lower since the Gaussian are scaled down faster.

In comparison, for $\Delta T = 164$K and $\Delta T = 350$K, the energy barrier converges to the scaled value of K_u approximately in 30×10^6 and 50×10^6 less MC steps with progressively more significant onset fluctuations. This is because as ΔT increases, the rate at which the Gaussian height is scaled down decreases.

An essential remark of ΔT in well-tempered metadynamics is that it can be used to predict the maximum potential energy deposited. This control of the maximum potential deposited is crucial for this project and any future continuation; it will allow sampling landscapes, including skyrmions, without exceeding the energy required to annihilate a skyrmion.

To conclude, the results presented in the figures 3.6 and 3.5 ensure that the code developed is accurate without any errors.

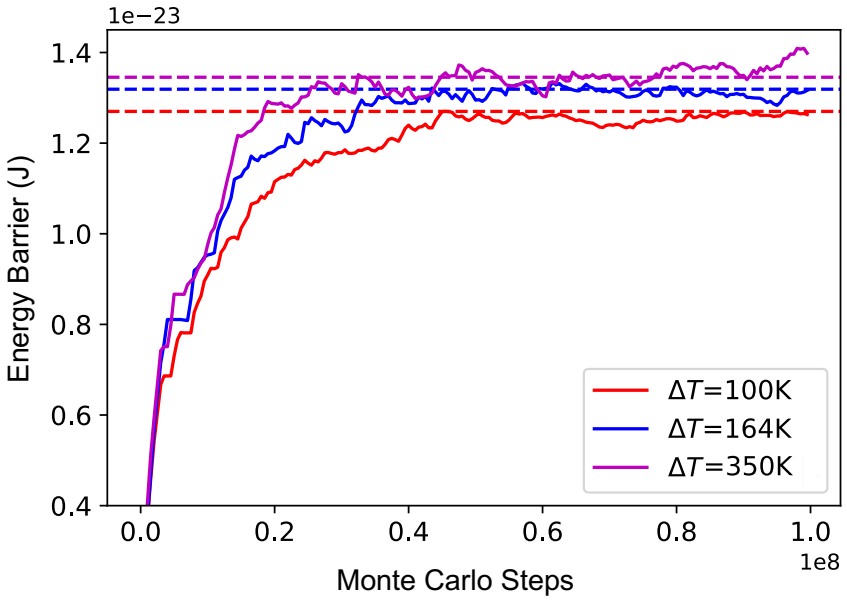

Figure 3.6: Energy barrier convergence with the expected values of K_{u} shown as dashed lines.

As seen in figure 3.6, the functions developed can give accurate estimations of the energy barriers associated with the selected CV; if the metadynamics parameters are chosen wisely. In addition, the effect of the ΔT upon the speed and accuracy of the simulation can be seen. We get the highest accuracy with a high computational cost for a $\Delta T < E_{\mathrm{ex}}$. In figure 3.6 (red line), the estimated energy barrier converges at 8×10^7 MC steps with the highest accuracy (i.e. less fluctuation around the convergence point (dashed red line). In comparison, for $\Delta T = E_{\mathrm{ex}}$ and $\Delta T >> E_{\mathrm{ex}}$, the energy barrier reaches the convergence points 30×10^6 and 50×10^6 less MC steps with progressively larger fluctuations. This is because as we increase ΔT, we decrease the rate at which we scale down the Gaussian height.

3.4 Magnetic Anisotropy Scalling

The final code validation and study of the anisotropy scaling was conducted by comparing the tempered metadynamics results of the anisotropy scaling against the Callen-Callen theory using the out-of-plane magnetisation as the CV. In 1965, Callen-Callen analytically showed that the single-ion anisotropy energy exhibits a power scaling proportional to temperature according to [102]

$$K \propto M(\mathrm{T})^3 \tag{3.2}$$

where K is the magneto-crystalline anisotropy energy, and $M(\mathrm{T})$ is the thermodynamical equilibrium normalised magnetisation for a given temperature. This temperature dependence of anisotropy has been successful and demonstrated experimentally multiple times. However, the Callen-Callen theory excludes any magnon-magnon interactions. For high temperatures relative to the Curie temperature of the system, the exponent differs from 3.2 to account for the magnon-magnon interactions. Hence, in the final test, only the low-temperature limit, where $m_{\mathrm{z}}(\mathrm{T}) \approx 0.80$, is considered to examine the power scaling law of K as shown in 3.2.

As explained, the associated energy barrier of the FEL is reconstructed using m_{z} as the CV is the magnetocrystaline anisotropy. Thus, the Callen-Callen theory is tested against the energy barriers extracted from the FELs of a ferromagnet in a range of temperatures with metadynamics, ensuring that the developed metadynamics code is accurate. Interestingly in 2019, a similar study published at the same time this analysis had been started used metadynamics to metadynamics to study the temperature dependence and spin re-orientation of the magnetic thin film, using $m_{\mathrm{saturation}}/m_{\mathrm{z}}$ as a CV [87].

In this test, the FELs of a $20 \times 20 \times 20$ simple cubic lattice in a temperature range of 10K up to 180K were reconstructed using the magnetic and metadynamic parameters shown in table 3.2.

For every temperature, 15 independent simulations were conducted. Their average reconstructed FELs are shown in figure 3.7. The two minima on each FEL on the plot show the thermodynamic equilibrium magnetisation,$\pm m_{\mathrm{z}}(\mathrm{T})$, which decreases with increasing the tem-

Tempered Metadynamics Parameters	
w_{initial}	0.5×10^{-24} J
σ	0.001
ΔT	$200K$
$K_{\text{u}} = 1.4 \times 10^{-23}$J , $E_{\text{ex}} = 3.55 \times 10^{-21}$J	

Table 3.2: Tempered metadynamics and magnetic simulation parameters used for the magnetic anisotropy scaling study

perature as expected. Similarly, the maximum point between the two minima decreases as we expect the MAE to decrease, as the power law states. The ”crosses” on the two minima and the maximum point are automatically placed from our analysis code in Python, which is used to extract the MAE from these FELs. This code was developed to find the minima at each individual FEL and the maximum point between the minima identified. The energy barriers are then calculated by subtracting the minima values from the maximum value point.

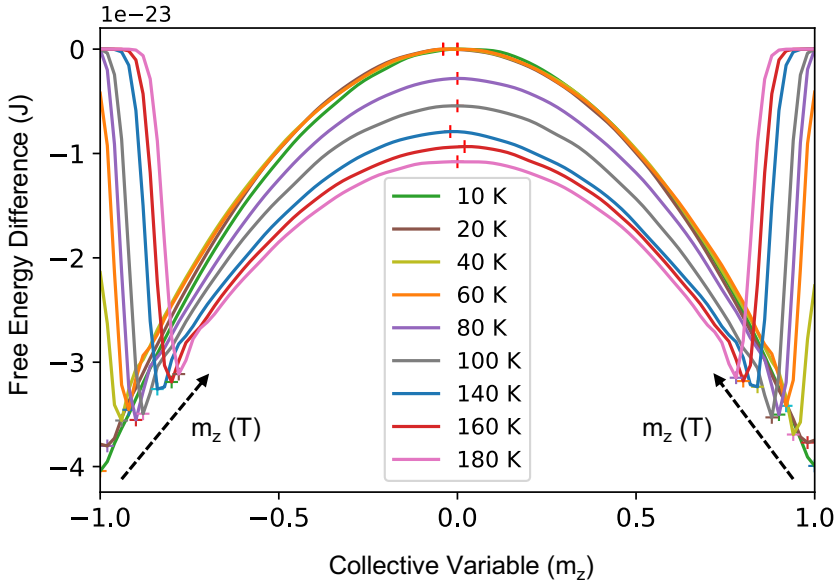

Figure 3.7: Reconstructed Free Energy Landscapes as a function of increasing temperature

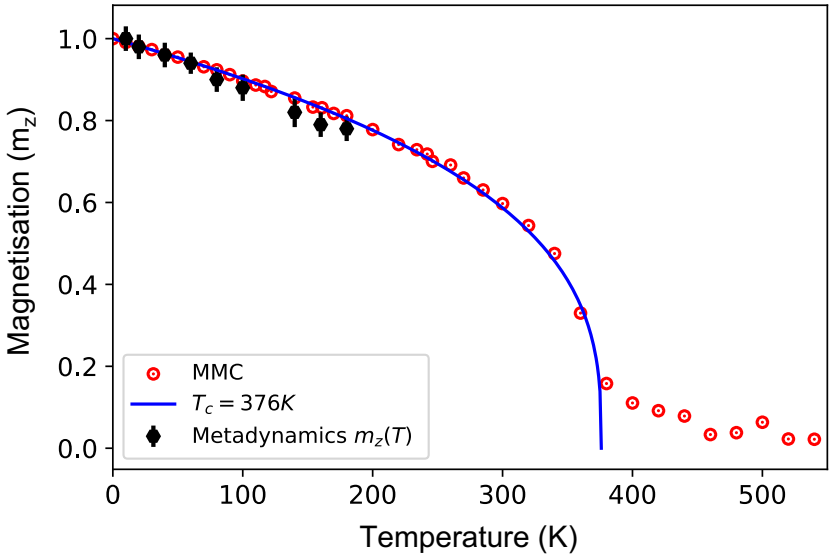

Figure 3.8: Temperature against magnetisation simulations data; red data points, plotted against the extracted thermodynamic equilibrium magnetisations from the FELs reconstructed with tempered metadynamics shown as black data points with their associated errors.

Additionally, plain Monte Carlo simulations were conducted to extract the thermodynamic equilibrium magnetisation m_{z} up to 550K to test if it matches with the m_{z} from the minima point in figure 3.7 and further validate metadynamics. Finally, the minimum magnetisation points are plotted against $m_{\mathrm{z}}(\mathrm{T})$ data from the plain Monte Carlo simulations in figure 3.8.

In figure 3.8, the extracted metadynamics data fit the $m_{\mathrm{z}}(\mathrm{T})$ data, further validating our code's accuracy. The error in the data points is calculated as the standard error from the 15 independent metadynamics simulations. Additionally, from figure 3.8, the Curie temperature of our system is found to be at 376K.

Finally, the MAE extracted from the FEL landscapes are plotted in figure 3.9. Every point on the plot averages 15 simulations for every temperature, with the standard error of the MAE calculated as the standard error between the 15 simulations. The fitting of the results is presented as the solid red line, and the theoretical prediction of the Callen-Callen theory as the dashed yellow line. There is a perfect agreement between the Callen-Callen theory and our well-

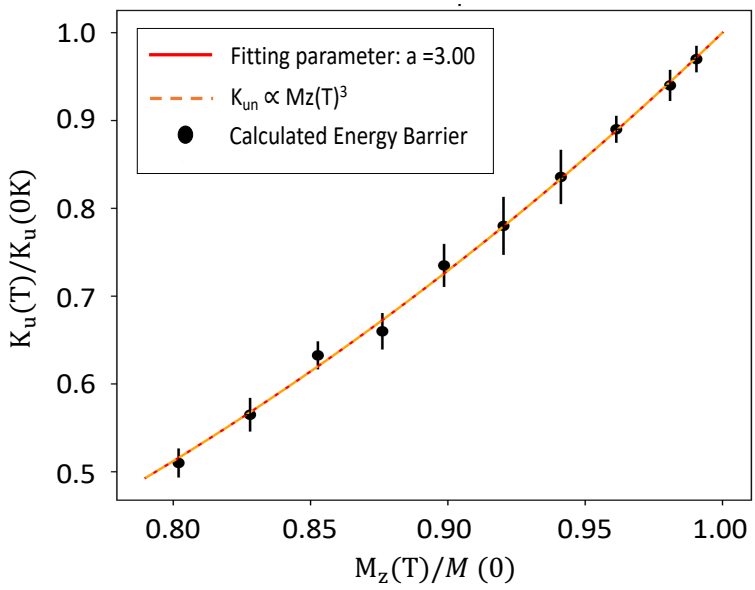

Figure 3.9: Magneto-Crystalline Anisotropy Temperature scaling. The dashed orange is a plot of the Callen-Callen anisotropy scaling, and the black scatter points are extracted from the FELs with the standard error from the 15 independent simulations. The fitting parameter of the extracted points shows a perfect match between the Callen-Callen theory and the results from metadynamics

tempered simulations.

In figure 3.9, it is also observed that the standard error decreases with increasing temperatures. This is because the CV crosses the energy barrier more times in higher temperatures due to the larger thermal fluctuations; thus, the better the sampling of the energy barrier. Therefore, in principle, the longer the metadynamics simulation, the smaller the error will be since the better the sampling of the energy barrier. Furthermore, since the reconstructed FELs have a mirror symmetry at $m_z = 0$, the simulations could have been conducted faster by setting the CV physical space $y(x) \in [0, -1]$ or $[0, +1]$ since we are using the mirror boundaries. Additionally, the CV of m_z/m_s used in the recent publication samples the maximum point of the FELs shown in 3.7 better than the CV used in this study. However, this study aimed to validate our code developed and test the metadynamics parameters' effect on the accuracy of

metadynamics. Thus the m_z was selected for our study and validation.

In this project, metadynamics is used with more than one CV. Having validated the metadynamics code using a single CV and studied the magnetic scaling using metadynamics, the code using multiple CVs is tested. To do so, the FEL, as in the tempered metadynamics test, was reconstructed using the m_z and the perpendicular to m_z, $m_{[001]}$ as CVs. The reconstructed free energy landscape is presented in figure 3.10.

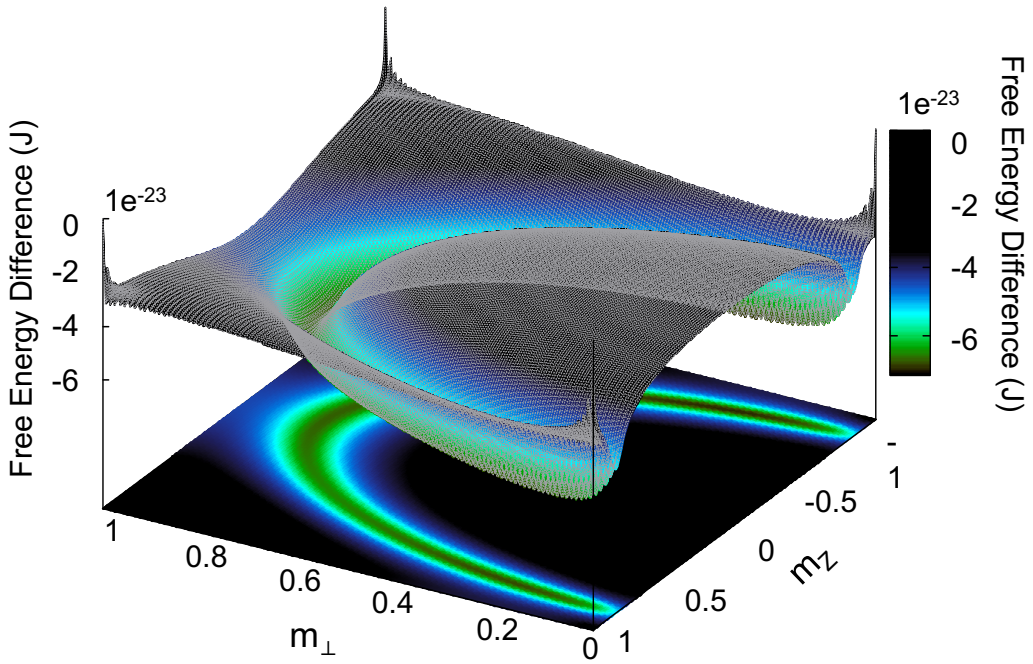

Figure 3.10: 2D and 3D reconstructed FEL using tempered metadynamics with two CVs used.

In figure 3.10, the thermodynamic equilibrium at the given temperature is at $m_z(10\text{K}) = \pm 0.98$. The minimum energy path is along the $\langle m \rangle$ where $\langle m \rangle = (m_z^2 + m_\perp^2)^{0.5} = 1$. The area below the minimum energy path where $|m| < \langle m \rangle$ has a high energy cost as the system must work against the exchange energy to be in that area. The region above the minimum path $|m| > \langle m \rangle$ work to align the spins against the entropy of the system introduced by the finite temperature. Thus the anisotropy energy of the system can be calculated by considering the maximum and minimum values along the minimum path, which effectively describes the

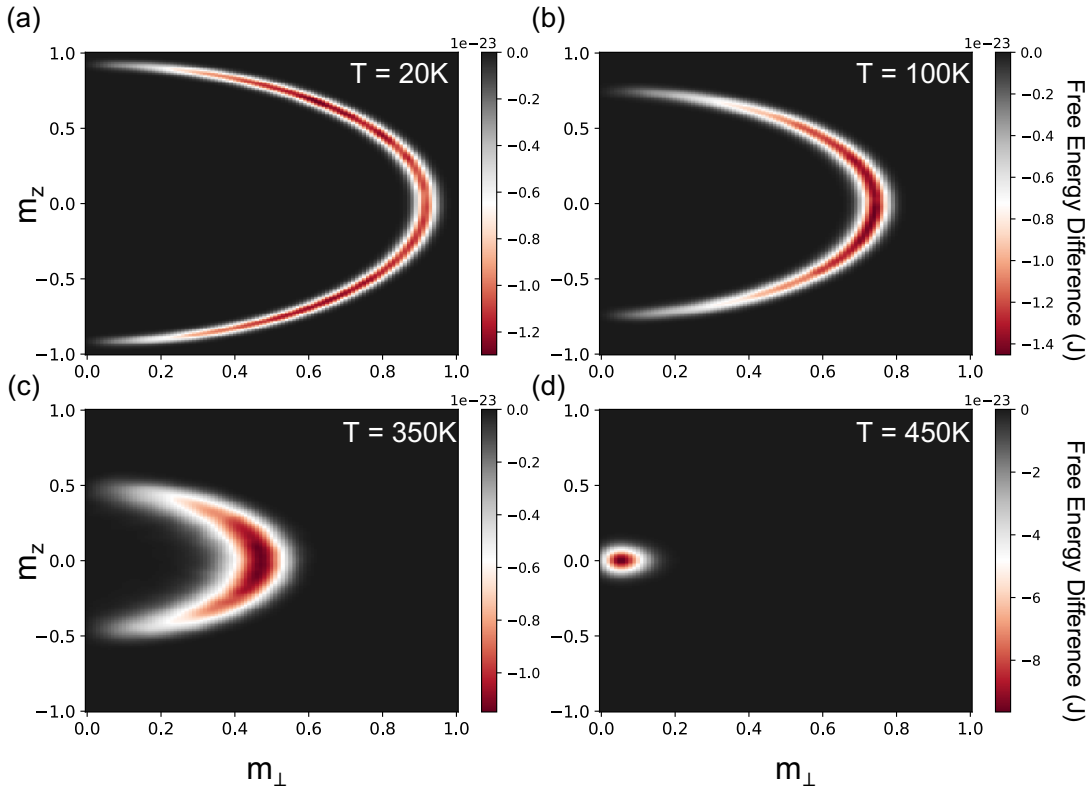

Figure 3.11: Reconstructed FEL using the tempered metadynamics with the out-of-plane m_z and the magnetisation perpendicular to m_z as CVs as a function of increasing temperature.

anisotropy energy barrier. Finally, the FEL change as a function of temperature is presented in figure 3.11. As expected, the $m_z(\mathrm{T})$ keeps decreasing with increasing temperature. For $m_z(\mathrm{T} > \mathrm{T_c}) \approx 0$ since the system has become paramagnetic as shown in figure 3.11

CHAPTER 4

Skyrmion Metastable Energy Paths

Skyrmions are defined by their integer topological charge, Q. The metastable skyrmion energies and all the transition energy paths are sampled and calculated with metadynamics by selecting CVs that fully describe the phase transition between a skyrmionic state to a ferromagnetic state and distinguish between different states with the same Q and vice versa. During these transitions, there is a change in Q and the out-of-plane magnetisation m_z. If only Q is used as a CV, the resulting energy barrier estimation will have large margins of errors since the transition is not fully described due to the hidden degrees of freedom; resulting in overfilled 2D FEL minima, as described in section 2.3.1 and schematically illustrated in figure 2.3 since they will include the sampling of the hidden degree of freedom. This is because for a certain value of Q there are many skyrmion states due to the broad range of energies corresponding to different sizes of skyrmion and the possible chiral features in the lattice, which are not distinguished using only Q as a CV. Hence Q and m_z must be used as CVs to distinguish between different states with the same topological charge values resulting in 3D reconstructed FEL.

Additionally, in principle, the configurational space of Q spans between $[-\infty, \infty]$; thus, restricting the configurational space with hard boundaries will break the ergodicity of the simulation as well as introduce large systematic errors near boundaries of the set topological charge's configurational space.

In this chapter, a description of the possible ansatzes to calculate Q in a spin-lattice are introduced to explain the selection of the calculation ansatz of Q used as a CV. Then the boundaries constructed to ensure that the ergodicity of the system is not hindered while sampling only a part of the topological charge configurational space of interest are introduced. Finally, the results, using the methods described, are presented.

4.1 Topological Charge Calculations

Often, the topological charge is estimated by coarse grain sampling, which is unable to resolve small topological features which are of interest on a lattice. But estimating topological charge on a discrete and finite system is by no means a trivial problem. One way to estimate topological charge has been proposed in 1981 by Berg, where a quasilocal definition of topo-

logical charge on a finite lattice with periodic boundary condition, which results in an integer value of topological charge, has been proposed [103]. Similarly, in the continuum limit, coarse grain sampling for the topological charge yields an integer value, but on a finite lattice, without periodic boundary conditions, estimators of topological charge can have non-integer values.

In this subsection, the two most commonly used ansatzes in condensed matter magnetism and their use as CVs are discussed.

4.1.1 Geometrical Definition of Topological Charge

The geometrical definition of topological charge is based on computing the spherical angles, q_{ijk} spanned by triplets i, j, k of neighbouring spins $\mathbf{S}$, per lattice point. Then the topological charge can be estimated using the following expression [104]

$$Q = \frac{1}{4\pi} \sum_{\langle ijk \rangle} q_{ijk} \tag{4.1}$$

where the spherical angles q_{ijk} of each triplet are calculated as

$$\tan\left(\frac{q_{ijk}}{2}\right) = \frac{\mathbf{S}_i \cdot (\mathbf{S}_j \times \mathbf{S}_k)}{1 + \mathbf{S}_i \cdot \mathbf{S}_j + \mathbf{S}_i \cdot \mathbf{S}_k + \mathbf{S}_j \cdot \mathbf{S}_k} \tag{4.2}$$

where $\mathbf{S}$ are the directions of each spin. Equation 4.1 counts the number of times the spin directions cover a unit sphere. In practice, this algorithm takes two triangles per lattice site, where every triangle is defined by three neighbouring spins, covering the whole lattice area. However, it is necessary to avoid double counting areas when summing up all the triangle contributions [104]. The main benefit of this algorithm is that it considers individual lattice points, resulting in integer values of Q, does not include computationally expensive differentiations and is easy to compute numerically on a finite lattice of any geometry with or without periodic boundary conditions.

This algorithm was first used for magnetic skyrmions in a lattice by J. von Kim in 2020 within the micromagnetics framework [104]. As demonstrated, this calculation offers a more reliable and accurate way of calculating the topological charge in finite temperatures, which is used to monitor Q. However, here Q is used as a CV which drives the dynamics of the lattice. Thus when this algorithm is used as a CV, two limiting cases are encountered, which

were reported in the original paper in 1981 by B.Berg and occurred when the nominator or denominator in equation 4.2 are [103]

$$\mathbf{S}_i \cdot (\mathbf{S}_j \times \mathbf{S}_k) = 0 \quad , \quad 1 + \mathbf{S}_i \cdot \mathbf{S}_j + \mathbf{S}_i \cdot \mathbf{S}_k + \mathbf{S}_j \cdot \mathbf{S}_k \leq 0 \tag{4.3}$$

For these exceptional spin configurations, the calculated spherical angle q_{ijk} lies along the complex plane [103]. When these limiting cases occur in the metadynamics simulation, single spins change the topological charge value and appear ”frozen”, as shown in a snapshot of a simulation of a nanowire at 40K where the CV was set as the geometrical definition of the topological charge in figure 4.1

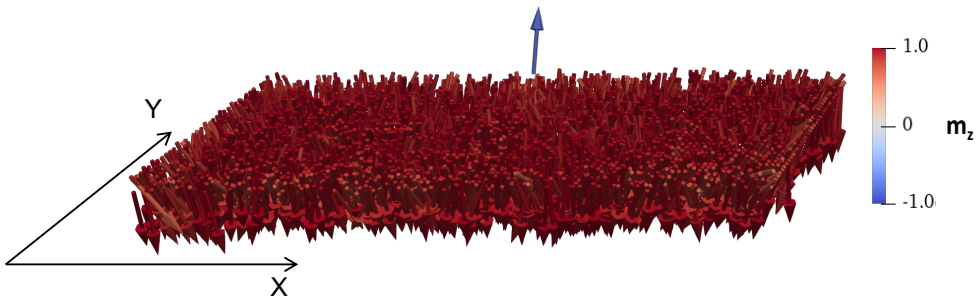

Figure 4.1: Snapshot during a metadynamics simulation of a nanowire with the topological charge geometrical definition set as a CV, demonstrating the limiting cases of the algorithm when used as a CV

Additionally, this algorithm results in integer values of topological charge. Thus it can not be used as a CV since it can not describe the slow modes of the transition from the skyrmionic state to the ferromagnetic and vice versa. However, the algorithm is still of high importance for this and any continuation of this project, as it will be discussed in section 6.

4.1.2 Finite Difference Topological Charge Calculation

In the continuum limit, the topological charge is defined as

$$Q = \frac{1}{4\pi} \int \mathbf{m} \cdot \left(\frac{\partial \mathbf{m}}{\partial x} \times \frac{\partial \mathbf{m}}{\partial y} \right) \mathrm{d}x\mathrm{d}y \tag{4.4}$$

Using finite difference approaches to estimate the derivatives and considering the hexagonal lattice, equation 4.4 can be approximated as with the following expression [105]

$$Q = \frac{1}{4\pi}\sum_{i}\left[\left(\frac{\mathbf{S}\left(\mathbf{r}_i+\mathbf{u}_1-\mathbf{u}_2\right)+\mathbf{S}\left(\mathbf{r}_i+\mathbf{u}_2\right)-\mathbf{S}\left(\mathbf{r}_i-\mathbf{u}_1+\mathbf{u}_2\right)-\mathbf{S}\left(\mathbf{r}_i-\mathbf{u}_2\right)}{2}\right)\right. \\ \left.\times\left(\frac{\mathbf{S}\left(\mathbf{r}_i-\mathbf{u}_1+\mathbf{u}_2\right)+\mathbf{S}\left(\mathbf{r}_i+\mathbf{u}_2\right)-\mathbf{S}\left(\mathbf{r}_i+\mathbf{u}_1-\mathbf{u}_2\right)-\mathbf{S}\left(\mathbf{r}_i-\mathbf{u}_2\right)}{2\sqrt{3}}\right)\right] \tag{4.5}$$

where $\mathbf{u}_1 = \hat{\mathbf{x}}$ and $\mathbf{u}_2 = \frac{1}{2}\hat{\mathbf{x}} + \frac{\sqrt{3}}{2}\hat{\mathbf{y}}$ are the hexagonal lattice vectors within the cartesian plane as shown in the supplementary information of S. Rohart et al. in 2016 [105]. Compared with the geometrical definition of the topological charge, this calculation is a coarse grain estimation, thus being sensitive to thermal fluctuations. Because of that, the topological charge values calculated using 4.5 are continuous, which can be used to sample the slow modes of the transition from a ferromagnetic state to a skyrmionic state and vice versa. It is often reported that the skyrmion creation process is not continuous. However, as discussed in section 4.3, the metadynamic simulations demonstrate the non-continuous process during the skyrmion creation is the generation of a Bloch point which is a single abrupt event. Then the skyrmion is stabilised by generating the skyrmionic spin profile around the Bloch point. Thus the continuous calculation values of topological charge are required to fully describe the transition from a ferromagnetic to a skyrmionic state. In contrast, using the geometric definition of the topological charge, we only get Bloch points but not a stable skyrmion configuration similar to what is shown in 4.1.

The drawbacks of the finite difference calculation of Q are that it is computationally expensive and since it is sensitive to thermal fluctuations, errors arise in the calculation of the topological charge for temperatures near the T_{C}, as reported and discussed in section 6 [105]. However, this is the only topological charge calculation that can be used as a CV in a spin-lattice to sample the transition from a ferromagnetic to a skyrmionic state.

4.2 Restoring Boundary Conditions

The configurational space of m_z is within the range of $[-1, +1]$. The mirror boundaries introduced in section 3.2 are used to reduce the systematic errors in low temperatures when the sat-

uration magnetisation is near the boundaries. In principle, the configurational space of the topological charge, Q is within $[-\infty, +\infty]$. However, only the region within $y(Q) = [-2.5, 2.5]$ is of any interest since a finite lattice is wished to be sampled, which metadynamics will explore by creating up to two skyrmions. This is because metadynamics is restricted by the computational power available, and the smaller the lattice, the faster the metadynamics simulations. Thus if the Q range is expanded and more than two skyrmions are introduced, larger lattices must be used to avoid the interaction between skyrmions which will affect the reconstructed FEL. Thus boundary conditions must be applied to ensure that only the region of interest is sampled.

If no boundary conditions are used, the system will explore increasingly large space without converging, and two more major limitations arise from the predefined potential histogram $N(y(Q), t)$. First, in principle $y(Q) = [-\infty, +\infty]$, however, $N\left(y(Q), t\right)$ has a finite size divided in equally spaced bins where the value of the Q during the metadynamics simulations is interpolated to find the centre which the Gaussian will be deposited and stored. Hence, any Q value larger or lower than the limits of the potential histogram will be interpolated at the edges of $N(y(Q), t)$ during the simulation resulting in large margin of errors. Additionally, once the system creates a spin texture that results in a $|Q| > 2.5$, the bias potential built near the boundaries of $N(y(Q), t)$ will repulse the system from adapting any configuration within the range of interest within the $y(Q) = [-2.5, 2.5]$ (i.e. potential will be continuously accumulated at the boundaries of $N(y(Q), t)$).

Similarly, if hard boundaries are used by setting a constant large potential at the edges of the $y(Q)$ to restrict the system from adapting spin configuration, which results in Q beyond the range of interest, two main limitations will occur. First, the systematic error at the boundaries will be large since the region around the boundaries will be oversampled. Secondly, the ergodicity of the system will be hindered, making the metropolis monte carlo algorithm invalid.

To resolve these issues, we use restoring boundaries developed to sample only the region of interest without breaking the system's ergodicity, which procedure is illustrated in the schematic in figure 4.2. These boundaries work similarly to a harmonic spring potential, allowing the system to explore regions outside a defined region but pushing the system back towards

the region of interest. The restoring boundaries were inspired by the recent study where metadynamics applied in a Quantum Chromodynamic System (QSD) to overcome the so-called topological freezing observed in high energy physics, where a similar boundary condition was used [97].

Here the restoring boundaries use the V_{bias} built within the $N(y(Q),t)$ to alter the metropolis monte carlo simulation transition probability in order to bias the system into exploring the region of interest. When the system creates a spin configuration resulting in the CV value beyond the range of $y(Q)$, a constant restoring potential $V_{\mathrm{res}}(Q)$, which strength depends on the distance between the upper and lower thresholds Q^{th} from the CV value of calculated is used. Here the upper and lower Q^{th} define the range of the $y(Q)$ sampled. The $V_{\mathrm{res}}(Q)$ is given by the following expression

$$V_{\mathrm{res}}\left(Q\right)=\begin{cases} V_{\mathrm{res}}\left(Q\right)=k*\left(y\left(Q\right)-Q^{\mathrm{thr}}\right)^{2}+N\left(Q^{\mathrm{thr}},t\right), & \text{if } |Q|\geq|Q^{\mathrm{thr}}, \\ V_{\mathrm{res}}\left(Q\right)=0, & \text{otherwise.} \end{cases} \tag{4.6}$$

where k is a dimensional constant, $y\left(Q\right)$ is the calculated CV value larger than the threshold set Q^{thr} and $N\left(Q^{\mathrm{thr}},t\right)$ is the accumulated bias potential on the histogram at the upper or lower Q^{thr} during the MC step t. While the system configuration results in $y(Q)$ larger than the $|q^{\mathrm{thr}}|$ no Gaussian are accumulated in the $N(y,t)$, and the metropolis transition probability is biased with the V_{res} instead of the V_{bias}. These boundaries allow the system to explore all possible configurations, ensuring that the ergodicity is not broken. However, the restoring potential push the system back into the configurational space of interest, which is sampled.

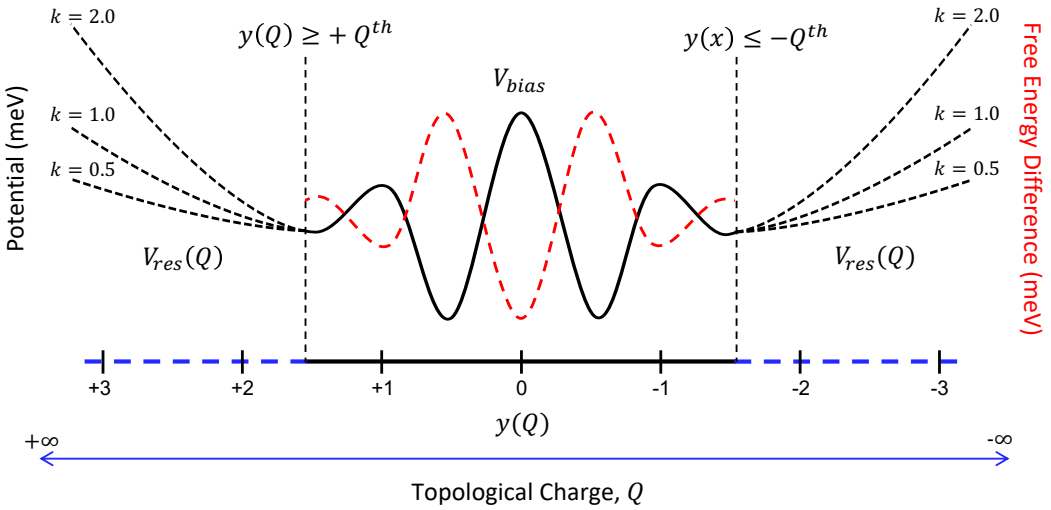

Figure 4.2: Restoring boundary conditions schematic

4.3 Metastable Skyrmion Free Energy Landscapes

For this investigation a $65 \times 65 \times 1$ hexagonal single-layer lattice with periodic boundary conditions applied along the x and y axis with the magnetic parameters shown in table 4.1 The

Magnetic Parameters	
Exchange Energy	$J = 13.00$ meV
Anisotropy	$K_u = 0.09$ meV
DMI	$D = 0.811$ meV

Table 4.1: Magnetic parameters used for the results in sections 4.3 and 5. As it is demonstrated in a paper that uses GNEBM, these parameters can host metastable skyrmions; thus selected for the following studies [2].

FELs were reconstructed using well-tempered metadynamics with the simulation parameters presented in table 4.2 for temperatures of 16K to 54K. For each temperature, 10 independent simulations were run. As shown in table 4.2, 190 million MC steps were run. This ensured that the whole FEL for each simulation was sampled. To ensure the FEL is fully sampled for each temperature, the relative Gaussian amplitude tempering is plotted as shown in figure 4.3 c. d.

for 26K and 48K, respectively. It can be seen that the relative Gaussian tempering within the whole FELs is below $0.1 * w$, showing that all potential wells are filled. For magnetisation values larger than thermodynamic equilibrium magnetisation $m_z > |m_z(T)|$ the system needs to exceed the entropic energy, which is a highly unprobable configuration, which is evident in figure 4.3. The errors in the average landscape for each temperature are calculated as the standard errors for each point and are shown in figure 4.3 a. and b. for temperatures 26K and 48K, respectively. This error could be further reduced by running the simulations for more MCS, reducing the amplitude of the initial Gaussian amplitude and decreasing the bias temperature ΔT. However, these improvements would significantly increase the computational time required for the simulations; each independent simulation required fourteen days (336 hours) of computations to finish on the ARC4 platform, part of the High-Performance Computing facilities at the University of Leeds, UK.

Metadynamics Parameters	
MC Steps	190×10^6 MCS
Gaussian Deposition stride	$\tau_g = 1$
Gaussian Amplitude	$\omega = 0.1\text{meV}$
Gaussian Width (Q)	$\sigma_Q = 0.1$
Gaussian Width (m_z)	$\sigma_{m_z} = 0.05$
Bias Temperature	$\Delta T = 2500K$

Table 4.2: Well-tempered metadynamics simulation parameters for the metastable skyrmion energy simulations.

Figure 4.4 presents an average 3D FEL. The colour map shows the free energy difference ΔF. The deep blue areas along the FEL in figure 4.4 show the region where the metastable spin excitations can be stabilised. All the other coloured shaded areas show the less probable spin configurations, which are not metastable. Near the top and bottom areas along the $\text{y} - \text{axis}$, the dark red region shows the high entropy cost required to push the m_z in values greater than the saturation magnetisation $|m_z(T)|$ for a given temperature as it is also shown in section 3. For $Q = 0$, there are three potential wells corresponding to the trivial FM states

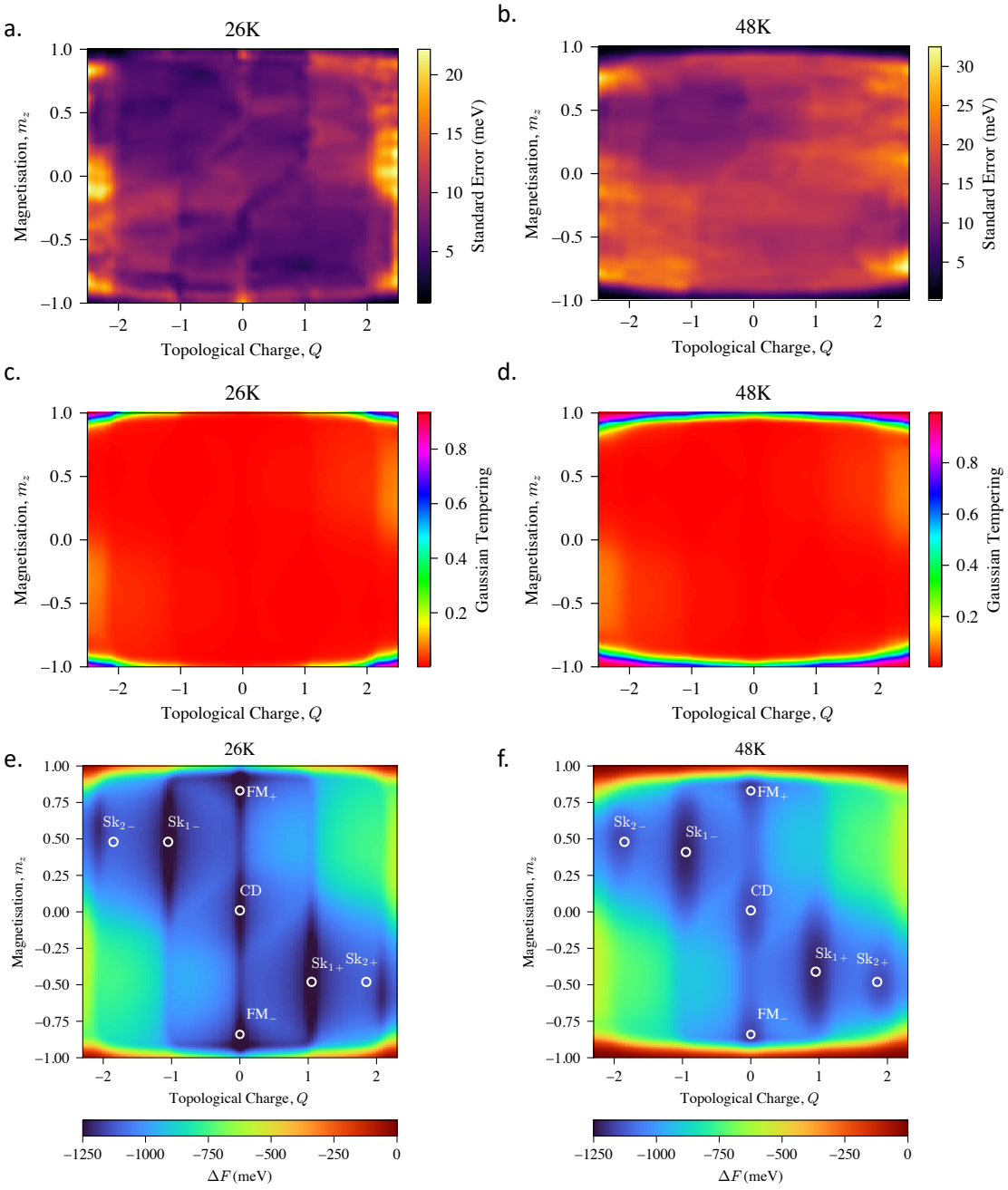

Figure 4.3: a. and b. show the standard error calculated from the independent metadynamics simulations where, as c. and d. show the average Gaussian amplitude tempering, demonstrating that metadynamics has explored the whole FEL. The plots at e. and f. show the average FELs at 26K and 48K, respectively.

at the thermodynamics equilibrium magnetisation for each temperature, $m_z(T)$ and a chiral domain intermediate state. Interestingly, the magnetisation reversal does not show coherent rotation. Instead, a Chiral Domain (CD) is formed, which expands to revert the out-of-plane magnetisation. As is shown in section 5.1, this is expected due to the DMI present, which lowers the energy of the out-of-plane magnetisation reversal by forming the metastable CD, as shown in figures 5.6 and 5.7. For $Q < 0$ and $m_z > 0$, up to two skyrmions are formed with negative polarity at the point Sk_{1-} and Sk_{2-}. A diagonal mirror plane symmetry is observed as expected due to the m_z reversal, where skyrmions with positive polarity are formed at points Sk_{1+} and Sk_{2+}. The surface along the y-axis between $\pm 0.25 \leq m_z \leq \pm 0.7$ at points $Q = \pm 1$ and $Q = \pm 2$ is shallow. This shows that the skyrmions in this lattice are soft, meaning that small energies are required to expand or contract the skyrmion radii.

Additionally, antiskyrmions form when metadynamics pushes the system to explore the regions of the FEL for the same sign of m_z and Q. These antiskyrmions are not stable since at $\mathrm{ASk}_{1\pm}$ and $\mathrm{ASk}_{2\pm}$ points, there are no minima observed. However, the formation of the antiskyrmions highlights that metadynamics can be used to explore all possible spin configurations, which no other study has demonstrated before for magnetic skyrmions and topological spin structures.

Two energy paths are observed as shown in figure 4.5, identified using the MEPSAnd python interface [5]. MEPSAnd is a minimum energy path analysis path code that offers a Python interface [5], which is used here to automate the exploration of the energy paths in the reconstructed FEL and identification of the energy minima points used to calculate the energy barriers present. MEPSAnd calculates the minimum energy path by finding the nearest energy minimum neighbouring points along the FEL between two energy minima regions.

The first energy path is shown in figure 4.5 a. and b. where first a Bloch point is created, which results in $Q = \pm 1$ for the $m_z = \pm m_z(T)$. Once the Bloch point is created, a skyrmion is created around this point resulting in the reduction of the $\pm m_z(T)$ due to the opposite polarity of the skyrmion with respect to the $\mathrm{FM}_{\pm}$. This energy path is the only energy path sampled in the studies using the GNEBM [2, 3, 54] and in the early experimental observation of skyrmions in low temperatures, this skyrmion creation has possibly occurred. The second energy path is

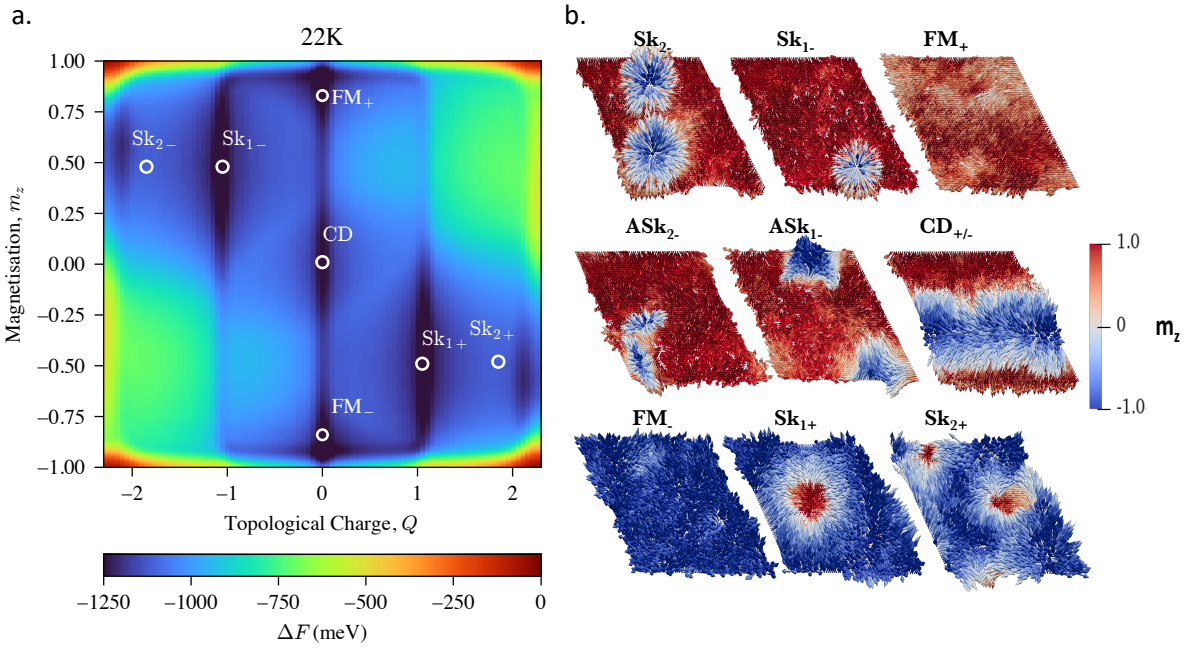

Figure 4.4: a. Reconstructed average of 10 independent simulations FEL indicating the location of the energy minima along the FEL where metastable spin textures are stabilised and b. shows their spin configuration. The abbreviations FM, Sk, ASk, and CD correspond to Ferromagnetic, Skyrmion, AntiSkyrmion and Chiral Domain. The $\pm$ under script states the polarity of the Sk and ASk and the sign of m_z for the FM states. Similarly, the numbering on the $\mathrm{Sk}_{\pm}$ and $\mathrm{ASk}_{\pm}$ shows the number of spin textures.

observed for temperatures higher than 36K, approximately $0.25 * T_C$. At higher temperatures, the thermal fluctuations increase resulting in chiral spin formation in the opposite m_z direction with respect to the FM state, as also shown in section 5.1. The second path in figure 4.5 c. and d. shows that these clustered spins can form a skyrmion. It can be argued that this transition path occurs experimentally, where skyrmions are created with a local laser pulse [106], which monumentally increases the temperature locally, which can result in these chiral features, which can then stabilise a skyrmion, as shown in our simulations or where field cycling protocols generate maze domains from which skyrmions are formed [107]. Similarly, skyrmions are experimentally created using the magnetisation reversal process, in which skyrmions are created during the reversal. Another feature observed in figure 4.5 it can be seen that the deep blue regions area at the metastable states gets larger with increasing temperatures. This is due to the onset of thermal fluctuations and thermally activated skyrmion modes. Additionally, to the paths described, there are more symmetrically equivalent paths along the FELs. However, these paths are highly unprobable, and the thermal fluctuations in higher temperatures result in large margins of errors which limits their accurate identification and quantification of the energy barriers associated with these paths.

Figure 4.6 show the 3D projections of the first energy paths for temperatures up to 36K. For temperatures up to 26K, the skyrmion creation has an additional energy barrier to exceed before a skyrmion is stabilised. This is shown in figure 4.6 a. where the red scatter points show the 3D projection of the transition from the $FM_{\pm}$ to $Sk_{1\pm}$. Physically, the transition occurs by creating a Bloch point at $Q = \pm 1$ and $|m_z(T)|$ point. Following the creation of the Bloch point, the additional energy barrier $\approx 50\mathrm{meV}$ need to be exceeded in order to continue in the stabilisation of the skyrmion. However, this small energy barrier becomes negligible for temperatures higher than 26K due to the increasing thermal fluctuations. Similarly, the 3D projections of the second energy paths observed in temperatures larger than 36K are presented in figure 4.7, where the 3D projections of the transitions from a single into two skyrmions are not plotted for clarity. Comparing figure 4.7 a. with b. it can be seen that the skyrmionic state becomes more stable than the ferromagnetic. This can be explained by the entropic barrier, which increases for a temperature range, which has been shown both experimentally [82], and

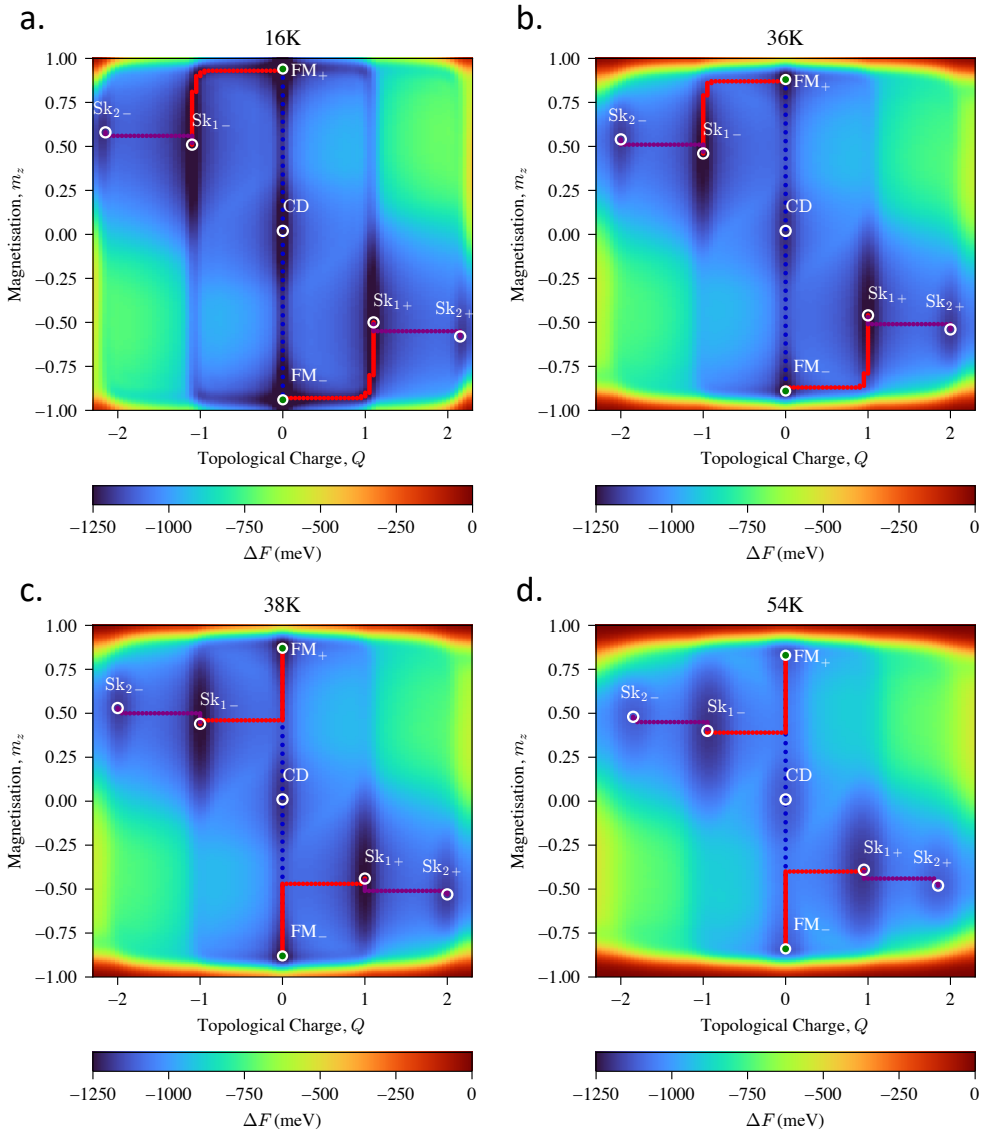

Figure 4.5: Reconstructed FELs using tempered metadynamics. Each FEL is an average of 10 independent simulations. Plots a. and b. show the first energy path observed, where a Bloch point initiates the skyrmion creation. Similarly, c. and d. show temperatures larger than 36K where the second energy path is observed. The energy paths were identified using the MEPSAnd python interface [5]

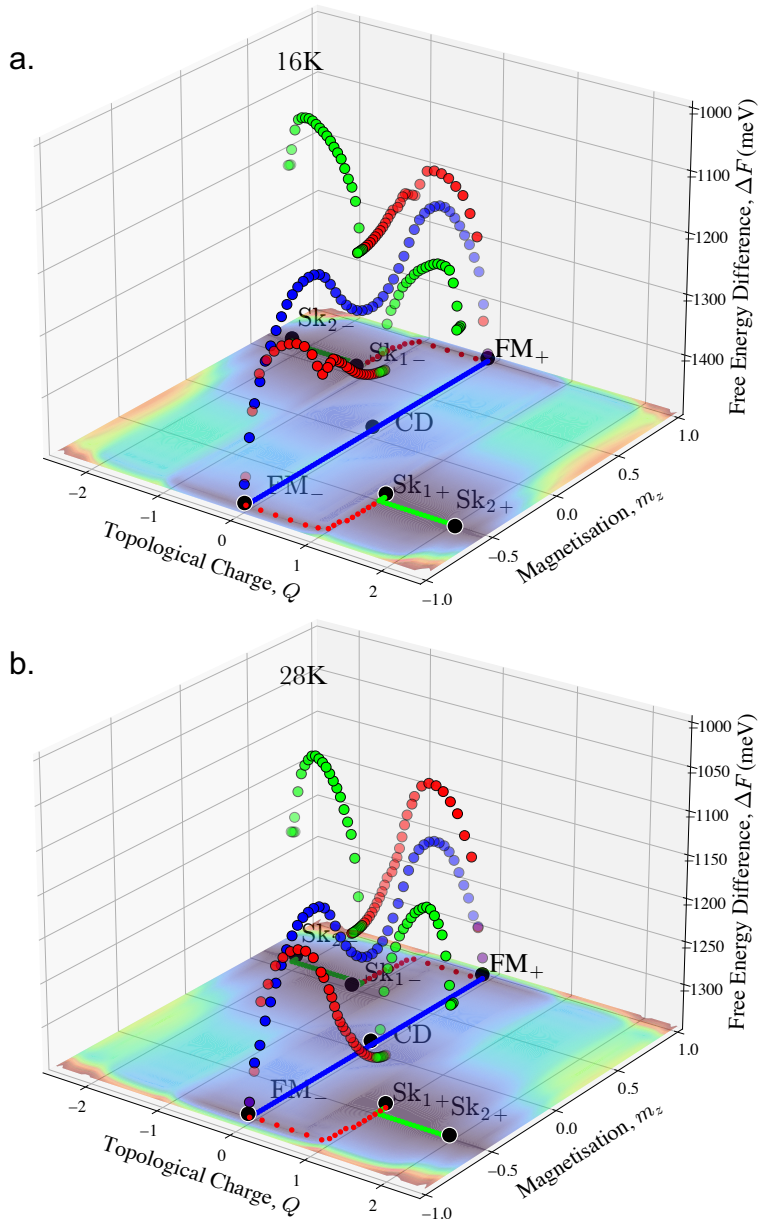

Figure 4.6: Diagrams showing the FEl at a. 16K and b. at 28K and the 3D projections of the magnetisation reversal energy path with the blue scatter points, the $FM_{\pm}$ to $Sk_{1\pm}$ transition path with the red scatter points and the $Sk_{1\pm}$ to $Sk_{2\pm}$ with the green scatter points.

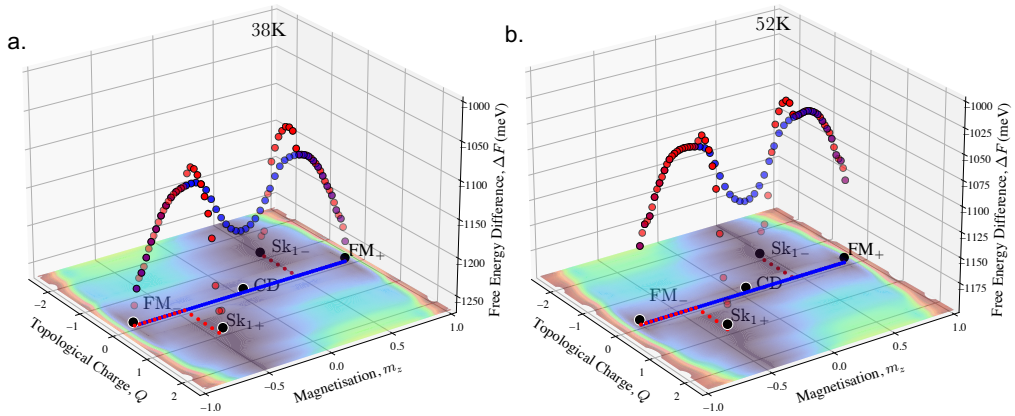

Figure 4.7: Diagrams showing the FEl at a. 38K and b. at 52K and the 3D projections of the magnetisation reversal energy path with the blue scatter points, the $FM_{\pm}$ to $Sk_{1\pm}$ transition path with the red scatter points.

theoretically [4], that is the main contributor to the skyrmion stability. Figure 4.8 shows the free energy difference of the points along the minimum energy paths for the transition from $FM_{\pm}$ to $Sk_{1\pm}$ and $Sk_{2\pm}$ clearly shown that as the temperature increases the skyrmionic spin configurations become more stable relative to the $FM_{\pm}$. Another, in figure 4.7, it can be seen that the energy minima along the $\mathrm{x}-\mathrm{axis}$ are uneven between the points at $Q = \pm 1$ with $Q = \pm 2$. This is due to the finite lattice, which makes two skyrmions energetically more costly in this lattice size and reflects the possibility that the skyrmions interact due to the lattice confinement.

From the reconstructed FELs, the creation and annihilation energies are calculated as the difference between the maximum and minimum points along their transition paths. The results are presented in figure 4.9 where a. and c. show the energies required to create single and two skyrmions within the lattice. Similarly, the energies required to annihilate the skyrmions are

shown in figure 4.9 b. and d. for single and two skyrmions, respectively. Each point in the plots in figure 4.9 is the average of the energy barriers calculated for the spin configurations with opposite polarity (i.e. Sk_{1+} and Sk_{1-}) and the errors are standard errors. The standard errors are not calculated from the averaged FEL at each temperature. Rather, the energy barriers of the 10 individual FELs for each temperature are extracted, and the standard errors of those barriers are calculated. This ensures that the errors will not be overestimated. For both the $Sk_{2\pm}$ and $Sk_{1\pm}$, the creation energy is reduced with increasing temperature. This is expected since the results discussed later in chapter 5 show that the thermal fluctuations leading to the chiral features in the opposite polarity relative to the ferromagnetic polarity can get stabilised into a skyrmion, thus with more thermal fluctuations, less additional energy is required to create skyrmions. On the contrary, for a single skyrmion, the annihilation energy increases with increasing temperatures up to 36K, where the first energy path is more energetically favourable. For temperatures higher than 38K, the annihilation energy slowly decreases but is still larger than the lowest temperature (16K). Similarly, as shown in figure 4.9 d. for two skyrmions, the annihilation energy increases up to 30K and then is reduced with increasing temperature. However, the annihilation energy for two skyrmions is half compared to a single skyrmion, which can be due to the small lattice size.

Figure 4.10 shows the crossover between the two different nucleation and annihilation paths at temperatures below 38K and highlights the extra energy that is required to nucleate or annihilate a single skyrmion with the second energy minimum path for each case observed in diagrams 4.5 4.6 and 4.7. As shown in figure 4.10 a., shows that for temperatures below 36K, the creation energy via domain nucleation paths requires more energy than the Bloch point path. Similarly, for temperatures below 36K, as shown in figure 4.10 b., the skyrmion annihilation requires more energy to get annihilated via a domain.

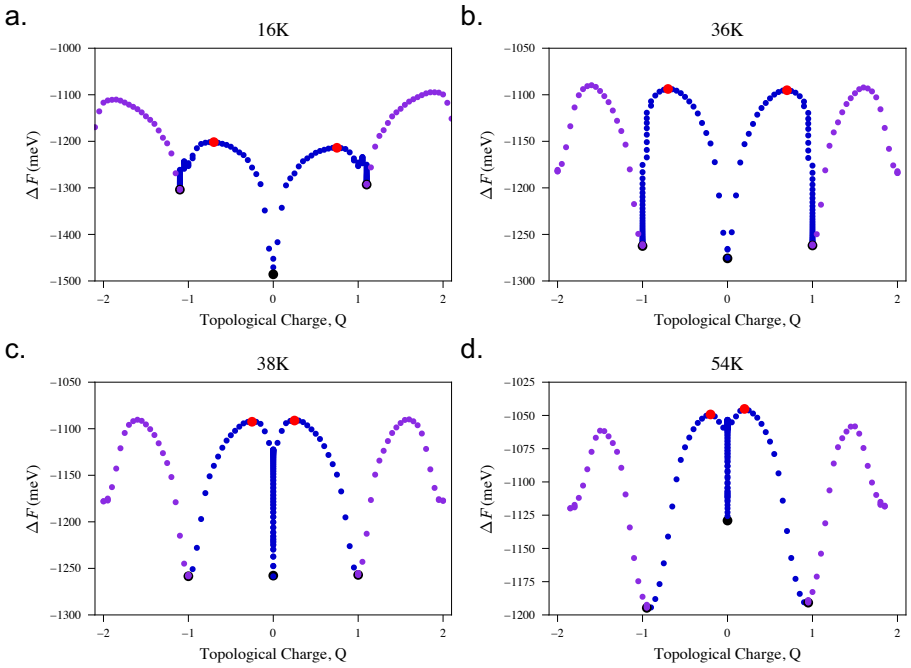

Figure 4.8: Plots of the free energy difference along the topological charge coordinate from the FM state to the $Sk_{\pm 1}$ and $Sk_{\pm 2}$. The red data points represent the maximum free energy difference ΔF points between the FM state and $Sk_{\pm 1}$.

The trend of the skyrmion annihilation energy with increasing temperature is shown in figure 4.9 b. and d. further validates the studies [3, 82] that showed that the difference in configurational entropy help to stabilise skyrmions. If the internal skyrmion energy was the only parameter responsible for the skyrmion stability, the energetics of the lattice with and without a skyrmion as a function of temperature should show an order parameter transition.

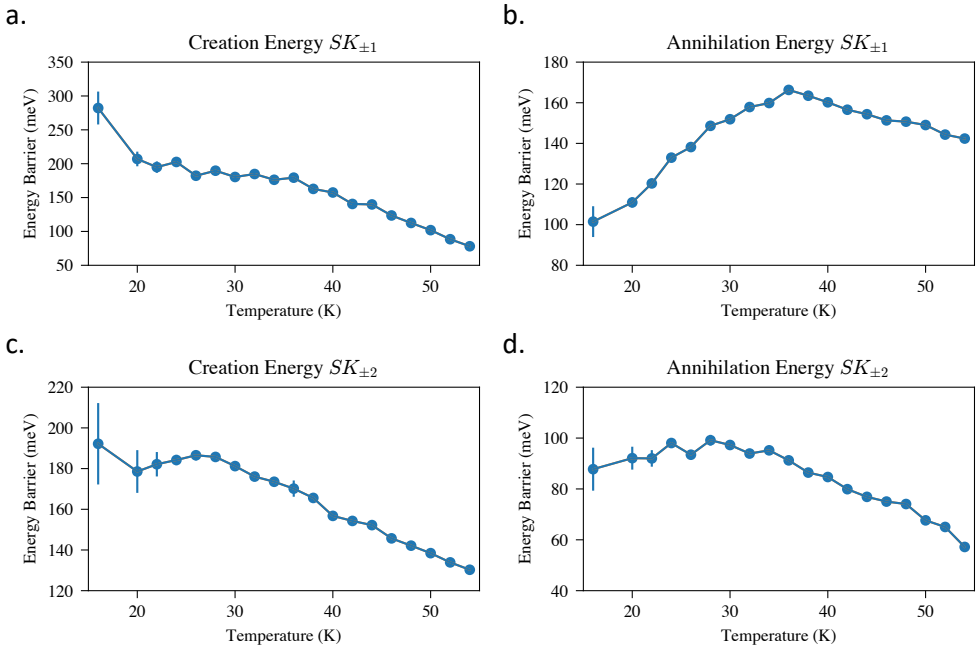

Figure 4.9: Plots of the calculated energy barriers from the FELs reconstructed with metadynamics as a function of temperature. Plots a. and b. present the creation and annihilation energy barriers for the single skyrmion formation and annihilation. Plots c. and d. show the energy barriers for the formation and annihilation of the two skyrmions.

Figure 4.11 a. and b. show the DMI and anisotropy energy as a function of temperature for a lattice with a skyrmion (orange scatter data points) and a lattice with a uniformly initialised ferromagnetic spin alignment. The lattice used for the results shown in figure 4.11 is the same $65 \times 65 \times 1$ used for this section, with the same magnetic parameters. For these results, the MMC simulation (without metadynamics) was used to thermalise the lattices for 500.000 MC steps. In the lattice with the skyrmionic spin texture, the skyrmion was initialised using the skyrmion profile as explained later in section 6.1. However, in figure 4.11 a. and b. at 82K, it can be seen that the skyrmion got annihilated prior to the lattice thermalisation; highlighting the importance of generating a thermalised lattice with a skyrmion to ensure that the skyrmion will not get annihilated prior to the lattice thermalisation which is further discussed in chapter 6.

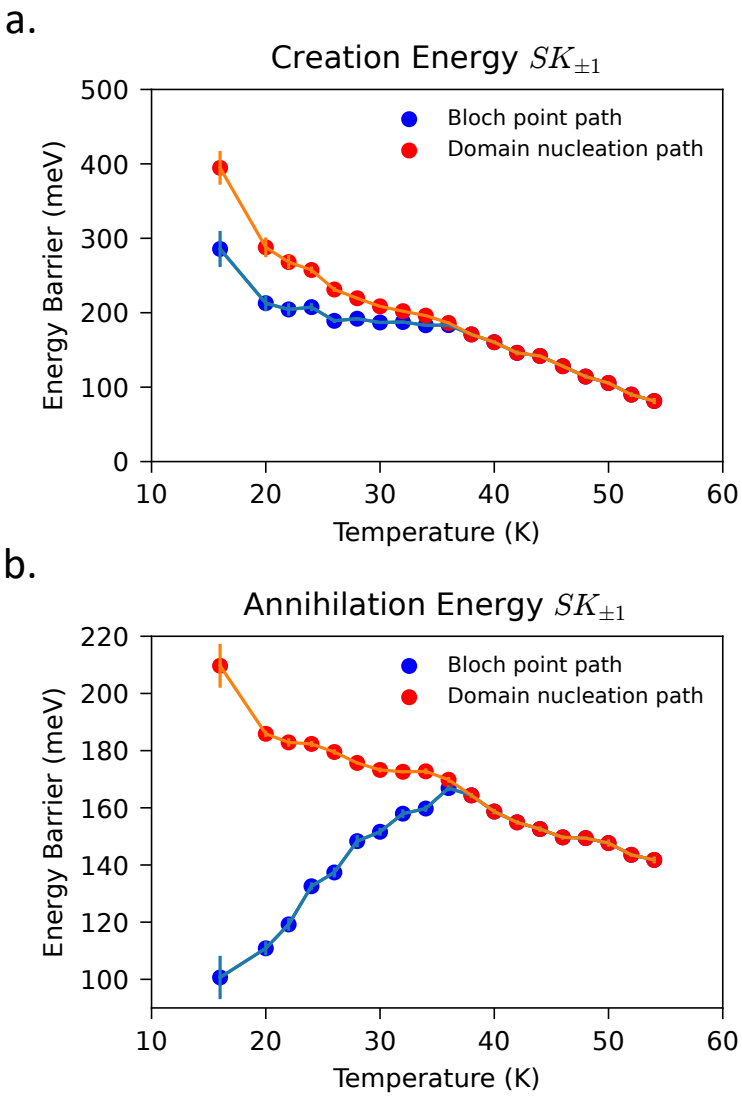

Figure 4.10: Skyrmion a. creation and b. annihilation energies via domain and a Bloch point path with the standard error calculated from the 10 independent simulations.

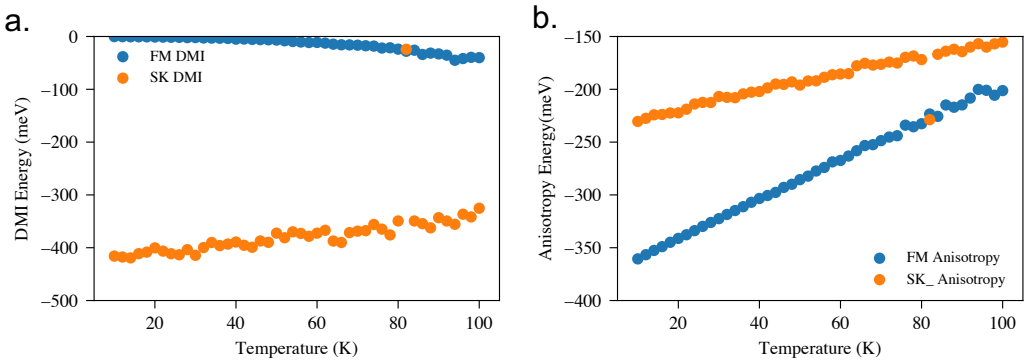

Figure 4.11: Comparison of the a. DMI energy and b. effective anisotropy energy against the temperature for the $65 \times 65 \times 1$ lattice initialised with a skyrmionic spin texture and a uniform ferromagnetic colinear spin alignment shown as the orange and blue scatter points, respectively.

As shown in figure 4.11 b., the anisotropy energy is reduced with increasing temperature in both lattices due to the increasing thermal fluctuations resulting in individual spin orientations away from the easy axis. The difference in the anisotropy energy between the two lattices is due to the presence of the skyrmion. The DMI energy is lower for the lattice with a skyrmion (orange data points) than the lattice with the ferromagnetic alignment due to the collinear spin alignment (blue data points). As the temperature increases, the DMI energy for the skyrmionic lattice increases due to spins within the skyrmion subjected to thermal fluctuations, which deform the skyrmion increasing the DMI energy of the lattice. On the contrary, for the ferromagnetic lattice where all spins are aligned collinearly, the DMI energy is reduced with increasing temperature due to the formation of the chiral spin features, which is later reported in chapter 5 where the study of the magnetisation reversal with metadynamics showed the formation of these chiral spin features. Despite the analysis of the energetics trends in figure 4.11; it is clearly shown that the skyrmion internal energy is not the detrimental factor in the skyrmion stability which is another evidence of the validity of the studies [4, 82] which demonstrated that the skyrmion stability is due to the internal and the entropic barrier.

CHAPTER 5

Magnetisation Reversal with DMI

In section 4, metadynamics revealed that the magnetisation reversal in a system with DMI occurs by the mediation of a metastable chiral domain state from which the magnetisation reversal occurs by the expansion of this chiral domain. To further investigate this finding, the system as in section 4 is tested with and without DMI. These simulations were conducted on a $65 \times 65 \times 1$ hexagonal lattice with periodic boundary conditions applied along the x and y directions, and the magnetic parameters are presented in table 4.1.

First, the Currie temperature with and without DMI is investigated using the Metropolis Monte Carlo algorithm to estimate the thermodynamics equilibrium magnetisation for a range of temperatures from $5 - 295\mathrm{K}$. The results are plotted in figure 5.1 for both systems and the magnetic susceptibility is calculated with the following expression

$$\chi = \frac{\partial \langle M \rangle}{\partial T} = \frac{1}{k_{\mathrm{B}} T} \left[\langle M^2 \rangle - \langle M \rangle^2 \right] \tag{5.1}$$

where $\langle M \rangle$ denotes the average magnetisation for a given temperature. Each simulation was initiated with uniform spin alignment along the $m_z = +1$ direction, and the system was thermalised for 90×10^4 MC steps. Without the DMI interaction in the system $T_{\mathrm{c}} \approx 156K$. Interestingly with the DMI, the Currie temperature is reduced to $T_{\mathrm{c}} \approx 136K$ with a phase transition occurring before it reaches the T_{c}, as indicated from the χ plot, which has two peaks in figure 5.2 a.; the first indicated with blue dashed lines and the second (T_{c}) with the black dashed line in figure 5.2 a. This is explained by investigating at the spin vector plots in figure 5.2 where a-c are the spin vectors for the lattice without DMI, and d-g is the lattice with DMI for selected temperatures bellow and above T_{c}. Thus, the reduction of the $\mathrm{T_C}$ could be due to the DMI, which tends to stabilise non-parallel arrangement of spins; resulting in a lower distance to revert the spins.

For the lattice without the DMI, as is expected, it can be seen that approximately $0.90 \cdot T_c$ in figure 5.2 a., there are few spins crossed in the negative m_{z} direction reducing the overall magnetisation without the spins having any correlation. Similarly, as the temperature increases, there is more randomness in the spin directions, and for $T > T_c$, the system has become paramagnetic. On the other hand, for the lattice with the DMI at temperatures higher than $0.60 * T_{\mathrm{c}}$ the spins that cross in the negative m_{z} direction cluster together and form a small local region where chirality is observed as shown in 5.2 d. As more spins are crossing to the

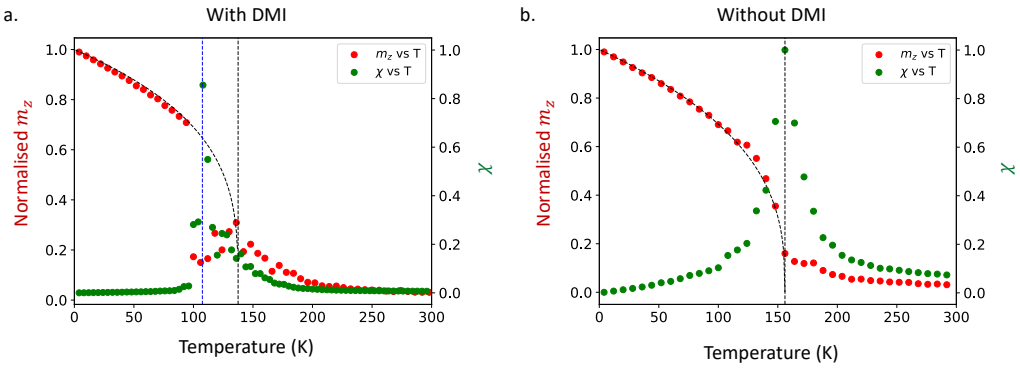

Figure 5.1: Plots showing the susceptibility and magnetisation against temperature for the lattice a. with DMI and b. without DMI. The black dashed line indicates the T_c. In a., the blue dashed line indicates a phase transition that the system before reaching the T_c

negative m_z direction, this effect is becoming more evident as in 5.2 e. Even for temperatures up to $0.95 * T_c$, the spins form local chiral domains as it is shown in 5.2 f. It is only for temperatures higher than $1.075 * T_c$ that the system becomes paramagnetic, as is shown in 5.2 g. This suggests that the system has to overcome two energy minima to go to a paramagnetic phase similar to the magnetisation reversal seen in section 4 and also evident from figure 5.1 a. However, the T_c of the system is at $\approx 136K$. The local chiral domains and spin directions that are seen for temperatures higher than the T_c are instant, unstable and only create noise near the T_c as seen in figure 5.1.

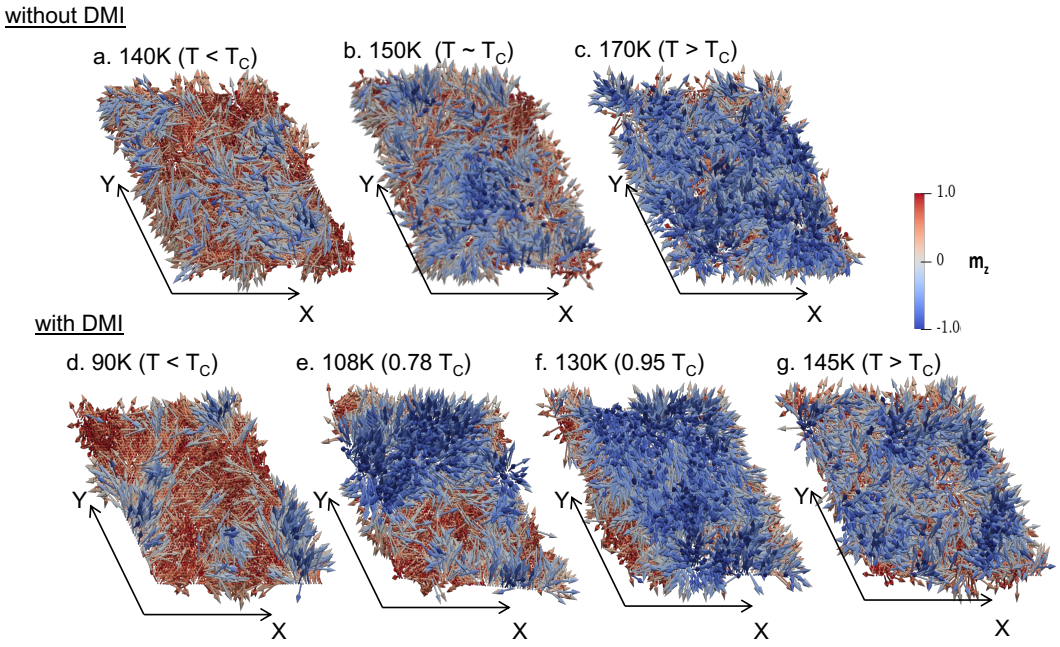

Figure 5.2: Spin vector plots for a range of temperatures from the lattice simulations without DMI a-c and with DMI d-g.

5.1 Metadynamics Analysis of the Magnetisation Reversal

Next, well-tempered metadynamics is applied in both systems with and without DMI with the CV set as the m_z with mirrored boundaries applied to compare their magnetisation reversal transitions and to quantify the associated energy barriers in each case. For all the simulations, the magnetic parameters shown in table 4.1 are used. The metadynamics and simulation parameters are shown in table 5.1

Metadynamics Parameters	
MC Steps	110×10^6
Gaussian Deposition stride	$\tau_g = 5$
Gaussian Amplitude	$\omega = 0.01meV$
Gaussian Width	$\sigma = 0.05$
Bias Temperature	$\Delta T = 1000K$

Table 5.1: Well-tempered metadynamics simulation parameters for the magnetisation reversal simulations with and without DMI using the out-of-plane magnetisation as a CV with the mirrored boundaries.

5.1.1 Lattice without DMI

Starting with the lattice without DMI, the same FEL as seen in section 3 is observed with two energy minima at the thermodynamic magnetisation for the temperature of the simulation. For every temperature, 10 individual simulations are run. Figure 5.3 shows the set of the individual simulations for the 50K and 100K simulations, and the standard errors of these simulations are shown in figure 5.4. As can be seen, the reconstructed FEL of each simulation converges almost perfectly with the others. It is worth noting that for intermediate temperatures, the standard error from the 10 individual simulations is reduced due to the more frequent crossing of the energy barrier. Finally, the calculated energy barriers are plotted in figure 5.5, with the energy barrier reducing with increasing temperatures. Additionally, it can be clearly seen that for lower temperatures, the errors are higher due to the less frequent crossing of the energy

barrier.

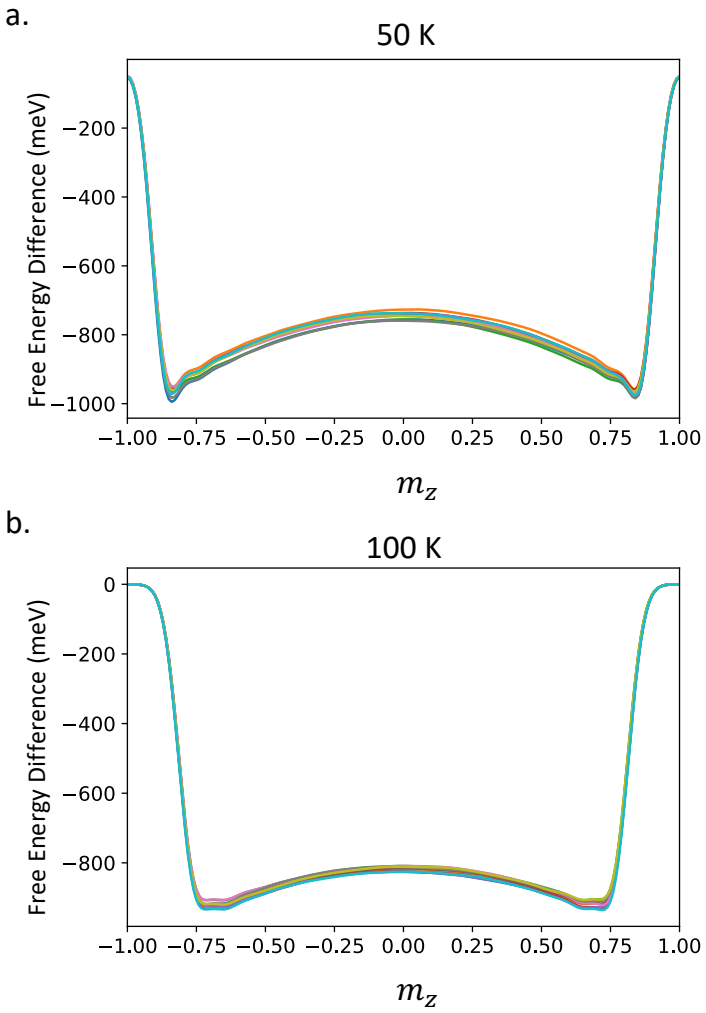

Figure 5.3: Set of the 10 independent well-tempered simulations for a. 50K and b. 100K showing the convergence of the FELs.

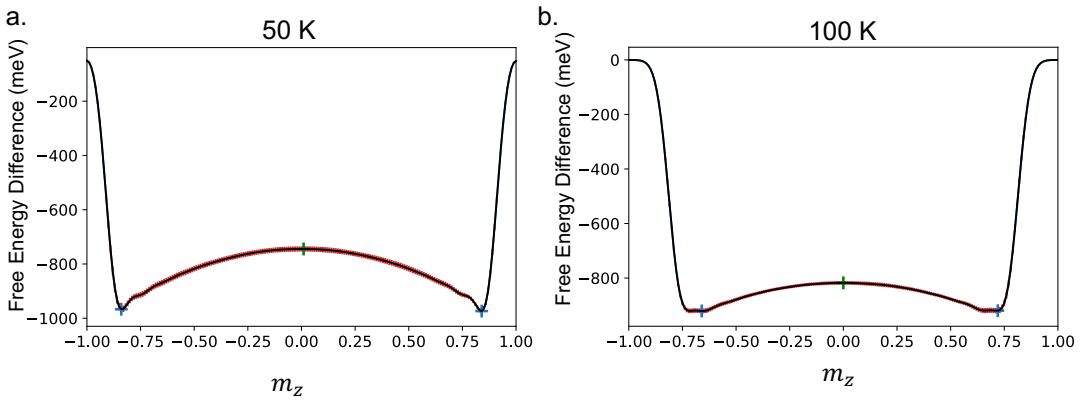

Figure 5.4: Standard error calculation shown as the red area along the FEL. The blue and green crosses show the maximum and minimum energy points used to calculate the associated energy barriers.

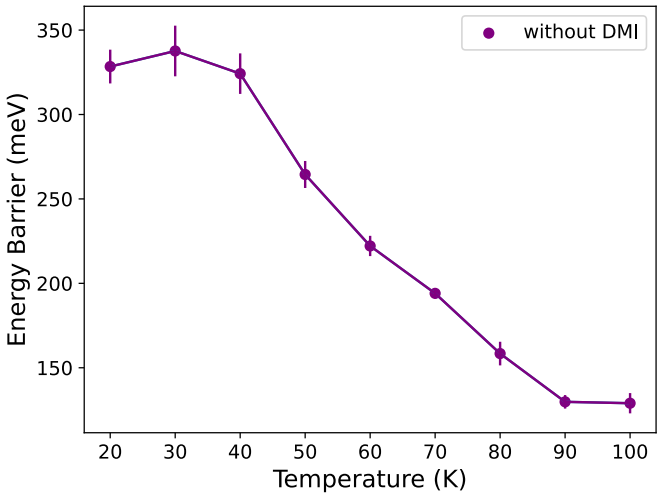

Figure 5.5: Plot of the calculated energy barriers (meV) scaling with increasing temperature (K) from 20K to 100K with their associated error for the lattice without DMI.

5.1.2 Lattice with DMI

Next well-tempered metadynamics simulations were conducted in the same system with DMI strength of $0.811\mathrm{meV}$ with the same simulation parameters as shown in tables 5.1. Figure 5.6 show the independent simulations for temperatures of a. 50K, b. 60K, c. 80K and d.90K. Compared to the lattice without DMI, these FELs have two energy minima that the system needs to overcome to reverse the magnetisation. These energy barriers are named first and second energy barriers, as shown in figures 5.6 and 5.7. As reported in chapter 4, this is due to the formation of a chiral domain because of the DMI present. As the temperature increases, systematic errors are introduced along the FELs, as shown in figure 5.6 b-d. This is due to the chiral texture formations observed in the plain monte carlo simulations as shown in the vector plot figure 5.2 and the susceptibility plot 5.1 a. where the noise prior to the T_{c} is due to the DMI present thus as it can be seen on figure 5.7 the standard error along the FEL increase due to these random chiral texture formations.

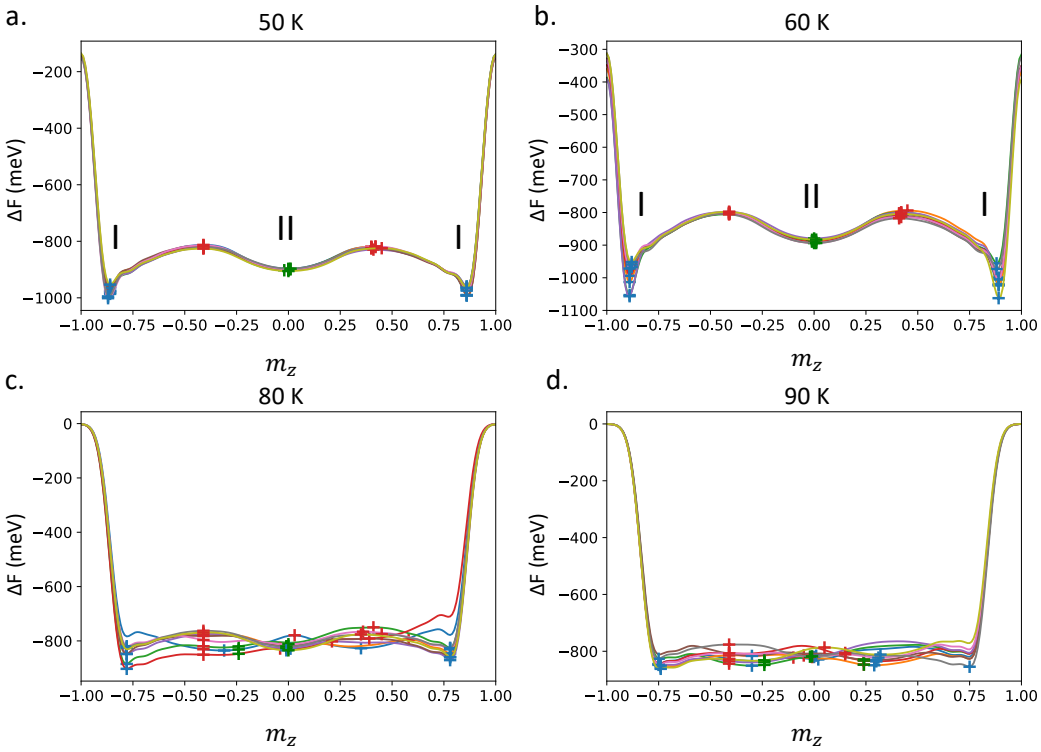

Figure 5.6: Set of the 10 independent well-tempered simulations in the lattice with DMI for a. 50K, b. 60K, c. 80K, and d.90K showing the convergence of the FELs.

The energy barriers height (meV) for both minima are plotted in figure 5.8, for the first energy minima is calculated as the average between the two minima at $\pm m_z\,(\mathrm{T})$ shown as blue data points in figure 5.8. The second energy minimum is a metastable state between the two groundstates (first energy minima). The height of the second energy barrier is plotted with the orange data points. For both energy minima, the errors progressively increase for temperatures higher than 30K, as explained.

Comparing the energy barriers for the simulations with and without DMI, it can be seen that the energy barrier to reverse the magnetisation is higher for the system without the DMI. The comparison between the two sets of simulations is plotted in figure 5.9. The plotted energy barrier height for the simulations with DMI includes the energies from both energy barriers. In low temperatures (20K), the energy barrier to reverse the magnetisation for the system with

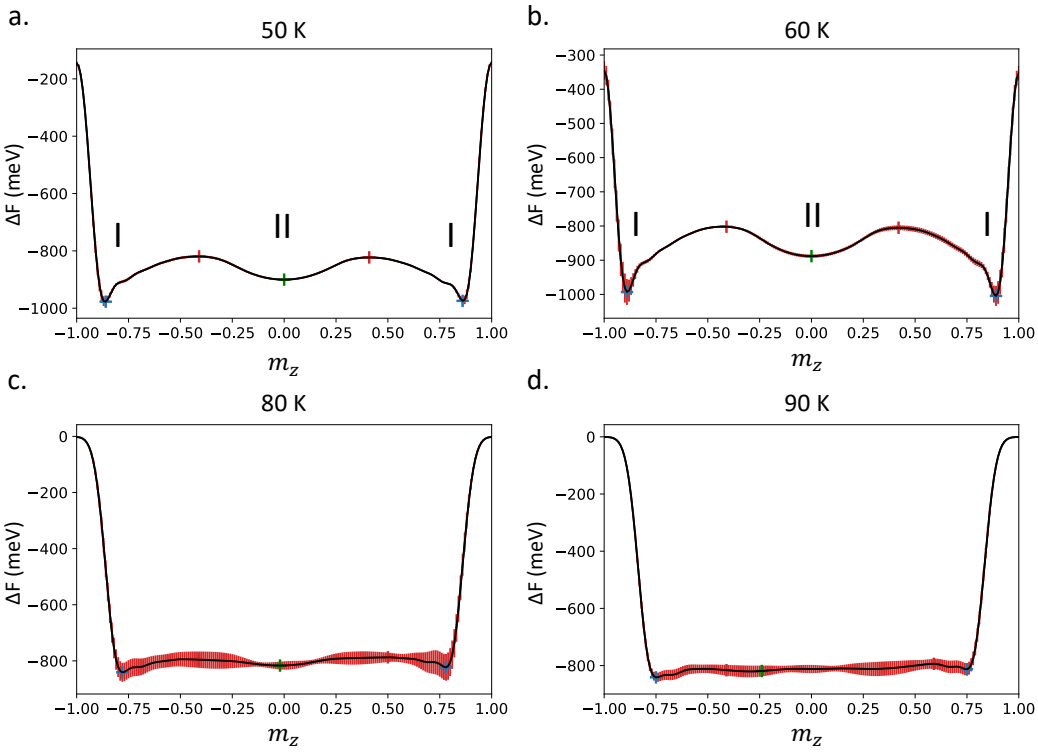

Figure 5.7: Standard error calculation shown as the red area along the FEL for the well-tempered simulation simulations with DMI. The blue and green crosses show the minima energy points, and the red crosses show the maxima point between the energy minima used to calculate the associated energy barriers.

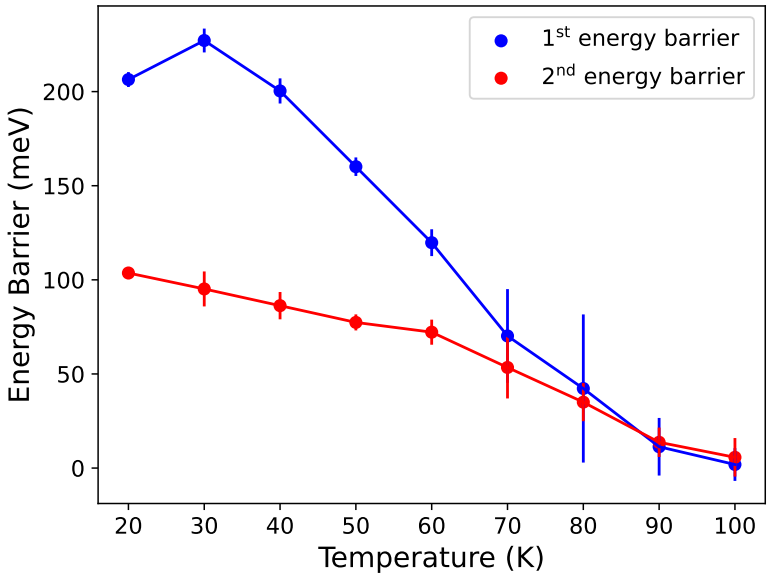

Figure 5.8: First (blue) and second (orange) energy barrier heights (meV) as a function of increasing temperature (K)

or without DMI is similar. This is because, for low temperatures, the thermal fluctuations are smaller, and all spins are in the $+m_z$ directions. As the temperature is increased, the thermal fluctuations start to spontaneously reverse some of the spins in the $-m_z$ direction. Thus as shown in this section, for the system with DMI, the spins crossed due to thermal fluctuations cluster together. This reduces the energy required to reverse the magnetisation since it reduces the energy required to overcome the second energy barrier. As the temperature increased, the difference between the two systems became stronger, as expected.

Moreover, there is another important conclusion that this study suggests about the behaviour of thin films. More specifically, in thin films, as the dimensions are reduced, the demagnetisation field becomes weaker. In turn, this induces single magnetic domain thin films. Thus it is often believed that the magnetisation reversal occurs with a coherent rotation. As this study has shown, this is true in thin films without DMI. However, in single-domain thin film heterostructures with strong DMI, the magnetisation reversal occurs by the creation and expansion of a chiral domain which is energetically more favourable, especially for higher temperatures, as

the findings of this study suggest.

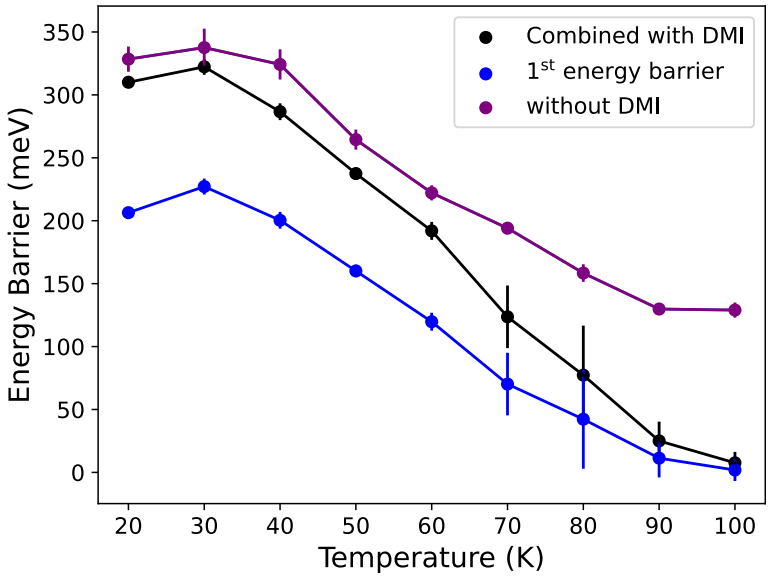

Figure 5.9: Comparison between the energy barriers height scaling with temperature for the simulations with and without DMI with their associated standard errors. For the system with DMI, first, the combined energy barriers are plotted. However, since, the energy to revert the magnetisation will always occur when the dominant energy barrier energy exceeds the most dominant (first) energy barrier is plotted too.

CHAPTER 6

Towards Skyrmion Lifetime Calculations

Currently, most computational skyrmion stabilities studies [2, 3, 54] are using the GNEBM to identify the skyrmion metastable energy and use an arbitrary attempt frequency to estimate the skyrmion lifetime using the Néel type Arrhenius equation. However, the GNEBM energy barrier, ΔE includes only the internal energy contributions, and the attempt frequency, τ_0 has been shown experimentally that it changes over 30 orders at finite temperatures [82]. In contrast, in chapter 4, the energy barriers extracted using metadynamics, ΔF include both the internal energy and entropic contributions, shown to be a major factor on skyrmions stability [4].

Using metadynamics, it is possible accurately estimate the attempt frequency, τ_0 in finite temperatures. With metadynamics, the skyrmion metastable energy at a high temperature which results in an estimated lifetime of a few hundred nanoseconds can be identified (using the arbitrary $\tau_0 = 1GHz$). This will allow to simulate a lattice with a skyrmion at that temperature and identify the lifetime of the skyrmion before its annihilated. Since the expected lifetime will be within the timescale range where the atomistic framework can simulate by evolving the system using the Landau-Lifshitz-Gilbert (LLG) equation [108]. Thus the attempt frequency can be calculated as,

$$\tau_0 = \tau \exp\left(\frac{\Delta F}{k_{\mathrm{B}} T}\right) \tag{6.1}$$

In practice, this requires stopping the atomistic simulations immediately when the skyrmion is annihilated and having a thermalised lattice with a skyrmion. However, the conventional ways that a skyrmion is inserted in a spin-lattice require a relaxation process, where often the skyrmion is annihilated before getting stable at high temperatures. Similarly, during the simulation, Q need to be monitored to stop the simulation once the skyrmion is annihilated. But both topological charge definitions have limitations which can lead to the simulation stopping before the skyrmion is annihilated or continuing running due to the inaccurate calculation of Q. These two problems can be resolved by using metadynamics and combining both definitions of topological charge.

In this chapter, first, the conventional ways to stabilise a skyrmion in a lattice are introduced. Then the procedure to generate a thermalised lattice with metadynamics and by com-

bining the two definitions of topological charge is presented.

6.1 Stabilising a Skyrmion in a Lattice

As discussed in chapter 2, a pre-defined lattice is used to initiate a simulation, which is then thermalised, resulting in the final spin configuration as a consequence of the interacting terms in the Hamiltonian. Throughout this thesis, the Hamiltonian terms selected are the Heisenberg exchange, magnetocrystaline anisotropy, DMI and Zeeman terms with units of Joules, as shown in equation 2.1. To stabilise a skyrmionic spin texture is important to select the appropriate strength for J_{ij}, K_{u}, and D_{ij}. The interplay between these energy term strengths dictates the stability and size of the resulting interfacial skyrmion. Increasing the D_{ij} results in larger skyrmion radii, which, if it's too strong, will result in chiral domain walls as opposed to K_{u} which act to shrink the skyrmion radii, which eventually results in the skyrmion annihilation. In literature, sub-ten nanometer skyrmions are stabilised using the following ratios

$$\frac{D_{\mathrm{ij}}}{J_{\mathrm{ij}}} = 0.36, \quad \frac{K_{\mathrm{u}}}{J\mathrm{ij}} = 0.4. \tag{6.2}$$

The predefined lattices incorporated are a simple cubic lattice and a hexagonal lattice (i.e. FCC(111) interface), which are common interfacial crystal structures of the thin films that experimentally reported the observation of skyrmions. These crystal lattices are shown in figure 6.1. For both crystal lattices used, the unit vector in the magnetocrystaline anisotropy term, $\hat{\mathbf{e}} = (0, 0, 1)$ is set with an out-of-plane easy axis since the systems simulated are thin films.

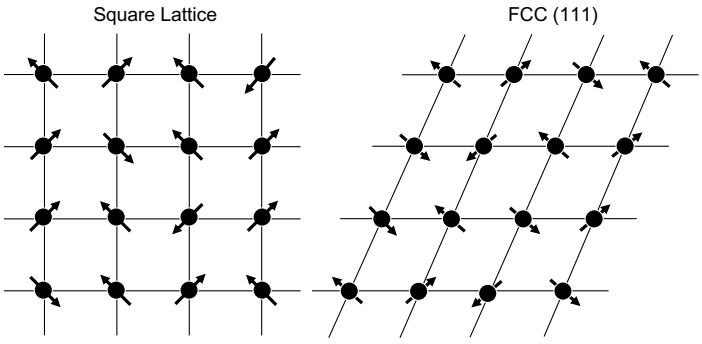

Figure 6.1: Illustration of a square and a hexagonal lattice

To include a skyrmion within a lattice, the simulation is initialised with one of the following two conventional ways. First, with a uniform ferromagnetic state along the positive or negative m_z with a radius of spins in the opposite m_z as shown in figure 6.2 a. Secondly, using an expression for a static skyrmion profile according to

$$\tan\left(\frac{\Theta_0\,(\mathrm{r})}{2}\right) = \frac{r_s}{r} \Rightarrow \Theta_0\,(r) = 2\arctan\left(\frac{r_{sk}}{r}\right) + 2\pi \tag{6.3}$$

where $\Theta_0\,(\mathrm{r})$ is the skyrmion profile in polar coordinates r

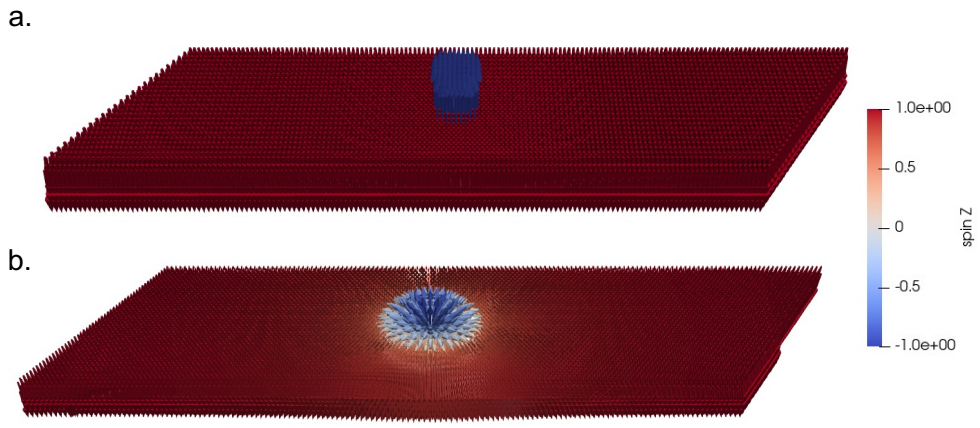

Figure 6.2: Predefined atomic lattices of an fcc(111) Fe/Pt multilayer nanowire with uniform ferromagnetic spins with radii of spins a. uniformly arranged in the negative m_z and b. with a skyrmion profile calculate by equation 6.3

By relaxing the spin configurations shown in figure 6.2, a stable skyrmion in finite temperature is stabilised if the magnetic term strengths are selected correctly. The difference between the two initialisation techniques is that the skyrmion profile requires less MCS to stabilise the skyrmion. However, the ground state of any thin film with out-of-plane is a ferromagnetic state, not a skyrmionic one. Hence, there is always a finite probability for the skyrmion to annihilate as more MCS are performed. Additionally, in higher temperatures relative to the system's Curie temperature, the skyrmion can get annihilated during the thermalisation of the lattice before it gets stabilised. This is due to thermal noise, which can cause the spins close

to the external skyrmion circumference to flip to the opposite side, which can shrink and annihilate the skyrmion or expand the skyrmion get annihilated in the boundaries of the lattice in a finite lattice. This can be a major limitation when testing magnetic energy term parameters or incorporating dynamical simulations.

6.2 Thermalised Skyrmion Lattice with Metadynamics

As introduced in 6.1, for temperatures near the T_{C}, skyrmions can be annihilated before the lattice is fully thermalised after a few hundred MC steps. This can happen both when a skyrmion is initialised by reverting the spins within a radius, or when a full skyrmion profile is introduced into the ferromagnetic texture. This is also seen in figure 4.11, where the skyrmion at 84K got annihilated before the lattice was thermalised. It is possible that before the lattice is thermalised, the effect of the ΔS contributing to the skyrmion stability is not strong, increasing the probability of the skyrmion getting annihilated during the thermalisation process. Thus for any thermal stability studies with any spin texture, it is crucial that a thermalised lattice with the spin texture of interest is used as the initial spin configuration. Thus here, a procedure with metadynamics is reported, which can be used to generate a thermalised lattice for the continuation of this project or any other study which requires a thermalised lattice with a spin texture at temperatures near the T_{C}.

In section 4.1.2, two procedures that can be used to calculate the topological charge were introduced. By using both of these procedures to monitor the lattice Q during the simulation, the simulation can be terminated when metadynamics generates a skyrmion at finite temperatures. At the same time, this can be used as a monitor to stop the simulation as soon as the skyrmion is annihilated to find the lifetime of a skyrmion using atomistic simulations evolved with the LLG. Hence, by outputting the spin configurations when metadynamics has generated a skyrmion, a thermalised lattice with a skyrmion can be generated.

The geometrical definition of the topological charge calculates only integer values of Q. However, single spins can result in a topological of ± 1 even if a skyrmion is not generated in the lattice. On the other hand, the finite difference calculation of the topological charge considers

the whole lattice spin configurations; thus, in high temperatures, the thermal fluctuations offset the calculation of Q. Thus by monitoring the metadynamics simulation with both definitions of topological charge, the simulation can be terminated when both calculations result in $Q = \pm 1$. To demonstrate this, plain metadynamics is used in the same lattice, with the same magnetic parameters as in the previous subsection 4.3. However, a large Gaussian amplitude, $w = 5$ meV, is used since the aim is to use metadynamics to generate a skyrmion at finite temperatures, not reconstructing the FEL. As in subsection 4.3, the finite difference topological charge and m_z are used as CVs. For the m_z CV, the mirror boundaries are used. Similarly, for the Q CV, the restoring boundaries are used to limit the exploration of topological charge configurational space from $Q = -1.4$ to $Q = 1.4$. Figure 6.3 a. shows the topological charge estimations using both procedures during the metadynamics simulation to generate a single skyrmion at 40K. Figure 6.3 a.i shows a single spin which results in the geometrical definition calculation of $Q = +1$ even if a skyrmion is not generated within the lattice. However, figure 6.3 a.ii demonstrates that when both definitions of topological charge calculations are $Q = \pm 1$ a skyrmion has been generated, which at that point, the simulation can be terminated. Similarly, figure 6.3 b. shows the effect of the thermal fluctuations in the calculation of Q using the finite difference definition. Figure 6.3 b.i shows that it is probable that the thermal fluctuations can monumentally form a spin configuration which results in $Q \approx \pm 1$. However, when both definitions of Q result is $Q = \pm 1$, a skyrmion is again generated within the lattice. Additionally, even if restoring boundaries are used to limit the number of skyrmions in only one, figure 6.3 shows that the geometrical definition often suggests that there are two skyrmions in the lattice; since it only returns integer values of topological charge.

Figure 6.4 shows a range of temperatures in which the metadynamics simulation was monitored using both the definitions of Q. It clearly shows that with increasing temperature, the fluctuation of the calculation of Q using the finite difference definition increases and becomes limiting for temperatures near the T_C. This is also the main reason that in section 4.3, the range used to reconstruct the FEL was limited to 54K. Furthermore, figure 6.4 also demonstrates the fact that metadynamics explores the whole configurational space faster for elevated temperatures. This is due to the larger thermal fluctuations, which increase the probability of the CV

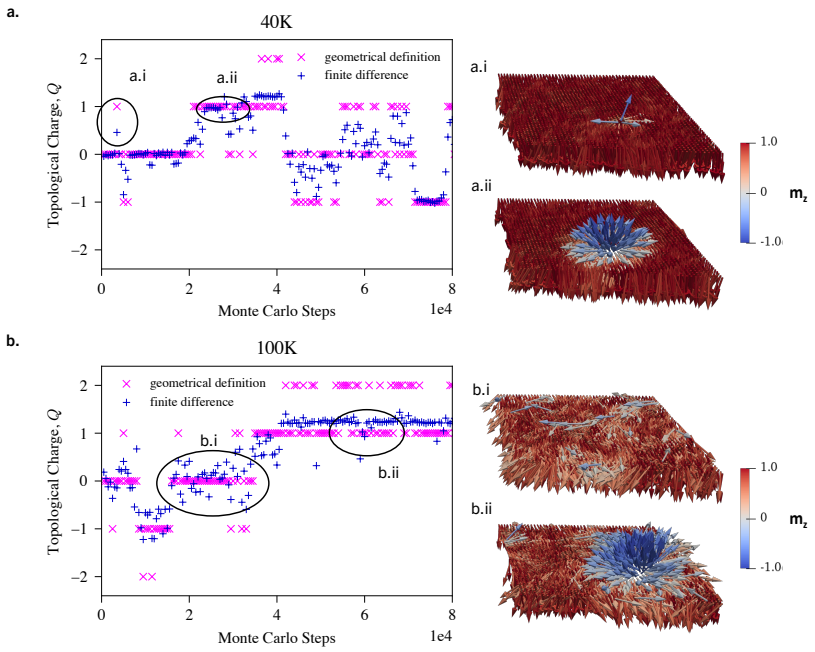

Figure 6.3: Calculations of the topological charge using the geometrical definition and finite difference paradigms for a. 20K and b. 100K. The vector plots a.i and a.ii show the limitation of the geometrical definition calculation. Similary b.i and b.ii demonstrate the limitation of the finite difference topological charge calculations with increasing temperatures

escaping a partially filled energy minimum region.

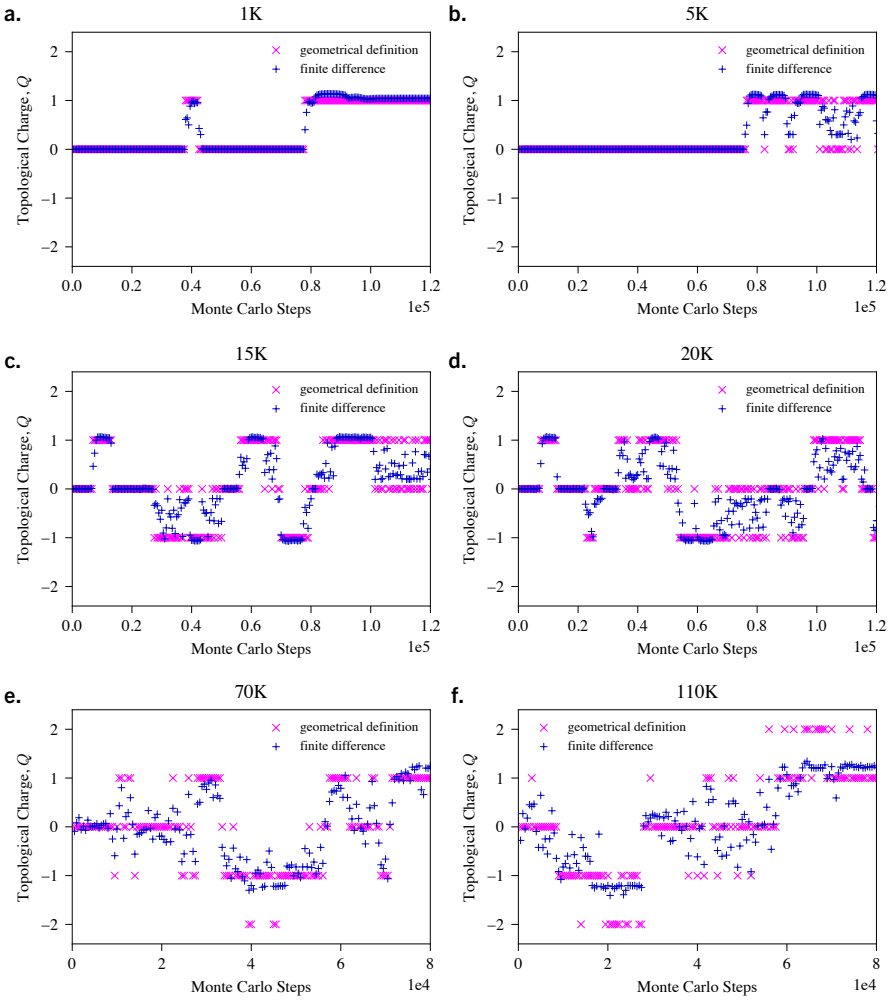

Figure 6.4: Geometrical definition and finite difference calculations of the topological charge for a range of temperatures demonstrating the limitation of both topological charge calculations.

6.3 Conclusions

As discussed in this chapter, the skyrmion lifetime can be estimated using a more accurate attempt frequency τ_0 (without an assumed value) and the more accurate metastable skyrmion energy, including the contributions of both the ΔE and ΔS using metadynamics. As extensively described in this chapter τ_0 can be calculated at elevated temperatures with the following steps:

1. Estimating the temperature where the skyrmion lifetime is within the time range where atomistic simulations can simulate the system. This can be achieved by using metadynamics to calculate the ΔF as demonstrated in chapter 4 and using the Néel type Arrhenius with the assumed $\tau_0 = 1\text{GHz}$.

2. For the temperature identified, creating a thermalised skyrmion lattice using metadynamics as shown in section 6.2.

3. The skyrmion lifetime can be calculated; using the lattice with the thermalised skyrmion and evolving the system using the LLG equation while monitoring the system with both topological charge definitions.

4. Calculating the attempt τ_0 using the Néel type Arrhenius equation 6.1

By identifying the τ_0 for a range of temperatures, a more accurate estimation or more justified selection of τ_0 can be used for lower temperatures where the skyrmion lifetimes are larger than the atomistic formalism time range limits.

To conclude, the skyrmion lifetime calculations and the calculation of the attempt frequency can be achieved by combining the topological charge definitions; by using metadynamics, the simulation can be stopped as soon as a skyrmion is created from metadynamics in the lattice. Then this lattice can be used as a starting lattice for any thermal study of skyrmions at high temperatures, ensuring that the thermalised lattice includes a stable skyrmion. Similarly, the combination of the topological charge definitions can be used to stop an atomistic simulation evolved with the LLG as soon as the skyrmion is annihilated at finite temperatures.

Here, the interest is to calculate the skyrmion lifetime. However, this procedure can be applied to more studies within or outside of the scope of this thesis, highlighting that metadynamics is powerful for atomistic and micromagnetic simulations, which possibilities have not yet been explored.

CHAPTER 7

Further Work

7.1 Effects of Lattice Defects

The natural continuation of this project is to include lattice defects. Then by selecting the appropriate CVs, the effect of a single or a set of defects can be studied. This can be achieved using the skyrmion core centre as a CV to move the skyrmion around the lattice. Possible energy minima in the reconstructed FEL will indicate that the skyrmion is pinned at that point and maxima that are deflected. If the Q and m_z with the skyrmion core centre are used as CVs, then the creational and annihilation skyrmion energies can be identified and studied as a function of temperature.

If non-magnetic defects such as impurities and vacancies are wished to be studied, then the DMI vectors within the lattice will not be uniform since the symmetry of the lattice will be broken. Thus a generalised and efficient procedure to calculate the DMI vectors at each lattice point must first be developed. If magnetic impurities are studied, then the DMI vectors need to be recalculated throughout the lattice with the addition that the magnetic impurities will affect exchange and anisotropy energies. The changes in anisotropy and exchange can be identified using first principle ab-initio calculations or from experimental data. Another difficulty will be to ensure that the skyrmion is not annihilated during the metadynamics simulation. This is because as metadynamics build the potential used to bias the skyrmion core centre, it is possible that it will exceed the skyrmion metastable energy, thus annihilating the skyrmion.

However, these studies will be crucial for the design and realisation of future skyrmionic devices. With a better understanding of the lattice defects, it is possible to engineer devices where specific defects are used to pin, deflect, lower or increase the energy required to create a skyrmion. Currently, there are many reports on the effects of defects in skyrmion motion and dynamics [3, 45, 55]. However, as is demonstrated, the metadynamics procedures developed in this thesis are currently the only method that fully accounts for temperature effects and includes both the contributions of the skyrmion internal and entropic energies in the estimations of the energy barriers studied as well as sampling all possible transitions between states. Thus in subsections 7.1.2, 7.1.3 and 7.1.4, the calculation of the skyrmion core centre and its use as a CV is demonstrated while reporting ways to ensure that the skyrmion will not get annihilated

during future simulations with defects, are introduced and discussed.

7.1.1 Skyrmion Core Center

The CVs that must be used to describe the skyrmion core centre fully are the X and Y cartesian coordinates. This also offers the benefit of moving the skyrmion only horizontally and vertically by using only one of these CVs. As previous studies reported that skyrmions' annihilation is preferable at the top or bottom edges in nanowires [2, 3], by using the y coordinate with the m_z and Q as CVs, these studies can be verified and show all possible annihilation paths and how these scale with temperature.

Thus, the configurational space for the set of CVs describing the skyrmion core centre is the physical space of the lattice simulated along the X and Y cartesian coordinates. As shown later, these CVs push the skyrmion to explore and sample the whole lattice. In plain MC, if the proposed S_{trial} is within the skyrmion radius or near the circumference, the highest probability is S_{trial} will not get accepted if the angle between S_{i} and S_{trial} is large, for temperatures were the thermal fluctuations are too small compared to the skyrmion metastable energy barrier. However, metadynamics will build a potential that will eventually be more energetically favourable to accept spins that change the skyrmion core centre. Hence the skyrmion will start exploring the whole lattice in regions with smaller V_{bias}.

In a system without any lattice defects, the underlined FEL is expected to be flat or not show any large energy basins. Additionally, the ability to use these CVs is crucial for the continuation of this project. Additionally, as discussed later, we show that tempered metadynamics can be used to ensure that the skyrmion will not get annihilated due to metadynamics.

7.1.2 Calculation of the Skyrmion-Core Center

In a system without any lattice defects, the underlined FEL is expected to be flat or not show any large minima. Additionally, as discussed later, we show that tempered metadynamics can be used to ensure that the skyrmion will not get annihilated due to metadynamics.

To use the skyrmion core centre as a CV, a computationally efficient and accurate method of calculating the skyrmion core centre must be used. Within a skyrmion, the spins are in

the opposite direction with respect to the rest of the lattice. Hence, the conventional weighted centre of mass can be used to calculate the skyrmion centre of mass coordinates **C** by setting the weight of each spin according to its magnetisation direction along the z-direction where if $m_z \geq -0.05$ the weight is set as 0 to ensure that only spins within or near the skyrmion contribute to the calculation of the skyrmion centre of mass according to

$$\mathbf{C} = \frac{1}{\sum_{i=1}^{n} (S_{z,i})} \sum_{i=1}^{n} (S_{z_i} \mathbf{r}_i) \tag{7.1}$$

where n is the number of spins below the threshold set and $\mathbf{r}_i$ are the cartesian coordinates of $\mathbf{S}_i$. However, this method is inaccurate for lattices with periodic boundary conditions since the spins within a skyrmion can be across the other side of the lattice, which offsets the calculation of the skyrmion core centre, when equation 7.1 is used. This is demonstrated in figure 7.1 b. where a skyrmion centre of mass is calculated incorrectly while the skyrmion is at the corner boundaries. Additionally, suppose the calculation of the skyrmion core centre is offset

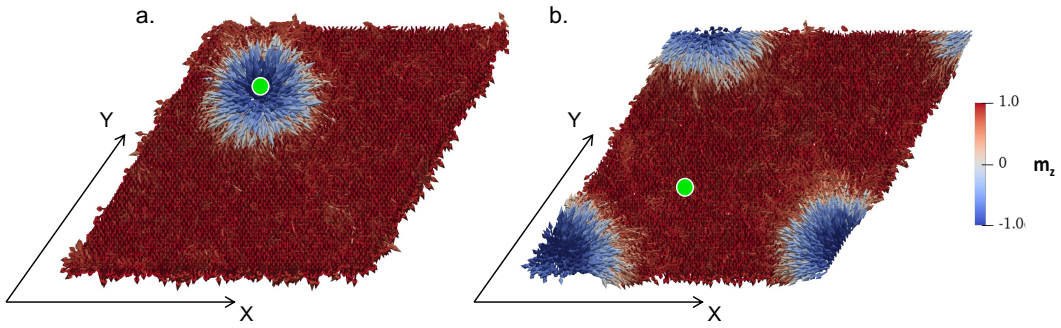

Figure 7.1: Skyrmion centre of mass calculation indicated with the green dot at a. away from the boundaries and b. at the corner boundaries of an fcc(111) lattice with periodic boundary conditions applied along the x and y directions

during the metadynamics simulation. In that case, the Gaussians may be deposited around the skyrmion, which can effectively restrict the skyrmion from exploring the lattice. This is illustrated as a one-dimensional example in figure 7.2. In 7.2 a., the Gaussians are deposited centred at the correct value of the skyrmion core centre. Hence eventually, the potential accumulated

will move the skyrmion away from the regions with high potential. On the other hand, in n 7.2 b., the offset skyrmion core calculation accumulates the bias potential around the skyrmion, restricting it from moving around the physical lattice.

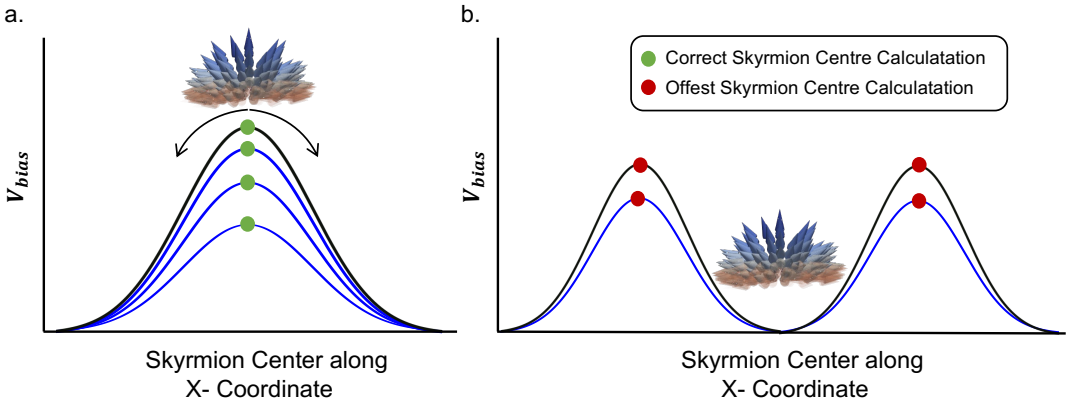

Figure 7.2: a. Illustrates the V_{bias} built centred around the correct skyrmion core centre along the x-coordinate, which will push the skyrmion to move within the x-direction. In contrast, in b., the offset skyrmion centre calculations denoted with the red point create a potential around the skyrmion, which effectively traps the skyrmion.

To overcome the limitations described, the algorithm reported by L.Bai and D.Breen in 2008 was employed [6]. This algorithm calculates the centre of mass for a set of points by forming two perpendicular tubes along the x and y, cartesian coordinates T_i and T_j and calculates their 3D centre of mass $\bar{\mathbf{X}}$. Then, by projecting the tubes' 3D centre of mass into the surface of the tubes and "unfolding" the tubes, the 2D coordinates of the centre of mass, $\left(\bar{i}, \bar{j}\right)$, are calculated.

Here, the point masses are the **S** at the lattice points with cartesian coordinates (i, j). This algorithm can be adapted to calculate the skyrmion centre of mass by only including spins S whose m_z component is lower than a threshold in T_i and T_j. Ensuring that S is orientated in the opposite direction of the ferromagnetic direction; S is within the spin radius). In higher temperatures, spins may cross this threshold due to thermal noise, but their effect is negligible.

The tube T_i connecting the point i with i_{max} of the lattice is formed by transforming the **S** by remapping the cartesian coordinates (i, j) from 2D into 3D where each considered lattice

point k coordinates is transformed to $\mathbf{X}_k \equiv (x, y, z)$ according to

$$x = \frac{i_{\max}}{2\pi}\cos(\theta_i) \quad , \quad y = j \quad , \quad z = \frac{i_{\max}}{2\pi}\sin(\theta_i), \quad \text{where} \quad \theta_i = \frac{i}{i_{\max}}2\pi \tag{7.2}$$

Similarly, the tube T_j connects the point j with $j_{\max}$ is formed with the following transformation

$$x = i \quad , \quad y = \frac{j_{\max}}{2\pi}\cos(\theta_j) \quad , \quad z = \frac{j_{\max}}{2\pi}\sin(\theta_j), \quad \text{where} \quad \theta_j = \frac{j}{j_{max}}2\pi \tag{7.3}$$

Following the remapping of the 2D space into the tubes T_i and T_j, the 3D centre of mass of each tube is calculated as

$$\bar{X} = \frac{1}{n}\sum_{k}^{n} X_k \tag{7.4}$$

where n is the number of points within the tube. The projection of the centre of mass of each tube T_i and T_j gives the coordinates of the 2D centre of mass coordinates $\bar{i}$ and $\bar{j}$, respectively. Thus the $\bar{i}$ coordinate of the centre of mass is calculated from the T_i, 3D centre of mass, $\bar{\mathbf{X}}_i = (\bar{x}, \bar{y}, \bar{z})$ calculated from equation 7.4 and projected with the following expression

$$\bar{i} = \frac{i_{\max}}{2\pi} \cdot \arctan 2\,(-\bar{z}, -\bar{x}) + \pi \tag{7.5}$$

where $\arctan 2\,(-\bar{z}, -\bar{x})$ is the inverse tangent function in the interval $(-\pi, \pi]$ used to map the point at $(-\bar{z}, -\bar{x})$ in the Cartesian plane.Then the $\bar{j}$ coordinate is given from the 3D centre of mass of tube T_j

$$\bar{j} = \frac{j_{\max}}{2\pi} \cdot \arctan 2\,(-\bar{z}, -\bar{y}_i) + \pi \tag{7.6}$$

Equations 7.5 and 7.6, give the skyrmion core centre coordinates $\left(\bar{i}, \bar{j}\right)$ which can also be used as single CVs by using only $\bar{i}$ or $\bar{j}$. However, the computation of the $\arctan 2$ function and space remapping of the lattice points is computationally expensive and can limit the use of the algorithm as a CV. However, by using the caching system introduced in section **??**, the space remapping of the lattice points in the tubes T_i and T_j is only required in the initialisation of the simulation. Then every time a $\mathbf{S}_{\text{trial}}$ with the m_z component is lower than the threshold set, the tube is updated, and the centre of mass is recalculated. This procedure is illustrated in a 1-dimensional example figure 7.3, wherein a. it shows a skyrmion profile with the center pointing at $m_z = -1$. The skyrmion profile is split across the boundaries. Then the 1D line

is folded into a circle, with the points transformed from 1D to 2D. The circle formed is shown in figure 7.3 b, where only the spins within the skyrmionic profile are included, and the 2D centre of mass calculated is shown as the red cross within the circle. Then in figure 7.3 c, the calculated 2D centre of mass is projected on the surface of the circle shown as the green point. The projected 2D centre of mass provides the 1D centre of mass of the 1D environment as shown in figure 7.3 d.

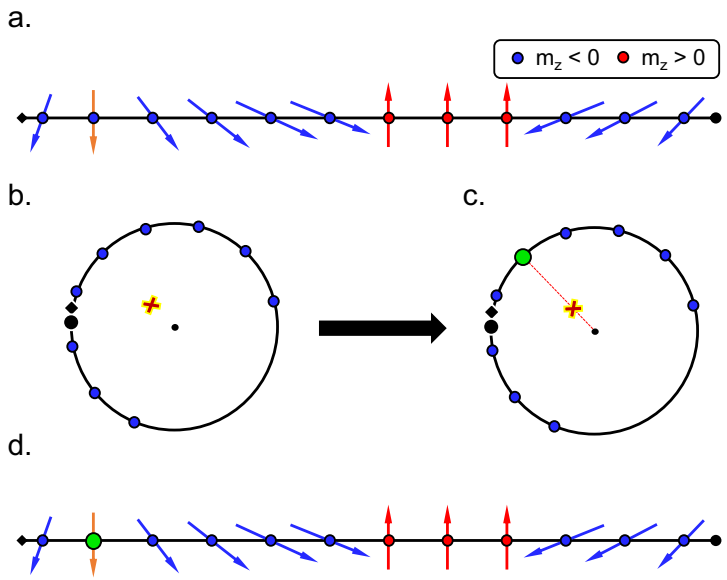

Figure 7.3: Schematic illustration of the centre of mass calculation in 2D as shown by L.Bai and D. Green [6] adapted to calculate the skyrmion core centre where the blue and red arrows represent spins pointing in the negative and positive z-direction respectively. Part a. shows the skyrmion profile across the periodic boundary conditions. b. and c. show the algorithm procedure where the red sign indicates the centre of mass of the circle, which is then projected into the surface of the indicated with the green point.

7.1.3 Lattice with Periodic Boundary Conditions

The skyrmion core coordinates along the x and y coordinates are selected as CVs to move the skyrmion along a uniform lattice without any periodic boundaries. The results reported here

were conducted at 40K. An fcc(111) multilayer with lattice dimensions of $64 \times 64 \times 5$ with a skyrmion with radius $r_{sk} = 10$ atomic lattices was initiated as a skyrmion profile. Periodic boundary conditions were used along the x and y axes. The metadynamics parameters used are reported in the table 7.1

Metadynamics Parameters	
MC Steps	6×10^6
Gaussian Deposition stride	$\tau_g = 100$
Gaussian Amplitude	$w = 0.5 \times 10^{-28}\text{meV}$
Gaussian Width	$\sigma = 5$
Bias Temperature	$\Delta T = 480\text{K}$

Table 7.1: Metadynamics simulation parameters for the plain metadynamics simulations in a hexagonal $64 \times 64 \times 5$ hexagonal lattice with periodic boundary conditions applied along the x and y coordinates.

The low ΔT ensures that the V_{bias} will not exceed the skyrmion's metastable energy, thus ensuring that the skyrmion won't exceed its metastable energy. Moreover, a fast τ_g can create small local minima, which can locally trap the skyrmion, which slows down the sampling of the whole physical lattice. This rarely occurs, but with a higher deposition stride, the probability of this occurring is reduced. Moreover, the skyrmion movement within the physical lattice is affected by τ_g. With a slow Gaussian deposition, the skyrmion moves away from the Gaussian deposited before the next Gaussian is deposited, exploring a larger area quicker. In contrast, a fast τ_g creates a retrograde skyrmion motion along the x and y axes within the lattice. Figure 7.4, clearly shows the effect of the τ_g described, where the dashed lines indicate the physical space, which is due to the hexagonal geometry of the lattice.

However, the whole physical lattice will eventually be sampled if the skyrmion is not annihilated. This can be ensured by maintaining a low energy deposition rate by, which can be controlled by reducing the Gaussian amplitude τ_g or using a lower bias temperature ΔT.

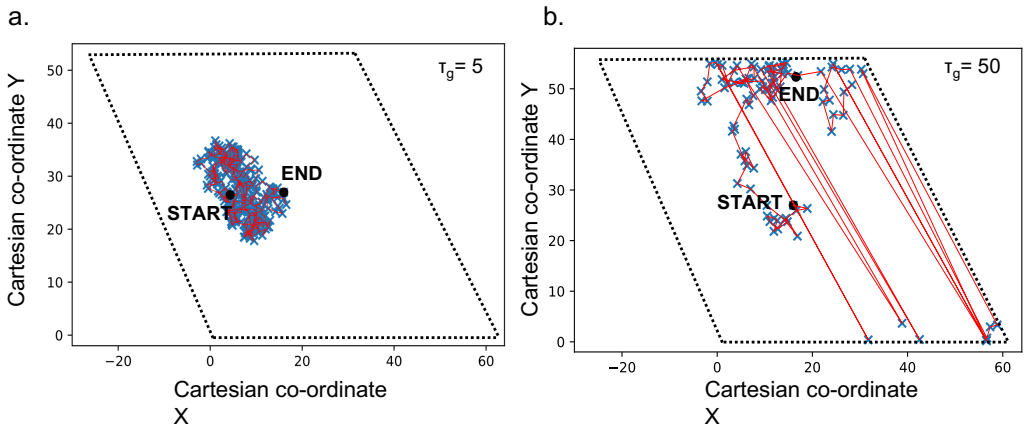

Figure 7.4: Comparing two different τ_g for 6 million MCS and simulation parameters as in table 7.1

Figure 7.5 shows the exploration of the skyrmion core centre after 20×10^6 MCS. It is clearly shown that in the long time limit, the CVs configurationally space is sampled, evident from the location of the skyrmion core centre within the physical lattice. Similarly, in figure 7.6, the skyrmion core location in the initialisation and end of the simulation is shown in the vector plots a. and d. respectively. Hence figure 7.6 demonstrated that metadynamics had not destroyed the skyrmion structure during the simulation. Additionally, by comparing the tracked skyrmion core centre from figure 7.5 with 7.6, the accuracy of the CV calculation across the boundaries is ensured.

To conclude, using the algorithm described by L.Bai in 2009 the skyrmion core centre is successfully used as a CV which results in the skyrmion exploring the physical lattice with periodic boundary conditions along the x and y dimensions. The reconstructed FEL is expected to be flat here, and as shown in figure 7.7, the reconstructed FEL has only shallow features due to the short duration of 6×10^6 MCS. There is no energy minima or maxima present. However, if defects are introduced, the FEL will not be flat, and the features of the FEL can quantify if certain defects pin or deflect skyrmions.

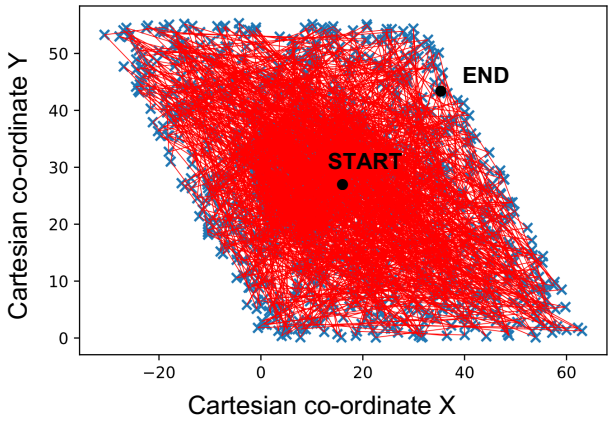

Figure 7.5: Tracking the skyrmion core centre during the metadynamics simulation with the skyrmion core centre set as CV in a lattice with periodic boundary conditions applied along the x and y cartesian coordinates

7.1.4 Confined Lattice

Having examined the centre of skyrmion as a CV in an infinite superlattice of the hexagonal multilayer with periodic boundary conditions applied on x and y axis, a confined lattice without any periodic boundary conditions was considered with the same parameters as reported in table 7.1. It is crucial that the continuation of this project by including lattice defects is simulated in a fully or partially confined lattice. This is because this will allow the simulations of nanowires, and the effects of lattice confined upon the skyrmion stability can be studied. More importantly, in a confined lattice, it is ensured that the skyrmion will move around the defects and not get stuck at the boundaries of the lattice.

However, metadynamics will build a potential in order to move the skyrmion core centre along the physical lattice; to sample the CV's configurational space. Eventually, the potential built will exceed the energy that stabilises the skyrmion in order to move the skyrmion core centre at the boundaries of the lattice, which will result in the skyrmion getting annihilated.

This is shown in figure 7.8, a vector plot with snapshots during the metadynamics simulation at 40K. In figure 7.8 a. and b. metadynamics moves the skyrmion core centre near the boundaries. Eventually, the potential built will result in the spins around the outer circum-

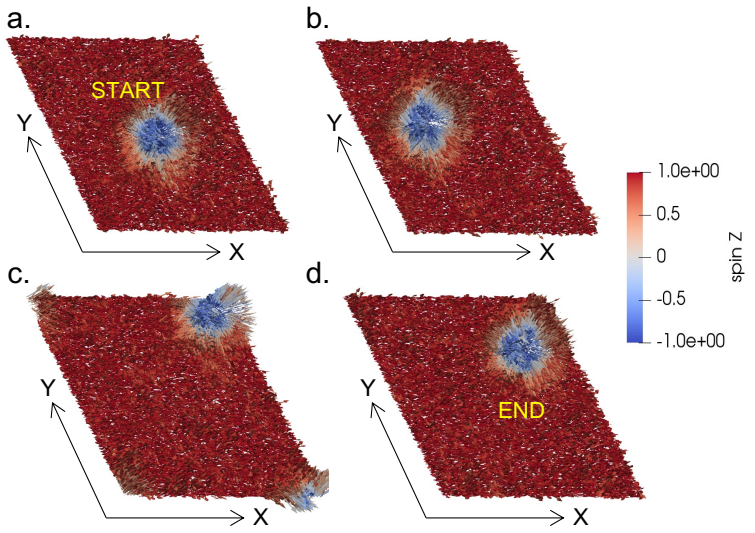

Figure 7.6: Vector plots of four different points during the simulation.

ference of the skyrmion structure being at the boundary of the physical lattice as shown in figure 7.8 c. At that point, the spins within the skyrmion do not map the whole unit sphere, eliminating any skyrmion stability. Hence the skyrmion is annihilated at the boundary, and the ferromagnetic ground state of the system is recovered as shown on snapshots d-f in figure 7.8.

Thus it is important to quantify the skyrmion metastable energy at a finite temperature for a finite lattice prior to the simulation as this thesis demonstrated in section 4. Once the metastable energy is known, a large repulsive potential can be applied around the physical lattice boundaries as illustrated in figure 7.9. By doing so, the reconstructed FEL of finite size with defects can be reconstructed without annihilating the skyrmion at the system's boundaries. Additionally, the potential built next to the introduced repulsive potential will be able to be used to examine if the skyrmion would have been annihilated at the system's boundaries. Another possibility is to use the tempering to introduce a maximum potential deposited throughout the lattice. However, this will depend on the size of the skyrmion metastable energy at a given temperature. This is because it is possible for certain systems that the metastable energy is lower than the energy required to move the skyrmion near the lattice defects.

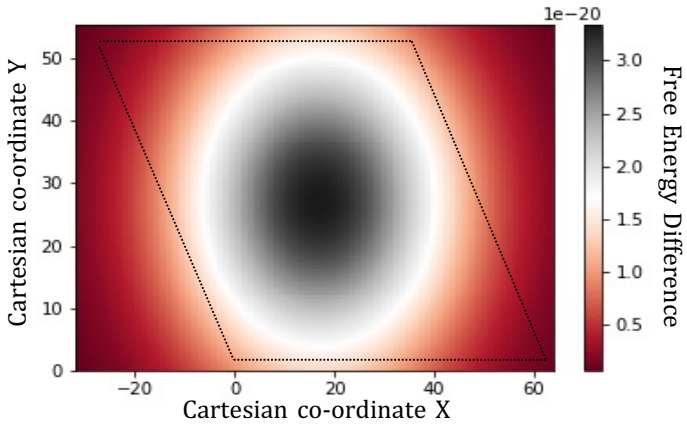

Figure 7.7: Reconstructed FEL with metadynamics using the skyrmion core centre as a CV in a hexagonal lattice. As can be seen, the reconstructed FEL has only shallow features, with no distinct potential basins or peaks where the skyrmion is pinned or deflected. However, as it can be seen, in the top left and bottom right corners, more MC steps are required for metadynamics to sample the whole lattice fully.

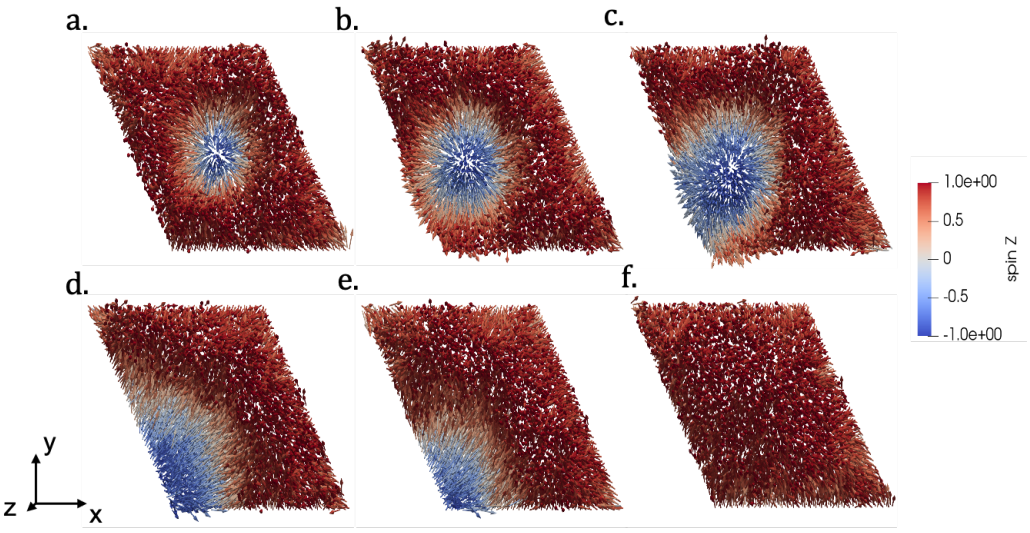

Figure 7.8: Confined lattice simulation progress snapshots a-e.

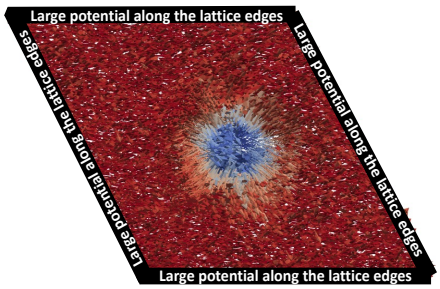

Figure 7.9: Illustration of the large repulsive potential which can be used to reconstruct the free energy landscape of a finite size lattice with defects without annihilating the skyrmion at the boundaries

7.2 Future Directions and Next Steps

In chapter 6, it was demonstrated that the skyrmion lifetime and the attempt frequency can be calculated using metadynamics. The next step of this research project is to apply the method introduced in chapter 6 in specific material heterostructures. Similarly, in the previous sections of this chapter, it was extensively discussed how metadynamics can be used to study the effect of lattice defects which is important for the design and realisation of future skyrmionic devices, which is also a continuation of this project.

In this thesis, the primary investigation with metadynamics was conducted on magnetic skyrmions. However, using different CVs, metadynamics can be used to explore the thermal stability of other spin textures. Recently a lot of research is focused on exploring the stability and dynamics of skyrmioniums [109], which are skyrmions with higher helicity that are shown to be valuable for the future neuromorphic skyrmionic devices [110]. The stability of skyrmioniums can be studied by reconstructing the FEL similar to the ones shown in section 4 with adding an extra CV to describe their helicity. This also offers the possibility of identifying more metastable spin textures a specific thin film or heterostructure can have, offering more states a device can take advantage of to design future computational devices. Similarly, fractional skyrmion tubes [111] where skyrmions are coupled along the z direction, which metadynamics can offer valuable insight. More specifically, recently, many computational techniques

have tried to study the binding energy of these fractional skyrmion tubes [112]. However, as the GNEBM, these are, in principle, athermal methods and include only the internal energy contributions of the associated energy barriers. In contrast with metadynamics, the fractional skyrmion tube energy can be estimated in finite temperatures, which also will include both the effects of entropy and internal energy in the estimations. Metadynamics can also be used to create 3D skyrmion or any topological spin texture stability phase diagrams with the DMI and Anisotropy as the x and y axis, which then every point in the diagram will be extracted from the FEL similar to chapter 4. This can then be also studied as a function of temperatures to investigate the skyrmion stability further. To conclude, metadynamics in condensed matter magnetism is not restricted only to skyrmions. It can be used to explore the stability of a plethora of topological spin textures, as shown in this thesis.

One of the drawbacks of metadynamics is the computationally expensive calculations of the CVs, which limit the use of metadynamics to larger lattices or more complex systems. In this project, the Metropolis MC algorithm was used with serial calculations, which in principle, is slow.However, one possible direction this research can take will be to parallelise the simulations' calculations to reduce computational time significantly. This can be achieved by parallelising the metropolis MC simulations or using the LLG, which can be parallelised using GPUs instead of CPUs as achieved in Mumax3 [76]. The MC simulations can be parallelised using the random walker algorithm, which can use parallel simulations to explore different sections of the configurational space. By doing so, the potential will be build simultaneously across the whole configurational space. However, this creates a technical difficulty; the file used to store the potential during the simulation will need to be accessed and updated from the simultaneous simulations, which can result in corrupt files (when trying to access a file before it is closed). Similarly, the LLG equation includes the Gilbert damping parameter and the bias factor, which are material-specific and dictate the magnetisation dynamics. During a metadynamics simulation using the LLG, the bias potential build can bias these parameters; to push the system away from its equilibrium state and explore the landscape defined by the CVs. If this occurs, then the simulation will be invalid since the dynamics of the simulation will not be the ones of the system studied, resulting in a different FEL structure. Hence, it must be ensured

that metadynamics will not change those parameters in LLG. Once the metadynamics simulations are parallelised, then quantum thermostats, as recently used [73] to make the atomistic semiquantum, can be used. By doing so, the temperature artefacts introduced from the classical thermostat will be reduced, which will allow the use of metadynamics in temperatures closer to the T_{C}.

CHAPTER 8

Conclusions

This thesis has successfully demonstrated that metadynamics can be used to reconstruct the FEL of topological spin textures such as skyrmions in condensed matter physics to study the skyrmions thermal stability and further used for a plethora of stability studies in finite temperatures as it is shown or proposed. This is crucial since most studies [2, 3, 54] have been using the GNEBM to quantify skyrmions energy barriers, including only the internal skyrmion energy, ΔE since GNEBM is a low or zero temperature formalism. Instead, we used metadynamics to reconstruct the FEL with metadynamics combined with atomistic simulations, in finite temperatures. Hence the energy barriers extracted from the FEL include both the ΔE and the change in configurational entropy ΔS, which, as has been demonstrated, is an important parameter of the skyrmions stabilisation [4]. Thus the skyrmion lifetimes can be estimated as

$$f = \tau_0 \cdot \exp\left(\frac{\Delta F}{k_{\mathrm{B}}T}\right) = \tau_0 \cdot \exp\left(\frac{-\Delta E}{k_{\mathrm{B}}T}\right) \cdot \exp\left(\frac{-\Delta S}{k_{\mathrm{B}}}\right) \tag{8.1}$$

where ΔF is energy barrier including the contributions from both ΔE and ΔS. The attempt frequency, τ_0, is assumed to be in the GHz range. However, it has been demonstrated that τ_0 changes more than 30 orders [82]. Thus in section 7, a novel method to extract the τ_0 in finite temperatures is proposed where metadynamics using the procedure introduced in section 6. Additionally, in section 7.1.2 it is shown and discussed how skyrmions can be moved within the lattice in order to sample a lattice with defects and how the skyrmion motion is affected by the Gaussian amplitude and deposition stride. Next, in section 5 by using metadynamics the magnetisation in a lattice with and without DMI was studied. This study revealed that during the magnetisation reversal in the lattice with DMI, the magnetisation rotation is not coherent; it creates a second metastable chiral domain which then expands. As described this gave an insight into the magnetisation reversal in single-domain thin films which is often said that the magnetisation reversal occurs with a coherent rotation; while this is true in simple ferromagnetic thin films. Interestingly this was also validated in section 4. For all these studies, the CVs calculations are discussed and the appropriate boundary conditions used or developed in this thesis are discussed.

In conclusion, this thesis has successfully demonstrated that the skyrmion metastable energy can be sampled with metadynamics and the studies in this thesis highlight the importance of using metadynamics to study the stability of spin textures. The primary aim of this thesis

achieved was to demonstrate a finite temperature method that the skyrmion stabilities can be studied, to help the realisation of the next skyrmionic devices. However, the results here can be applied to other spin textures, and metadynamics can be further used in condensed matter magnetism to identify spin textures in heterostructures and further thermal stability studies. However, the ultimate goal achieved was to demonstrate a procedure that can be used to design and realise the next skyrmionic or any spin texture spintronic devices to overcome Moore's postulation and continue increasing the computational power of computations or specific applications requiring neuromorphic beyond Von-Neumann architectures.

BIBLIOGRAPHY

[1] Albert Fert, Nicolas Reyren, and Vincent Cros. Magnetic skyrmions: advances in physics and potential applications. *Nat. Rev. Mater.*, 2:17031, 6 2017. doi: 10.1038/natrevmats.2017.31. URL https://dx.doi.org/10.1038/natrevmats.2017.31.

[2] David Cortés-Ortuño, Weiwei Wang, Marijan Beg, Ryan A. Pepper, Marc-Antonio Bisotti, Rebecca Carey, Mark Vousden, Thomas Kluyver, Ondrej Hovorka, and Hans Fangohr. Thermal stability and topological protection of skyrmions in nanotracks. *Sci. Rep.*, 7:4060, 6 2017. doi: 10.1038/s41598-017-03391-8. URL https://dx.doi.org/10.1038/s41598-017-03391-8.

[3] L. Desplat, J.-V. Kim, and R. L. Stamps. Paths to annihilation of first- and second-order (anti)skyrmions via (anti)meron nucleation on the frustrated square lattice. *Phys. Rev. B*, 99:174409, May 2019. doi: 10.1103/PhysRevB.99.174409. URL https://link.aps.org/doi/10.1103/PhysRevB.99.174409.

[4] L. Desplat, D. Suess, J-V. Kim, and R. L. Stamps. Thermal stability of metastable magnetic skyrmions: Entropic narrowing and significance of internal eigenmodes. *Phys. Rev. B*, 98:134407, Oct 2018. doi: 10.1103/PhysRevB.98.134407. URL https://link.aps.org/doi/10.1103/PhysRevB.98.134407.

[5] Iñigo Marcos-Alcalde, Eduardo López-Viñas, and Paulino Gómez-Puertas. MEPSAnd: minimum energy path surface analysis over n-dimensional surfaces. *Bioinformatics*, 36: 956–958, 8 2019. doi: 10.1093/bioinformatics/btz649. URL https://dx.doi.org/10.1093/bioinformatics/btz649.

[6] Linge Bai and David Breen. Calculating Center of Mass in an Unbounded 2D Environment. *J. Graph. Tools*, 13:53–60, 1 2008. doi: 10.1080/2151237x.2008.10129266. URL https://dx.doi.org/10.1080/2151237x.2008.10129266.

[7] Eric Masanet, Arman Shehabi, Nuoa Lei, Sarah Smith, and Jonathan Koomey. Recalibrating global data center energy-use estimates. *Science*, 367:984–986, 2 2020. doi: 10.1126/science.aba3758. URL https://dx.doi.org/10.1126/science.aba3758.

[8] Intel xeon gold 6138 processor (27.5m cache, 2.00 ghz) product specifications. URL https://www.intel.co.uk/content/www/uk/en/products/sku/120476/intel-xeon-gold-6138-processor-27-5m-cache-2-00-ghz/specifications.html. Accessed 01/3/2023.

[9] Energy Department for Business and Industrial Strategy. Greenhouse gas reporting: conversion factors 2018, 06 2022. URL https://www.gov.uk/government/publications/greenhouse-gas-reporting-conversion-factors-2022.

[10] Anders Clausen, Girish Ghatikar, and Bo NØrregaard JØrgensen. Load management of data centers as regulation capacity in denmark. In *International Green Computing Conference*, pages 1–10, 2014. doi: 10.1109/IGCC.2014.7039161.

[11] Moore law and intel innovation. URL https://www.intel.co.uk/content/www/uk/en/history/museum-gordon-moore-law.html.

[12] Scott E. Thompson and Srivatsan Parthasarathy. Moore's law: the future of si microelectronics. *Materials Today*, 9(6):20–25, 2006. ISSN 1369-7021. doi: https://doi.org/10.1016/S1369-7021(06)71539-5. URL https://www.sciencedirect.com/science/article/pii/S1369702106715395.

[13] Uygar E. Avci, Daniel H. Morris, and Ian A. Young. Tunnel Field-Effect Transistors: Prospects and Challenges. *IEEE J. Electron Devices Soc.*, 3:88–95, 5 2015. doi: 10.1109/jeds.2015.2390591. URL https://dx.doi.org/10.1109/jeds.2015.2390591.

[14] S.E. Thompson, R.S. Chau, T. Ghani, K. Mistry, S. Tyagi, and M.T. Bohr. In search of "forever," continued transistor scaling one new material at a time. *IEEE Transactions on Semiconductor Manufacturing*, 18(1):26–36, 2005. doi: 10.1109/TSM.2004.841816.

[15] Sujay B. Desai, Surabhi R. Madhvapathy, Angada B. Sachid, Juan Pablo Llinas, Qingxiao Wang, Geun Ho Ahn, Gregory Pitner, Moon J. Kim, Jeffrey Bokor, Chenming Hu, H.-S. Philip Wong, and Ali Javey. MoS $_2$ transistors with 1-nanometer gate lengths. *Science*, 354:99–102, 10 2016. doi: 10.1126/science.aah4698. URL https://dx.doi.org/10.1126/science.aah4698.

[16] Niranjan A. Natekar and R. H. Victora. Analytical Estimation of Transition Jitter for the Heat-Assisted Magnetic Recording Process. *IEEE Magn. Lett.*, 11:1–4, 2020. doi: 10.1109/lmag.2020.2992221. URL https://dx.doi.org/10.1109/lmag.2020.2992221.

[17] Catherine D. Schuman, Shruti R. Kulkarni, Maryam Parsa, J. Parker Mitchell, Prasanna Date, and Bill Kay. Opportunities for neuromorphic computing algorithms and applications. *Nat. Comput. Sci.*, 2:10–19, 1 2022. doi: 10.1038/s43588-021-00184-y. URL https://dx.doi.org/10.1038/s43588-021-00184-y.

[18] Kazunori Akiyama, Andrew Chael, and Dominic W. Pesce. New views of black holes from computational imaging. *Nat. Comput. Sci.*, 1:300–303, 5 2021. doi: 10.1038/s43588-021-00078-z. URL https://dx.doi.org/10.1038/s43588-021-00078-z.

[19] John Ryding David Reinsel, John Gantz. The digizatiom of the world from edge to core. 2018.

[20] Niranjan A. Natekar and R. H. Victora. Analytical Estimation of Transition Jitter for the Heat-Assisted Magnetic Recording Process. *IEEE Magn. Lett.*, 11:1–4, 2020. doi: 10.1109/lmag.2020.2992221. URL https://dx.doi.org/10.1109/lmag.2020.2992221.

[21] Atsufumi Hirohata, Keisuke Yamada, Yoshinobu Nakatani, Ioan-Lucian Prejbeanu, Bernard Diény, Philipp Pirro, and Burkard Hillebrands. Review on spintronics: Principles and device applications. *J. Magn. Magn. Mater.*, 509:166711, 9 2020. doi: 10.1016/j.jmmm.2020.166711. URL https://dx.doi.org/10.1016/j.jmmm.2020.166711.

[22] Kang Wang, Vineetha Bheemarasetty, Junhang Duan, Shiyu Zhou, and Gang Xiao. Fundamental physics and applications of skyrmions: A review. *J. Magn. Magn. Mater.*, 563: 169905, 12 2022. doi: 10.1016/j.jmmm.2022.169905. URL https://dx.doi.org/10.1016/j.jmmm.2022.169905.

[23] YaJun Zhang, Qi Zheng, XiaoRui Zhu, Zhe Yuan, and Ke Xia. Spintronic devices for neuromorphic computing. *Sci. China Phys., Mech. amp; Astron.*, 63: 277531, 2 2020. doi: 10.1007/s11433-019-1499-3. URL https://dx.doi.org/10.1007/s11433-019-1499-3.

[24] D. A. Allwood, G. Xiong, C. C. Faulkner, D. Atkinson, D. Petit, and R. P. Cowburn. Magnetic Domain-Wall Logic. *Science*, 309:1688–1692, 9 2005. doi: 10.1126/science.1108813. URL https://dx.doi.org/10.1126/science.1108813.

[25] X. R. Wang, P. Yan, and J. Lu. High-field domain wall propagation velocity in magnetic nanowires. *EPL (Europhysics Lett.)*, 86:67001, 6 2009. doi: 10.1209/0295-5075/86/67001. URL https://dx.doi.org/10.1209/0295-5075/86/67001.

[26] Stuart SP Parkin, Masamitsu Hayashi, and Luc Thomas. Magnetic domain-wall racetrack memory. *Science*, 320(5873):190–194, 2008.

[27] T. J. Hayward. Intrinsic Nature of Stochastic Domain Wall Pinning Phenomena in Magnetic Nanowire Devices. *Sci. Rep.*, 5:13279, 8 2015. doi: 10.1038/srep13279. URL https://dx.doi.org/10.1038/srep13279.

[28] A Mougin, M Cormier, J. P Adam, P. J Metaxas, and J Ferré. Domain wall mobility, stability and Walker breakdown in magnetic nanowires. *Eur. Lett. (EPL)*, 78:57007, 5 2007. doi: 10.1209/0295-5075/78/57007. URL https://dx.doi.org/10.1209/0295-5075/78/57007.

[29] Dan A. Allwood, Matthew O. A. Ellis, David Griffin, Thomas J. Hayward, Luca Manneschi, Mohammad F. KH. Musameh, Simon O'Keefe, Susan Stepney, Charles Swindells, Martin A. Trefzer, Eleni Vasilaki, Guru Venkat, Ian Vidamour, and Chester

Wringe. A perspective on physical reservoir computing with nanomagnetic devices. *Appl. Phys. Lett.*, 122:040501, 1 2023. doi: 10.1063/5.0119040. URL https://dx.doi.org/10.1063/5.0119040.

[30] S. Mühlbauer, B. Binz, F. Jonietz, C. Pfleiderer, A. Rosch, A. Neubauer, R. Georgii, and P. Böni. Skyrmion Lattice in a Chiral Magnet. *Science*, 323:915–919, 2 2009. doi: 10.1126/science.1166767. URL https://dx.doi.org/10.1126/science.1166767.

[31] Wang Kang, Yangqi Huang, Xichao Zhang, Yan Zhou, and Weisheng Zhao. Skyrmion-electronics: An overview and outlook. *Proceedings of the IEEE*, 104(10):2040–2061, 2016. doi: 10.1109/JPROC.2016.2591578.

[32] Luping Du, Aiping Yang, Anatoly V. Zayats, and Xiaocong Yuan. Deep-subwavelength features of photonic skyrmions in a confined electromagnetic field with orbital angular momentum. *Nat. Phys.*, 15:650–654, 4 2019. doi: 10.1038/s41567-019-0487-7. URL https://dx.doi.org/10.1038/s41567-019-0487-7.

[33] C. Moreau-Luchaire, C. Moutafis, N. Reyren, J. Sampaio, C. A. F. Vaz, N. Van Horne, K. Bouzehouane, K. Garcia, C. Deranlot, P. Warnicke, P. Wohlhüter, J.-M. George, M. Weigand, J. Raabe, V. Cros, and A. Fert. Additive interfacial chiral interaction in multilayers for stabilization of small individual skyrmions at room temperature. *Nat. Nanotechnol.*, 11:444–448, 1 2016. doi: 10.1038/nnano.2015.313. URL https://dx.doi.org/10.1038/nnano.2015.313.

[34] Olivier Boulle, Jan Vogel, Hongxin Yang, Stefania Pizzini, Dayane de Souza Chaves, Andrea Locatelli, Tevfik Onur Menteş, Alessandro Sala, Liliana D. Buda-Prejbeanu, Olivier Klein, Mohamed Belmeguenai, Yves Roussigné, Andrey Stashkevich, Salim Mourad Chérif, Lucia Aballe, Michael Foerster, Mairbek Chshiev, Stéphane Auffret, Ioan Mihai Miron, and Gilles Gaudin. Room-temperature chiral magnetic skyrmions in ultrathin magnetic nanostructures. *Nat. Nanotechnol.*, 11:449–454, 1 2016. doi: 10.1038/nnano.2015.315. URL https://dx.doi.org/10.1038/nnano.2015.315.

[35] Tomoyuki Yokouchi, Satoshi Sugimoto, Bivas Rana, Shinichiro Seki, Naoki Ogawa,

Yuki Shiomi, Shinya Kasai, and Yoshichika Otani. Pattern recognition with neuromorphic computing using magnetic field–induced dynamics of skyrmions. *Science Advances*, 8(39), 2022. doi: 10.1126/sciadv.abq5652. URL https://www.science.org/doi/abs/10.1126/sciadv.abq5652.

[36] T.H.R. Skyrme. A unified field theory of mesons and baryons. *Nuclear Physics*, 31: 556–569, 1962. ISSN 0029-5582. doi: https://doi.org/10.1016/0029-5582(62)90775-7. URL https://www.sciencedirect.com/science/article/pii/0029558262907757.

[37] A. N. Bogdanov and D. A. Yablonskii. Thermodynamically stable "vortices" in magnetically ordered crystals. The mixed state of magnets. *Soviet Journal of Experimental and Theoretical Physics*, 68(1):101, January 1989.

[38] A. Bogdanov and A. Hubert. Thermodynamically stable magnetic vortex states in magnetic crystals. *Journal of Magnetism and Magnetic Materials*, 138(3):255–269, 1994. ISSN 0304-8853. doi: https://doi.org/10.1016/0304-8853(94)90046-9. URL https://www.sciencedirect.com/science/article/pii/0304885394900469.

[39] A. Neubauer, C. Pfleiderer, B. Binz, A. Rosch, R. Ritz, P. G. Niklowitz, and P. Böni. Topological Hall Effect in theAPhase of MnSi. *Phys. Rev. Lett.*, 102:186602, 5 2009. doi: 10.1103/physrevlett.102.186602. URL https://dx.doi.org/10.1103/physrevlett.102.186602.

[40] W. Münzer, A. Neubauer, T. Adams, S. Mühlbauer, C. Franz, F. Jonietz, R. Georgii, P. Böni, B. Pedersen, M. Schmidt, A. Rosch, and C. Pfleiderer. Skyrmion lattice in the doped semiconductorFe_1âˆ'xCoxSi. *Phys. Rev. B*, 81:041203, 1 2010. doi: 10.1103/physrevb.81.041203. URL https://dx.doi.org/10.1103/physrevb.81.041203.

[41] A. B. Butenko, A. A. Leonov, U. K. Rößler, and A. N. Bogdanov. Stabilization of skyrmion textures by uniaxial distortions in noncentrosymmetric cubic helimagnets. *Phys. Rev. B*, 82:052403, 8 2010. doi: 10.1103/physrevb.82.052403. URL https://dx.doi.org/10.1103/physrevb.82.052403.

[42] S. X. Huang and C. L. Chien. Extended Skyrmion Phase in EpitaxialFeGe(111)Thin Films. *Phys. Rev. Lett.*, 108:267201, 6 2012. doi: 10.1103/physrevlett.108.267201. URL https://dx.doi.org/10.1103/physrevlett.108.267201.

[43] Albert Fert, Vincent Cros, and João Sampaio. Skyrmions on the track. *Nat. Nanotechnol.*, 8:152–156, 3 2013. doi: 10.1038/nnano.2013.29. URL https://dx.doi.org/10.1038/nnano.2013.29.

[44] Seonghoon Woo, Kai Litzius, Benjamin Krüger, Mi-Young Im, Lucas Caretta, Kornel Richter, Maxwell Mann, Andrea Krone, Robert M. Reeve, Markus Weigand, Parnika Agrawal, Ivan Lemesh, Mohamad-Assaad Mawass, Peter Fischer, Mathias Kläui, and Geoffrey S. D. Beach. Observation of room-temperature magnetic skyrmions and their current-driven dynamics in ultrathin metallic ferromagnets. *Nat. Mater.*, 15:501–506, 2 2016. doi: 10.1038/nmat4593. URL https://dx.doi.org/10.1038/nmat4593.

[45] Yoshinori Tokura and Naoya Kanazawa. Magnetic Skyrmion Materials. *Chem. Rev.*, 121:2857–2897, 11 2020. doi: 10.1021/acs.chemrev.0c00297. URL https://dx.doi.org/10.1021/acs.chemrev.0c00297.

[46] R. Tomasello, E. Martinez, R. Zivieri, L. Torres, M. Carpentieri, and G. Finocchio. A strategy for the design of skyrmion racetrack memories. *Sci. Rep.*, 4:6784, 10 2014. doi: 10.1038/srep06784. URL https://dx.doi.org/10.1038/srep06784.

[47] Yan Zhou and Motohiko Ezawa. A reversible conversion between a skyrmion and a domain-wall pair in a junction geometry. *Nat. Commun.*, 5:4652, 8 2014. doi: 10.1038/ncomms5652. URL https://dx.doi.org/10.1038/ncomms5652.

[48] Xichao Zhang, Motohiko Ezawa, and Yan Zhou. Magnetic skyrmion logic gates: conversion, duplication and merging of skyrmions. *Sci. Rep.*, 5:9400, 3 2015. doi: 10.1038/srep09400. URL https://dx.doi.org/10.1038/srep09400.

[49] Shijiang Luo and Long You. Skyrmion devices for memory and logic applications. *APL Mater.*, 9:050901, 5 2021. doi: 10.1063/5.0042917. URL https://dx.doi.org/10.1063/5.0042917.

[50] Tomoyuki Yokouchi, Satoshi Sugimoto, Bivas Rana, Shinichiro Seki, Naoki Ogawa, Yuki Shiomi, Shinya Kasai, and Yoshichika Otani. Pattern recognition with neuromorphic computing using magnetic field–induced dynamics of skyrmions. *Science Advances*, 8(39):eabq5652, 2022. doi: 10.1126/sciadv.abq5652. URL https://www.science.org/doi/abs/10.1126/sciadv.abq5652.

[51] Kitae Kim, Seong-Hyub Lee, Yooleemi Shin, Ji-Wan Kim, Jung-Hyun Park, Jun-Young Chang, and Sug-Bong Choe. Experimental verification of the Thiele equation for skyrmion Hall angle. *Appl. Phys. Express*, 16:033001, 3 2023. doi: 10.35848/1882-0786/acb7c8. URL https://dx.doi.org/10.35848/1882-0786/acb7c8.

[52] Pavel F. Bessarab, Valery M. Uzdin, and Hannes Jónsson. Method for finding mechanism and activation energy of magnetic transitions, applied to skyrmion and antivortex annihilation. *Comput. Phys. Commun.*, 196:335–347, 11 2015. doi: 10.1016/j.cpc.2015.07.001. URL https://dx.doi.org/10.1016/j.cpc.2015.07.001.

[53] Md Golam Morshed, Hamed Vakili, and Avik W. Ghosh. Positional stability of skyrmions in a racetrack memory with notched geometry. *Phys. Rev. Appl.*, 17:064019, Jun 2022. doi: 10.1103/PhysRevApplied.17.064019. URL https://link.aps.org/doi/10.1103/PhysRevApplied.17.064019.

[54] V.M. Uzdin, M.N. Potkina, I.S. Lobanov, P.F. Bessarab, and H. Jónsson. Energy surface and lifetime of magnetic skyrmions. *J. Magn. Magn. Mater.*, 459:236–240, 8 2018. doi: 10.1016/j.jmmm.2017.10.100. URL https://dx.doi.org/10.1016/j.jmmm.2017.10.100.

[55] C. Reichhardt, C. J. O. Reichhardt, and M. V. Milošević. Statics and dynamics of skyrmions interacting with disorder and nanostructures. *Rev. Mod. Phys.*, 94:035005, 9 2022. doi: 10.1103/revmodphys.94.035005. URL https://dx.doi.org/10.1103/revmodphys.94.035005.

[56] John B. Kramer. The Early History of Magnetism. *Trans. Newcom. Soc.*, 14:183–200, 1 1933. doi: 10.1179/tns.1933.013. URL https://dx.doi.org/10.1179/tns.1933.013.

[57] Daniel C. Mattis. *History of Magnetism*, pages 1–38. Springer Berlin Heidelberg, Berlin, Heidelberg, 1981. ISBN 978-3-642-83238-3. doi: 10.1007/978-3-642-83238-3_1. URL https://doi.org/10.1007/978-3-642-83238-3_1.

[58] *The Early History*, pages 3–15. Springer New York, New York, NY, 2006. ISBN 978-0-387-47290-4. doi: 10.1007/978-0-387-47290-4_1. URL https://doi.org/10.1007/978-0-387-47290-4_1.

[59] A.S. Mahajan and A.A. Rangwala. *Electricity and Magnetism*. 2001. ISBN 9780074602256.

[60] Stephen Blundell. *Magnetism in condensed matter*. Oxford University Press, 2003.

[61] N.W. Ashcroft and N.D. Mermin. *Solid State Physics*. Cengage Learning, 2011. ISBN 9788131500521.

[62] P.W. Anderson. *Concepts in Solids: Lectures on the Theory of Solids*. Advanced book classics series. World Scientific, 1997. ISBN 9789810232313. URL https://books.google.co.uk/books?id=2NEKzzbMbRgC.

[63] *Magnetic Materials*.

[64] Karin Larsson. *Chemical Vapour Deposition*. 2053-2563. IOP Publishing, 2022. ISBN 978-0-7503-3107-4. doi: 10.1088/978-0-7503-3107-4. URL https://dx.doi.org/10.1088/978-0-7503-3107-4.

[65] Richard W. Dawidek, Thomas J. Hayward, Ian T. Vidamour, Thomas J. Broomhall, Guru Venkat, Mohanad Al Mamoori, Aidan Mullen, Stephan J. Kyle, Paul W. Fry, Nina-Juliane Steinke, Joshaniel F. K. Cooper, Francesco Maccherozzi, Sarnjeet S. Dhesi, Lucia Aballe, Michael Foerster, Jordi Prat, Eleni Vasilaki, Matthew O. A. Ellis, and Dan A. Allwood. Dynamically Driven Emergence in a Nanomagnetic System. *Adv. Funct. Mater.*, 31:2008389, 2 2021. doi: 10.1002/adfm.202008389. URL https://dx.doi.org/10.1002/adfm.202008389.

[66] Sebastian Meyer, Marco Perini, Stephan von Malottki, André Kubetzka, Roland Wiesendanger, Kirsten von Bergmann, and Stefan Heinze. Isolated zero field sub-10 nm skyrmions in ultrathin Co films. *Nat. Commun.*, 10:3823, 8 2019. doi: 10.1038/s41467-019-11831-4. URL https://dx.doi.org/10.1038/s41467-019-11831-4.

[67] Imara Lima Fernandes, Juba Bouaziz, Stefan Blügel, and Samir Lounis. Universality of defect-skyrmion interaction profiles. *Nat. Commun.*, 9:4395, 10 2018. doi: 10.1038/s41467-018-06827-5. URL https://dx.doi.org/10.1038/s41467-018-06827-5.

[68] Dmitry A. Garanin, Reem Jaafar, and Eugene M. Chudnovsky. Breathing mode of a skyrmion on a lattice. *Phys. Rev. B*, 101:014418, 1 2020. doi: 10.1103/physrevb.101.014418. URL https://dx.doi.org/10.1103/physrevb.101.014418.

[69] Mohammed Bouhassoune and Samir Lounis. Friedel Oscillations Induced by Magnetic Skyrmions: From Scattering Properties to All-Electrical Detection. *Nanomaterials*, 11:194, 1 2021. doi: 10.3390/nano11010194. URL https://dx.doi.org/10.3390/nano11010194.

[70] S.C. Westmoreland, R.F.L. Evans, G. Hrkac, T. Schrefl, G.T. Zimanyi, M. Winklhofer, N. Sakuma, M. Yano, A. Kato, T. Shoji, A. Manabe, M. Ito, and R.W. Chantrell. Multiscale model approaches to the design of advanced permanent magnets. *Scripta Materialia*, 148:56–62, 4 2018. doi: 10.1016/j.scriptamat.2018.01.019. URL https://dx.doi.org/10.1016/j.scriptamat.2018.01.019.

[71] U. Atxitia, D. Hinzke, O. Chubykalo-Fesenko, U. Nowak, H. Kachkachi, O. N. Mryasov, R. F. Evans, and R. W. Chantrell. Multiscale modeling of magnetic materials: Temperature dependence of the exchange stiffness. *Phys. Rev. B*, 82:134440, Oct 2010. doi: 10.1103/PhysRevB.82.134440. URL https://link.aps.org/doi/10.1103/PhysRevB.82.134440.

[72] *Handbook of materials modeling : methods: theory and modeling*. Springer, Cham, second edition. edition, 2020. ISBN 9783319446776.

[73] Joseph Barker and Gerrit E. W. Bauer. Semiquantum thermodynamics of complex ferrimagnets. *Phys. Rev. B*, 100:140401, Oct 2019. doi: 10.1103/PhysRevB.100.140401. URL https://link.aps.org/doi/10.1103/PhysRevB.100.140401.

[74] Josef Fidler and Thomas Schrefl. Micromagnetic modelling - the current state of the art. *J. Phys. D: Appl. Phys.*, 33:R135–R156, 7 2000. doi: 10.1088/0022-3727/33/15/201. URL https://dx.doi.org/10.1088/0022-3727/33/15/201.

[75] Claas Abert. Micromagnetics and spintronics: models and numerical methods. *Eur. Phys. J. B*, 92:120, 6 2019. doi: 10.1140/epjb/e2019-90599-6. URL https://dx.doi.org/10.1140/epjb/e2019-90599-6.

[76] Arne Vansteenkiste, Jonathan Leliaert, Mykola Dvornik, Mathias Helsen, Felipe Garcia-Sanchez, and Bartel Van Waeyenberge. The design and verification of MuMax3. *AIP Adv.*, 4:107133, 10 2014. doi: 10.1063/1.4899186. URL https://dx.doi.org/10.1063/1.4899186.

[77] Michael Donahue. Oommf user's guide, version 1.0, 1999-09-01 1999.

[78] Marc-Antonio Bisotti, David Cortés-Ortuño, Ryan Pepper, Weiwei Wang, Marijan Beg, Thomas Kluyver, and Hans Fangohr. Fidimag – A Finite Difference Atomistic and Micromagnetic Simulation Package. *J. Open Res. Softw.*, 6:22, 9 2018. doi: 10.5334/jors.223. URL https://dx.doi.org/10.5334/jors.223.

[79] Pablo Chubykalo-Fesenko, Oksanaand Nieves. *Landau-Lifshitz-Bloch Approach for Magnetization Dynamics Close to Phase Transition*, pages 867–893. Springer International Publishing, Cham, 2020. ISBN 978-3-319-44677-6. doi: 10.1007/978-3-319-44677-6_72. URL https://doi.org/10.1007/978-3-319-44677-6_72.

[80] D.V. Berkov and J. Miltat. Spin-torque driven magnetization dynamics: Micromagnetic modeling. *J. Magn. Magn. Mater.*, 320:1238–1259, 4 2008. doi: 10.1016/j.jmmm.2007.12.023. URL https://dx.doi.org/10.1016/j.jmmm.2007.12.023.

[81] J. Hagemeister, N. Romming, K. von Bergmann, E. Y. Vedmedenko, and R. Wiesendanger. Stability of single skyrmionic bits. *Nat. Commun.*, 6:8455, 10 2015. doi: 10.1038/ncomms9455. URL https://dx.doi.org/10.1038/ncomms9455.

[82] Johannes Wild, Thomas N. G. Meier, Simon PÃ¶llath, Matthias Kronseder, Andreas Bauer, Alfonso Chacon, Marco Halder, Marco Schowalter, Andreas Rosenauer, Josef Zweck, Jan MÃ¼ller, Achim Rosch, Christian Pfleiderer, and Christian H. Back. Entropy-limited topological protection of skyrmions. *Science Advances*, 3(9):e1701704, 2017. doi: 10.1126/sciadv.1701704. URL https://www.science.org/doi/abs/10.1126/sciadv.1701704.

[83] Steven Fitzgerald, Amanda Bailey Hass, Grisell Diaz Leines, and Andrew John Archer. Stochastic transitions: Paths over higher energy barriers can dominate in the early stages. *The Journal of Chemical Physics*, 0(ja):null, 0. doi: 10.1063/5.0135880. URL https://doi.org/10.1063/5.0135880.

[84] Alessandro Laio and Michele Parrinello. Escaping free-energy minima. *Proc. Natl. Acad. Sci.*, 99:12562–12566, 9 2002. doi: 10.1073/pnas.202427399. URL https://dx.doi.org/10.1073/pnas.202427399.

[85] Giovanni Bussi and Davide Branduardi. *Free-Energy Calculations with Metadynamics: Theory and Practice*, chapter 1, pages 1–49. John Wiley and Sons, Ltd, 2015. ISBN 9781118889886. doi: https://doi.org/10.1002/9781118889886.ch1. URL https://onlinelibrary.wiley.com/doi/abs/10.1002/9781118889886.ch1.

[86] F. Marini, C. Camilloni, D. Provasi, R.A. Broglia, and G. Tiana. Metadynamic sampling of the free-energy landscapes of proteins coupled with a Monte Carlo algorithm. *Gene*, 422:37–40, 10 2008. doi: 10.1016/j.gene.2008.06.003. URL https://dx.doi.org/10.1016/j.gene.2008.06.003.

[87] Balázs Nagyfalusi, László Udvardi, and László Szunyogh. Metadynamics study of the temperature dependence of magnetic anisotropy and spin-reorientation transitions in ul-

trathin films. *Phys. Rev. B*, 100:174429, Nov 2019. doi: 10.1103/PhysRevB.100.174429. URL https://link.aps.org/doi/10.1103/PhysRevB.100.174429.

[88] Jaroslav Tóbik, Roman Martoňák, and Vladimír Cambel. Free-energy landscapes in magnetic systems from metadynamics. *Phys. Rev. B*, 96:140413, Oct 2017. doi: 10.1103/PhysRevB.96.140413. URL https://link.aps.org/doi/10.1103/PhysRevB.96.140413.

[89] D.P. Landau and K. Binder. *A Guide to Monte Carlo Simulations in Statistical Physics*. Cambridge University Press, 2014. ISBN 9781107074026.

[90] K. Binder, K. Binder, D.M. Ceperley, J.P. Hansen, M.H. Kalos, D.P. Landau, D. Levesque, H. Müller-Krumbhaar, D. Stauffer, and J.J. Weis. *Monte Carlo Methods in Statistical Physics*. Topics in Current Physics. Springer Berlin Heidelberg, 2012. ISBN 9783642828034.

[91] K Binder. Applications of Monte Carlo methods to statistical physics. *Rep. Prog. Phys.*, 60:487–559, 5 1997. doi: 10.1088/0034-4885/60/5/001. URL https://dx.doi.org/10.1088/0034-4885/60/5/001.

[92] Surya T. Tokdar and Robert E. Kass. Importance sampling: a review. *WIREs Comput. Stat.*, 2:54–60, 12 2009. doi: 10.1002/wics.56. URL https://dx.doi.org/10.1002/wics.56.

[93] Surya T. Tokdar and Robert E. Kass. Importance sampling: a review. *WIREs Computational Statistics*, 2(1):54–60, 2010. doi: https://doi.org/10.1002/wics.56. URL https://wires.onlinelibrary.wiley.com/doi/abs/10.1002/wics.56.

[94] A. Stevens. *Monte-Carlo Simulation: An Introduction for Engineers and Scientists*. CRC Press, 2022. ISBN 9781032280776.

[95] Nicholas Metropolis, Arianna W. Rosenbluth, Marshall N. Rosenbluth, Augusta H. Teller, and Edward Teller. Equation of State Calculations by Fast Computing Machines. *J. Chem. Phys.*, 21:1087–1092, 6 1953. doi: 10.1063/1.1699114. URL https://dx.doi.org/10.1063/1.1699114.

[96] Alessandro Laio and Francesco L Gervasio. Metadynamics: a method to simulate rare events and reconstruct the free energy in biophysics, chemistry and material science. *Rep. Prog. Phys.*, 71:126601, 11 2008. doi: 10.1088/0034-4885/71/12/126601. URL https://dx.doi.org/10.1088/0034-4885/71/12/126601.

[97] G. Sanfilippo F. Laio, A. Martinelli. Metadynamics surfing on topology barriers: The CP^{N-1} case. *Journal of High Energy Physics*, 89:214412, Jun 2016. doi: 10.1007/JHEP07(2016)089. URL https://doi.org/10.1007/JHEP07(2016)089.

[98] A. Laio and M. Parrinello. *Computing Free Energies and Accelerating Rare Events with Metadynamics*, pages 315–347. Springer Berlin Heidelberg, Berlin, Heidelberg, 2006. doi: 10.1007/3-540-35273-2_9. URL https://doi.org/10.1007/3-540-35273-2_9.

[99] Giovanni Bussi and Alessandro Laio. Using metadynamics to explore complex free-energy landscapes. *Nat. Rev. Phys.*, 2:200–212, 3 2020. doi: 10.1038/s42254-020-0153-0. URL https://dx.doi.org/10.1038/s42254-020-0153-0.

[100] Alessandro Barducci, Giovanni Bussi, and Michele Parrinello. Well-Tempered Metadynamics: A Smoothly Converging and Tunable Free-Energy Method. *Phys. Rev. Lett.*, 100:020603, 1 2008. doi: 10.1103/physrevlett.100.020603. URL https://dx.doi.org/10.1103/physrevlett.100.020603.

[101] Yanier Crespo, Fabrizio Marinelli, Fabio Pietrucci, and Alessandro Laio. Metadynamics convergence law in a multidimensional system. *Phys. Rev. E*, 81:055701, 2010. doi: 10.1103/PhysRevE.81.055701. URL https://link.aps.org/doi/10.1103/PhysRevE.81.055701.

[102] Earl Callen and Herbert B. Callen. Magnetostriction, forced magnetostriction, and anomalous thermal expansion in ferromagnets. *Phys. Rev.*, 139:A455–A471, Jul 1965. doi: 10.1103/PhysRev.139.A455. URL https://link.aps.org/doi/10.1103/PhysRev.139.A455.

[103] B. Berg and M. Lüscher. Definition and statistical distributions of a topological number in the lattice o(3) σ-model. *Nuclear Physics B*, 190(2):412–424, 1981. ISSN 0550-3213.

doi: https://doi.org/10.1016/0550-3213(81)90568-X. URL https://www.sciencedirect.com/science/article/pii/055032138190568X.

[104] Joo-Von Kim and Jeroen Mulkers. On quantifying the topological charge in micromagnetics using a lattice-based approach. *IOP SciNotes*, 1:025211, 8 2020. doi: 10.1088/2633-1357/abad0c. URL https://dx.doi.org/10.1088/2633-1357/abad0c.

[105] S. Rohart, J. Miltat, and A. Thiaville. Path to collapse for an isolated néel skyrmion. *Phys. Rev. B*, 93:214412, Jun 2016. doi: 10.1103/PhysRevB.93.214412. URL https://link.aps.org/doi/10.1103/PhysRevB.93.214412.

[106] Kathinka Gerlinger, Bastian Pfau, Felix BÃ¼ttner, Michael Schneider, Lisa-Marie Kern, Josefin Fuchs, Dieter Engel, Christian M. GÃ¼nther, Mantao Huang, Ivan Lemesh, Lucas Caretta, Alexandra Churikova, Piet Hessing, Christopher Klose, Christian StrÃ¼ber, Clemens von Korff Schmising, Siying Huang, Angela Wittmann, Kai Litzius, Daniel Metternich, Riccardo Battistelli, Kai Bagschik, Alexandr Sadovnikov, Geoffrey S. D. Beach, and Stefan Eisebitt. Application concepts for ultrafast laser-induced skyrmion creation and annihilation. *Applied Physics Letters*, 118(19), 05 2021. ISSN 0003-6951. doi: 10.1063/5.0046033. URL https://doi.org/10.1063/5.0046033. 192403.

[107] Katharina Zeissler, Simone Finizio, Kowsar Shahbazi, Jamie Massey, Fatma Al Ma'Mari, David M. Bracher, Armin Kleibert, Mark C. Rosamond, Edmund H. Linfield, Thomas A. Moore, Jörg Raabe, Gavin Burnell, and Christopher H. Marrows. Discrete Hall resistivity contribution from Néel skyrmions in multilayer nanodiscs. *Nat. Nanotechnol.*, 13:1161–1166, 10 2018. doi: 10.1038/s41565-018-0268-y. URL https://dx.doi.org/10.1038/s41565-018-0268-y.

[108] R F L Evans, W J Fan, P Chureemart, T A Ostler, M O A Ellis, and R W Chantrell. Atomistic spin model simulations of magnetic nanomaterials. *J. Phys.: Condens. Matter*, 26:103202, 2 2014. doi: 10.1088/0953-8984/26/10/103202. URL https://dx.doi.org/10.1088/0953-8984/26/10/103202.

[109] Alexander G. Kolesnikov, Maksim E. Stebliy, Alexander S. Samardak, and Alexey V.

Ognev. Skyrmionium – high velocity without the skyrmion Hall effect. *Sci. Rep.*, 8: 16966, 11 2018. doi: 10.1038/s41598-018-34934-2. URL https://dx.doi.org/10.1038/s41598-018-34934-2.

[110] Runze Chen, Yu Li, Vasilis F. Pavlidis, and Christoforos Moutafis. Skyrmionic interconnect device. *Phys. Rev. Res.*, 2:043312, 12 2020. doi: 10.1103/physrevresearch.2.043312. URL https://dx.doi.org/10.1103/physrevresearch.2.043312.

[111] Jagannath Jena, Börge Göbel, Tomoki Hirosawa, Sebastián A. Díaz, Daniel Wolf, Taichi Hinokihara, Vivek Kumar, Ingrid Mertig, Claudia Felser, Axel Lubk, Daniel Loss, and Stuart S. P. Parkin. Observation of fractional spin textures in a Heusler material. *Nat. Commun.*, 13:2348, 4 2022. doi: 10.1038/s41467-022-29991-1. URL https://dx.doi.org/10.1038/s41467-022-29991-1.

[112] Linjie Liu, Weijin Chen, and Yue Zheng. Skyrmion transport modified by surface terraces in magnetic multilayers. *Phys. Rev. Appl.*, 16:014050, Jul 2021. doi: 10.1103/PhysRevApplied.16.014050. URL https://link.aps.org/doi/10.1103/PhysRevApplied.16.014050.